12-2008

Investigation of Propagation Characteristics of Twisted Hollow Waveguides for Particle Accelerator Applications

Joshua Lee Wilson
University of Tennessee - Knoxville

To the Graduate Council:

I am submitting herewith a dissertation written by Joshua Lee Wilson entitled "Investigation of Propagation Characteristics of Twisted Hollow Waveguides for Particle Accelerator Applications." I have examined the final electronic copy of this dissertation for form and content and recommend that it be accepted in partial fulfillment of the requirements for the degree of Doctor of Philosophy, with a major in Electrical Engineering.

Aly E. Fathy, Major Professor

We have read this dissertation and recommend its acceptance:

Yoon Kang, Cheng Wang, Marshall Pace, Paul Crilly

Accepted for the Council:

Carolyn R. Hodges

Vice Provost and Dean of the Graduate School

(Original signatures are on file with official student records.)

To the Graduate Council:

I am submitting herewith a dissertation written by Joshua Lee Wilson entitled "Investigation of Propagation Characteristics of Twisted Hollow Waveguides for Particle Accelerator Applications". I have examined the final electronic copy of this dissertation for form and content and recommend that it be accepted in partial fulfillment of the requirements for the degree of Doctor of Philosophy, with a major in Electrical Engineering.

Aly E. Fathy, Major Professor

We have read this dissertation
and recommend its acceptance:

Yoon Kang

_____

Cheng Wang

_____

Marshall Pace

_____

Paul Crilly

_____

Accepted for the Council:

Carolyn R. Hodges, Vice Provost
and Dean of the Graduate School

(Original signatures are on file with official student records.)

Investigation of Propagation Characteristics of Twisted Hollow Waveguides for Particle Accelerator Applications

A Dissertation
Presented for the
Doctor of Electrical Engineering
Degree
The University of Tennessee, Knoxville

Joshua Lee Wilson
December 2008

Acknowledgments

This work has been sponsored by ORNL-SNS. The Spallation Neutron Source is managed by UT-Battelle, LLC, under contract DE-AC05-00OR22725 for the U.S. Department of Energy.

I would like to thank those individuals who helped significantly in my completion of my PhD in Electrical Engineering. First, I would like to thank Dr. Yoon Kang for his guidance and inspiration in pursuing my accelerator-related studies at the Spallation Neutron Source. I thank Dr. Aly E. Fathy for his excellent instruction in and out of the classroom and the long hours he put in to help me complete my research. I thank Dr. Cheng Wang for his very helpful and fruitful collaboration regarding mathematical methods in electromagnetics. I also thank Dr. Marshall Pace and Dr. Paul Crilly for serving on my committee.

I would also like to recognize other engineers and technicians at ORNL who were particularly helpful to me in completing my research: Tom Hardek, Rob Peglow, Ken Gawne, Sung-Woo Lee.

Finally, I wish to thank my parents, my wife Rebekah, and other friends whose encouragement made this work possible. Ultimately, I thank my God – "When I said, 'My foot is slipping,' Your love, O LORD, supported me."

Abstract

A new class of accelerating structures employing a uniformly twisted waveguide is investigated. Twisted waveguides of various cross-sectional geometries are considered and analyzed. It is shown that such a twisted waveguide can support waves that travel at a speed slower than the speed of light c. The slow-wave properties of twisted structures are of interest because these slow-wave electromagnetic fields can be used in applications such as electron traveling wave tubes and linear particle accelerators.

Since there is no exact closed form solution for the electromagnetic fields within a twisted waveguide or cavity, several previously proposed approximate methods are examined, and more efficient approaches are developed. It is found that the existing perturbation theory methods yield adequate results for slowly twisted structures; however, our efforts here are geared toward analyzing rapidly twisted structures using modified finite difference methods specially suited for twisted structures.

Although the method can handle general twisted structures, three particular cross sections are selected as representative cases for careful analysis. First, a slowly twisted rectangular cavity is analyzed as a reference case. This is because its shape is simple and perturbation theory already gives a good approximate solution for such slow twists rates. Secondly, a symmetrically notched circular cross section is investigated, since its longitudinal cross section is comparable to the well known disk-loaded cavity (used in many practical accelerator designs, including SLAC). Finally, a "dumbbell" shaped cross section is analyzed because of its similarity to the well-known TESLA-type accelerating cavity, which is of great importance because of its wide acceptance as a superconducting cavity.

To validate the results of the developed theory and our extensive simulations, the newly developed numerical models are compared to commercial codes. Also, several prototypes are developed employing the three basic shapes discussed previously. Bench measurements are performed on the prototype cavities to evaluate dispersion by measuring the field distribution along these cavities. The measurement results are compared to the simulations and theoretical results, and good agreement is shown. Once validated, the developed models are used to design twisted accelerating structures with specific phase velocities and good accelerating performance.

Contents

1 Introduction **1**

1.1 Background 1

1.2 Description of Twisted Structure 4

1.3 Contributions 6

2 Twisted Geometry **8**

2.1 Mathematical Description 8

2.1.1 Construction of a Helical Volume 8

2.1.2 Coordinate System Details 9

2.2 Helical Analogs to Non-Twisted Structures 12

2.3 Electromagnetic Modes in Twisted Structures 15

2.3.1 Boundary Conditions 15

2.3.2 Field Representation 16

2.4 Summary 17

3 Analysis Methods **18**

3.1 Straight Waveguide Equivalent 18

3.2 Analytic methods 22

3.2.1 Perturbation Theory (Rectangular Guide) 22

3.2.2 Helical Groove Waveguides 24

3.3 3D numerical methods 31

3.3.1 Boundary Treatment 32

3.3.2 Time Stepping and Stability 36

3.4 2D numerical methods 36

3.4.1 2D NFDTD Method 36

3.4.2 2D NFDFD Method 38

3.5 Extension to Arbitrary Cross Sections 41

3.6 Summary 42

4 Result Validation **44**
4.1 Existing Electromagnetics Software 44
4.2 Special Cases 45
4.3 Experimental Investigation 48
4.4 Summary 48

5 The Twisted Cavity as an Accelerating Structure **52**
5.1 Quantities of Interest for Accelerating Cavities 53
5.2 Advantages of Twisted Accelerating Structures 54
5.3 Twisted Disk-Loaded Accelerating Structure 56
5.4 The Disk-loaded Accelerating Structure: an Optimization Case Study 62
5.5 Twisted Elliptical (TESLA-type) Accelerating Structure 66

6 Experimental Investigation **76**
6.1 Twisted Rectangular Prototype 78
6.2 Twisted Disk-Loaded Analog Prototype 84
6.3 Twisted TESLA-type Prototype 88
6.4 Summary 92

7 Conclusion **94**

Bibliography **96**

Appendices **101**

A Selected Relevant Publications **102**

B Analysis of Rapidly Twisted Hollow Waveguides: Submitted to MTT Transactions **103**

C Applications of Twisted Hollow Waveguides as Accelerating Structures **114**

Vita **124**

List of Tables

1.1 Comparison of accelerating performance of several structures 3

4.1 Results for 3D NFDTD simulation of twisted waveguide 46

5.1 Parameters for the SLAC accelerating cavities 56
5.2 Comparison of disk loaded accelerating structures 60
5.3 Parameters for the SNS medium beta (beam beta = 0.61) accelerating cavity 72
5.4 Comparison of TESLA-type accelerating structures 74

6.1 Experimentally measured first four TE modes for the twisted rectangular prototype compared to 3D simulation method results. 81
6.2 Short and long prototype resonant frequencies compared to 2D simulation method results. 82
6.3 Parameters for twisted analog to disk-loaded accelerating cavity 84

List of Figures

1.1 Superconducting elliptical (TESLA) accelerating cavity. (from [1].) 2
1.2 A simple twisted rectangular geometry 5
1.3 Twisted rectangular waveguide: longitudinal cross section 5

2.1 End view of a twisted rectangular waveguide structure. Note that the cross section at each plane is a (rotated) rectangle. 10
2.2 An arbitrary straight waveguide and its transverse helical analog 13
2.3 A conventional disk-loaded slow-wave structure 13
2.4 A longitudinal helical analog to the disk-loaded slow-wave structure. (a) shows the transverse cross section, while (b) shows a cutaway view of the 3D twisted structure. 14

3.1 Example of a staircase mesh approximating a circular domain. 20
3.2 Typical dispersion curve of a twisted rectangular waveguide (solid line), compared to that of its transverse straight analog (dashed line), and the TEM limit (dotted line). 23
3.3 Helical groove waveguide geometry 25
3.4 Longitudinal cross section of the general helical groove waveguide problem 27
3.5 Cross sections for varying number of grooves 27
3.6 Dispersion curves for double helical groove waveguide. 30
3.7 log plot of magnitude of E_y at sample point using NFDTD simulation showing late-time instability. 33
3.8 Stability domain for Jameson method time integrator 37
3.9 "Collapsed" Yee grid used in the second order 2DNFDTD method. 39
3.10 Cascaded coordinate transformation used to analyze arbitrary twisted structures. . . 41
3.11 Keyhole cross section and corresponding mesh. 43

4.1 Dispersion relationship for 8.16 cm by 3.63 cm rectangular waveguide with twist rate of 30 $\frac{R}{m}$. 46
4.2 Simulated Ey multiplied by raised cosine window function, and corresponding spectrum. 47

4.3 Cutoff frequencies predicted for 8.16 cm by 3.63 cm rectangular waveguide. 49
4.4 Cutoff frequencies predicted for a single helical groove waveguide with varying twist rates. 50

5.1 Construction of the outline for a TESLA-type accelerating cavity 53
5.2 CST Simulation: Electric field in the SLAC Accelerating structure 57
5.3 CST Simulation: Electric field in the longitudinal helical analog to the SLAC Accelerating structure 58
5.4 CST Simulation of Twisted SLAC-type cavity: Electric field with increased outer radius 60
5.5 Magnitude of $\boldsymbol{E_z}$ for on-axis and off-axis particles: CST simulation 61
5.6 Predicted dispersion curves of the disk loaded twisted equivalent using the 2D frequency domain method for varying twist rates. 65
5.7 Simulated effect of changing the inner radius on $\frac{R}{Q}$. 67
5.8 Simulated frequency as a function of twist rate. (Phase velocity held equal to c.) . . 68
5.9 Simulated effect of changing m on $\frac{R}{Q}$. 69
5.10 Twisted cross section for longitudinal helical analog to TESLA structure. 70
5.11 Longitudinal cross section of twisted TESLA-type cavity. 71
5.12 CST simulation of an SNS superconducting three-cell half-cavity. 73
5.13 Electric field along a cross section of a helical TESLA-type cavity. 75

6.1 Bead and test setup for bead pull measurements. 77
6.2 Twisted rectangular waveguide prototype. 79
6.3 $|S_{21}|$ for the twisted rectangular prototype showing resonances. 81
6.4 Dispersion curves showing measured and predicted resonant frequencies for twisted rectangular cavity. 82
6.5 Bead pull measurement of the large twisted rectangular prototype for third mode. Measurements for other modes were similar, except with different number of cycles. . 83
6.6 Large twisted disk-loaded waveguide prototype. 85
6.7 Measured transmission spectrum of twisted analog of the disk-loaded cavity, showing resonances. 86
6.8 Measured field in the twisted analog of the disk-loaded cavity. 87
6.9 Predicted and measured dispersion curves for two modes of a twisted analog to a disk-loaded cavity. The mode with higher frequency is the TM accelerating mode. The x's are experimental points. 89
6.10 Large twisted TESLA-type waveguide prototype. 90
6.11 Measured transmission spectrum of twisted analog of the elliptical cavity, showing resonances. 91

6.12 Measured field in the twisted analog of the elliptical cavity. 93
6.13 Predicted and measured dispersion curves for the accelerating mode of an elliptical twisted guide. The x's are experimental points. 93

Chapter 1

Introduction

1.1 Background

It is a well known fact that straight hollow waveguides with a uniform cross section will only support electromagnetic waves whose phase velocity is greater than the speed of light. At the same time, many useful microwave devices depend on the interaction of charged particles with a certain electromagnetic mode. Such interaction can only happen effectively when the particles and the wave travel at almost the same speed. This is one reason why there has been interest in slow-wave electromagnetic structures, which support waves traveling at speeds slower than c.

A simple method for slowing the wave using a TM mode in a waveguide partially loaded with dielectric material has been thoroughly investigated [2–4]. Yet, the addition of dielectric material to the waveguide presents several challenges. It makes achieving a good vacuum much harder because of possible outgassing from the material. Also, dielectrics can be problematic if superconducting cavities are needed, since any dielectric has higher loss that can spoil the extremely high cavity Q. Therefore, slow wave structures with no dielectric loading are needed for superconducting cavities.

A conventional method for slowing the wave that is more well-suited for superconducting accelerators is to use a corrugated structure with nonuniform cross section. This is the idea behind many modern accelerating cavities, including the well-known disk-loaded accelerating cavity [5] and the elliptical, or TESLA type accelerating cavity [6]. (This accelerating structure is shown in Figure 1.1.) In these structures, the cross section gets wider and smaller along the axis of propagation, adding reactive loading and effectively slowing the wave. Although typical accelerators are operated in a standing wave mode, either standing wave or traveling wave modes can be of interest in these slow wave structures. Such a corrugated structure has often been treated as a chain of coupled L-C tank resonators, which provides a useful single-mode approximation if a full EM simulation (FE or FDTD) is not used (see [7], for example).

Although structures with nonuniform cross section are very useful for accelerators and traveling

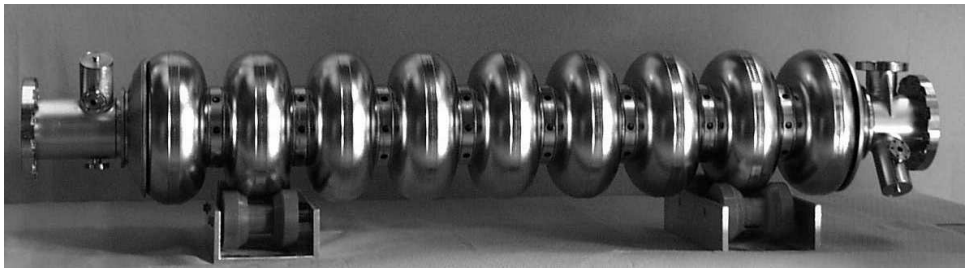

Figure 1.1: Superconducting elliptical (TESLA) accelerating cavity. (from [1].)

wave tubes, they also have some drawbacks. First, the manufacturing process often involves very difficult machining and welding to create the smooth finish necessary. This makes the cost of such cavities and waveguides a serious problem. Secondly, the electromagnetic wave will not propagate "smoothly" down the corrugated structures as it would with a straight waveguide (i.e. an $e^{-j\beta z}$ dependence cannot be assumed for the fields). Instead, the intensity of the wave would vary along the length of the guide, which adds complexity to the beam-wave interaction problem.

In this dissertation, I consider whether a uniform waveguide that is twisted along its axis could be used to address these difficulties. It has long been known that a twisted structure can be a slow wave structure, and a preliminary investigation into the feasibility of twisted guides as accelerating structures was undertaken by Kang [8]. Such a guide could be used without the problem of dielectric loading, and may also be easier to manufacture because of its uniform cross section.

Higher order mode (HOM) resonance is also an important and often problematic attribute of RF cavity structures, especially when they are used with charged particles. Any cavity or waveguide through which charged particles travel will support many higher order mode resonances in addition to the accelerating mode. Because higher order modes can interact with particles to cause instabilities in the beam, HOM dampers are often used to remove those HOMs that are dangerous to the particles. However, the HOMs may not always couple out successfully, since the boundary conditions that satisfy the resonance of the fundamental accelerating mode may not work favorably to the removal of certain HOMs. In other words, although HOM dampers are used to remove the HOMs, the coupling of many HOMs to the dampers can not be completely assured; some trapped modes may still exist inside the structure [9]. It is believed that the uniform cross section of a twisted waveguide may enable the HOMs to be coupled to the outside more easily, giving a better chance of HOM damping. Trapped HOM characteristics of twisted guides are investigated in this research.

Table 1.1 gives a comparison between several types of structures in terms of their performance as accelerating cavities. It is clear that finding a cavity that can meet all of the design criteria is a difficult task. We will investigate the twisted guide in detail to determine its performance with respect to these metrics.

Table 1.1: Comparison of accelerating performance of several structures

	Supports slow waves	**Vacuum/ Superconducting performance**	**Manufacturability**
Straight Guide	no	good	simple
Dielectric loaded guide	yes	poor	moderate
Reactively loaded cavity	yes	good	difficult
Twisted guide	yes	good	potentially simple

The modes supported by the twisted waveguides are obviously not simple TE or TM modes if a conventional orthogonal coordinates system is referenced. Determining the electromagnetic modal fields that are supported in the cavity/waveguide structure is important, since both the desired operating mode and other harmful modes can exist. The TM-like modes may be used for acceleration of charged particles. Other TE-like modes or hybrid modes need to be assessed to completely characterize the properties of the structure to be used with charged particles. The pass-band characteristics of the slow wave twisted waveguide structure also need to be investigated. These pass-band characteristics are important in the conventional corrugated or reactively loaded structures when selecting the operating mode and predicting the performance of the cavity structures. Pass-band characteristics also determine the matching of the phase velocity of the wave to the velocity of the particle. These properties of twisted waveguides are investigated in this research.

In this research, the design of twisted waveguides and cavities is focused on from the point of view of microwave engineering. The dynamics of the beam-wave interaction is not investigated, but rather left as an area of future research and investigation. In other words, the detailed effects of the beam on the cavity fields are not considered, and the exact influence of the cavity fields on particle dynamics is not considered.

1.2 Description of Twisted Structure

As previously mentioned, we are considering a twisted waveguide formed by extruding a certain cross section along a straight line while twisting. A simple example of a twisted rectangular guide is shown in Figure 1.2. A transverse cross section at any point on the axis of the guide will be a perfect rectangle. However, a longitudinal cross section will yield a much different shape, shown in Figure 1.3. This type of waveguide or cavity offers the possibility of much simpler manufacturing, as it could be formed through an extrusion or molding process without the need for multiple pieces joined together by difficult and expensive welds.

An analysis of twisted rectangular waveguides has been previously carried out by Lewin [10] and by Yabe and Mushiake [11, 12], who showed that such a twisted rectangular waveguide can support both slow and fast wave modes. In each of [10–12], perturbation theory is used to analyze the propagation characteristics of the dominant quasi-TE mode in the waveguide. It is well-known that in general, the more rapid the twist rate, the slower the phase velocity of the wave.

Obviously, the rectangular cross section is only one possible design based on a commonly used hollow waveguide. Any non-circular cross section will generate a nontrivial shape when twisted along the axis of propagation, which has the potential to produce slow-wave effects. However, this research will concentrate more on a few simple representative cross sectional shapes in order to give some examples of how the general methods proposed here can be applied.

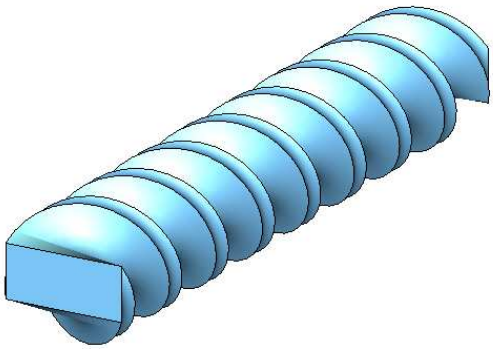

Figure 1.2: A simple twisted rectangular geometry

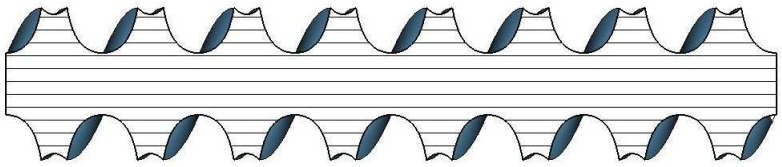

Figure 1.3: Twisted rectangular waveguide: longitudinal cross section

1.3 Contributions

In this dissertation, an overview of the twisted geometry and the modeling challenges associated with it is given. Then, it is shown how the finite difference method was chosen as the best way to analyze twisted guides. The specifics of the numerical implementation are discussed in detail. The developed methods are validated using commercial code, previously investigated special cases, and by experiment. Finally, these new methods are used to develop design guidelines for practical twisted accelerating structures.

Specifically, the contributions of the present research include the following:

i. Investigations on the accuracy limits of the existing perturbation theory and mode matching approaches.

ii. Investigation of similarities and differences between twisted waveguides and cavities, and conventional corrugated cell-type accelerating cavities.

iii. Development of a 3D fully nonorthogonal finite difference numerical scheme for the twisted rectangular waveguide, which could be generalized to non-rectangular geometries.

iv. Development of a 2D fully nonorthogonal finite difference time domain scheme or schemes for the twisted rectangular waveguide, which could be generalized to non-rectangular geometries.

v. Development of a 2D fully nonorthogonal finite difference frequency domain scheme or schemes for the twisted rectangular waveguide, which could be generalized to non-rectangular geometries.

vi. Experimental investigation of a few types of twisted geometries, including measurement of dispersion curves and internal electromagnetic fields.

vii. Investigation of end effects on twisted cavities of finite length.

viii. Development of design guidelines for accelerator cavities. Specifically, determining how to construct a helical slow wave structure that will produce a certain lowering of the phase velocity. A few other design factors for accelerating cavities will be considered in this research.

This research represents the first time an in-depth design method has been presented for a twisted accelerating structure, which is shown to have great promise. The design study was made possible by the novel approach of applying a 2D mesh to solve twisted structures, which significantly reduces computational effort compared to standard 3D methods. Also, the method of

handling boundary conditions to ensure late-time stability without sacrificing accuracy is new to this approach.

Chapter 2

Twisted Geometry

In this chapter, the theoretical foundation for the analysis of twisted structures is developed, and notation is introduced. The mathematics of differential geometry used in this section are well-known. However, the rules of differential geometry allow the development of an exact straight equivalent to any twisted structure through the use of anisotropic materials, which is new. The details of this equivalent and its consequences are discussed.

2.1 Mathematical Description

2.1.1 Construction of a Helical Volume

Let us assume that we have a 2D cross section defined by some implicit function of x and y, i.e. $f(x, y) < L$ for some constant L. An arbitrary straight cavity can be constructed by specifying a volume

$$\begin{aligned} f(x,y) &< L \\ z_{min} < z &< z_{max}. \end{aligned} \tag{2.1}$$

An arbitrary straight waveguide can be obtained by letting $z_{min} \to -\infty$ and $z_{max} \to +\infty$. In either case, it is assumed that the boundaries of the structure are perfectly conducting walls.

Now, we introduce the twisted (or helicoidal) coordinate transform employed by Lewin [10]. This is given by

$$\begin{aligned} x' &= x\cos pz + y\sin pz \\ y' &= y\cos pz - x\sin pz \\ z' &= z. \end{aligned} \tag{2.2}$$

Here, p is some constant twist rate. A twisted cavity can now be defined simply by

$$\begin{aligned} f(x', y') &< L \\ z_{min} < z' &< z_{max}. \end{aligned} \tag{2.3}$$

A twisted waveguide can be defined by sending the z limits to infinity. It should be noted that the transverse cross section of such a helical waveguide or cavity (i.e. cut across a $z = constant$ boundary) will always yield the same shape, although rotated about the line $x = 0, y = 0$. In this sense, the structure has a uniform cross section, only rotated along the axis. An end view of a twisted structure would reveal a circular inner hole. Figure 2.1 shows an end view of a twisted rectangular waveguide with the cross section shown at several different planes down the length of the guide.

2.1.2 Coordinate System Details

As discussed in [11, 12], the coordinate transformation of Equation 2.2 is not orthogonal. Its analysis will require the covariant and contravariant basis vectors to be defined. In keeping with the conventional notation of differential geometry, we will sometimes refer to the coordinate x' as x^1, y' as x^2, and z' as x^3. The corresponding covariant basis vectors will be denoted by $\mathbf{e_1}$, $\mathbf{e_2}$, and $\mathbf{e_3}$, and can be defined at any point in space using

$$\begin{aligned} \mathbf{e_1} &= \frac{\partial \mathbf{r}}{\partial x^1} \\ \mathbf{e_2} &= \frac{\partial \mathbf{r}}{\partial x^2} \\ \mathbf{e_3} &= \frac{\partial \mathbf{r}}{\partial x^3}. \end{aligned} \tag{2.4}$$

Here, $\mathbf{r}$ is an arbitrary vector. These basis vectors can be computed easily if the coordinate transform is defined. For example,

$$\begin{aligned} \frac{\partial \mathbf{r}}{\partial x^1} &= \frac{\partial \mathbf{r}}{\partial x}\frac{\partial x}{\partial x^1} + \frac{\partial \mathbf{r}}{\partial y}\frac{\partial y}{\partial x^1} + \frac{\partial \mathbf{r}}{\partial z}\frac{\partial z}{\partial x^1} \\ &= \hat{x}\frac{\partial x}{\partial x^1} + \hat{y}\frac{\partial y}{\partial x^1} + \hat{z}\frac{\partial z}{\partial x^1}. \end{aligned} \tag{2.5}$$

$\hat{x}$, $\hat{y}$, and $\hat{z}$ are the ordinary Cartesian basis vectors. The other basis vectors can be computed in a similar fashion. The dot products between the basis vectors can now be computed as well. Since the coordinate system of interest is nonorthogonal, there should be no expectation that $\mathbf{e_i} \cdot \mathbf{e_j} = \delta_{ij}$. Instead, the covariant metric tensor must be defined

$$g_{ij} = \mathbf{e_i} \cdot \mathbf{e_j} \tag{2.6}$$

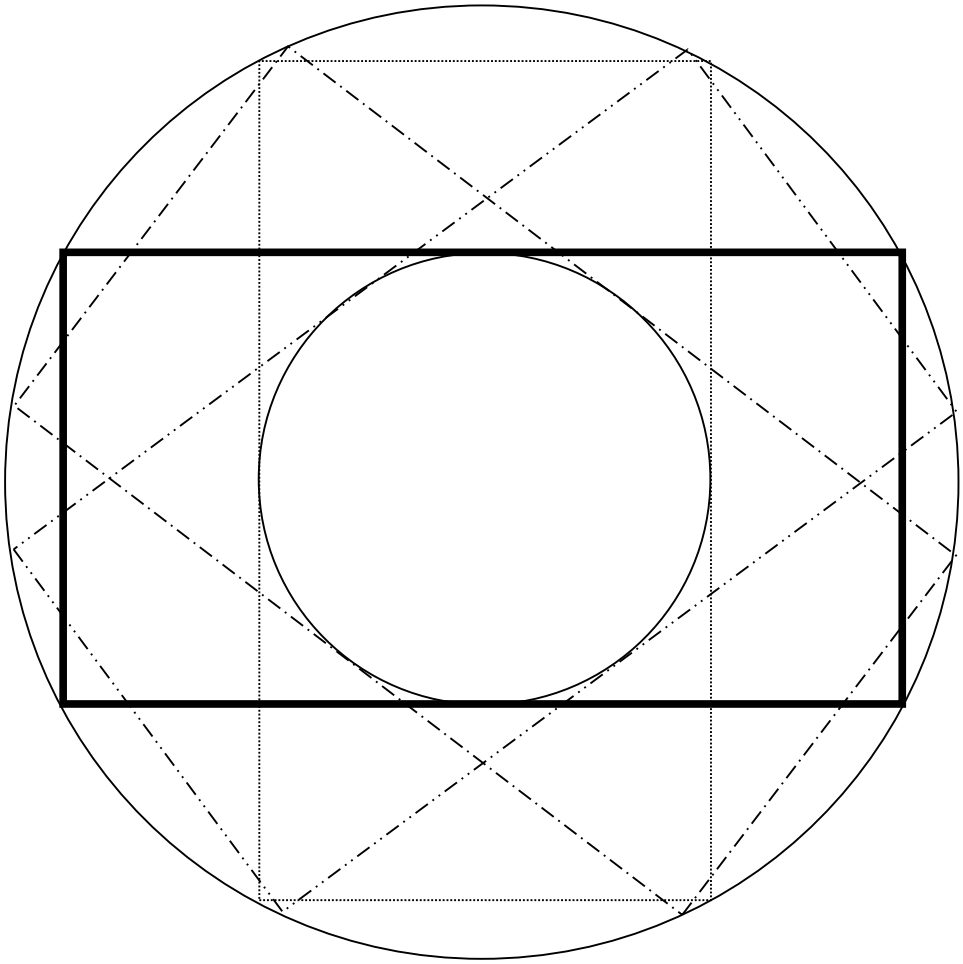

Figure 2.1: End view of a twisted rectangular waveguide structure. Note that the cross section at each plane is a (rotated) rectangle.

The matrix $[g_{ij}]$ will be symmetric, not just for the twisted coordinate system, but for any other curvilinear coordinate system. In the case of orthogonal coordinates, $[g_{ij}]$ should also be diagonal. For the twisted coordinate system of Equation 2.2, it can be shown from basic differential geometry that

$$[g_{ij}] = \begin{bmatrix} 1 & 0 & -py' \\ 0 & 1 & px' \\ -py' & px' & p^2(x'^2 + y'^2) + 1 \end{bmatrix}. \tag{2.7}$$

Note that as p tends to 0, $[g_{ij}]$ becomes the identity matrix, which is expected since in this case, the original Cartesian coordinate system is recovered.

In addition to the covariant basis vectors defined above, our analysis must also make use of contravariant basis vectors. These can be defined using

$$\begin{aligned} \mathbf{e^1} &= \nabla x^1 \\ \mathbf{e^2} &= \nabla x^2 \\ \mathbf{e^3} &= \nabla x^3. \end{aligned} \tag{2.8}$$

Following the usual convention, superscripts are used to refer to contravariant quantities, whereas subscripts are used to refer to covariant quantities. These contravariant vectors are perpendicular to surfaces of constant x^1, x^2, and x^3. The dot products of these vectors are given by the contravariant tensor metric.

$$g^{ij} = \mathbf{e^i} \cdot \mathbf{e^j} \tag{2.9}$$

By differential geometry, we have the relations

$$[g_{ij}]\left[g^{ij}\right] = I \tag{2.10}$$

$$\mathbf{e^i} \cdot \mathbf{e_j} = \delta_{ij}. \tag{2.11}$$

For more details, refer to any classic text on differential geometry, such as [13].

It is possible to represent any vector as a linear combination of either covariant or contravariant basis vectors, and in the analysis to follow, it will be necessary to use both representations. For example, the electric field $\mathbf{E}$ can be expressed as

$$\begin{aligned} \mathbf{E} &= E^1\mathbf{e_1} + E^2\mathbf{e_2} + E^3\mathbf{e_3} \\ \mathbf{E} &= E_1\mathbf{e^1} + E_2\mathbf{e^2} + E_3\mathbf{e^3} \end{aligned} \tag{2.12}$$

along covariant and contravariant basis vectors, respectively. It is also possible to convert between

covariant and contravariant vector representations, as the components transform as

$$E_i = g_{ij}E^j, E^i = g^{ij}E_j. \tag{2.13}$$

Here, the Einstein summation convention is used, meaning that a sum over the index j is assumed. (This summing convention will be assumed throughout this text, unless otherwise stated.) Obviously, converting covariant components to contravariant components can be done in the same manner, using the elements of $\left[g^{ij}\right]$ instead.

2.2 Helical Analogs to Non-Twisted Structures

Using the transformation of Equation 2.2, it is possible to define a twisted structure which is analogous to a straight structure in that an arbitrary cross section in the transverse plane will yield the same shape. Figure 2.2 shows an arbitrary straight waveguide, and its corresponding twisted analog after applying the coordinate transformation. These analogs are important in defining the electromagnetic properties of a structure, since we expect that in the limit as $p \to 0$, we will recover the same fields as those in the straight waveguide or cavity. We will refer to these structures as transverse helical analogs. Comparisons between a given straight waveguide and its transverse helical analog are performed in this research.

There is also another important analog between twisted and non-twisted structures that is useful for comparing a rotationally symmetric slow wave structure to a twisted structure. Consider, for example, a disk-loaded slow-wave waveguide. A longitudinal cutaway view of such a structure is shown in Figure 2.3. If we define a "keyhole" transverse cross section as shown in Figure 2.4a, we can use this 2D cross section to generate a twisted geometry as discussed above. Upon examining the longitudinal cross section of this geometry in Figure 2.4b, it can be seen to be identical to the disk-loaded structure. Therefore, these structures will be referred to as longitudinal helical analogs.

As may be inferred intuitively, it can also be shown mathematically that the total volume of a straight cavity is the same as the volume of its transverse helical analog; similarly, the total volume of a rotationally symmetric cavity is the same as the volume of its longitudinal helical analog. The fact that the volume is automatically the same between a helical structure and its analog further facilitates a meaningful comparison.

A longitudinal helical analog can be constructed in the following fashion. Assume we have a rotationally symmetric structure defined by

$$\rho < g(z), \tag{2.14}$$

where g is some periodic function with periodicity Δz. We define a 2D transverse cross section in

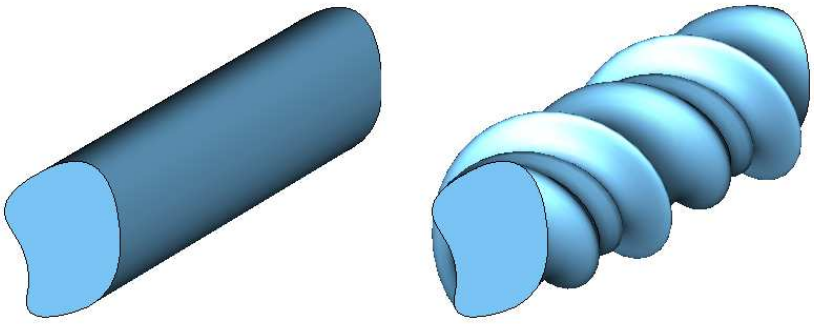

Figure 2.2: An arbitrary straight waveguide and its transverse helical analog

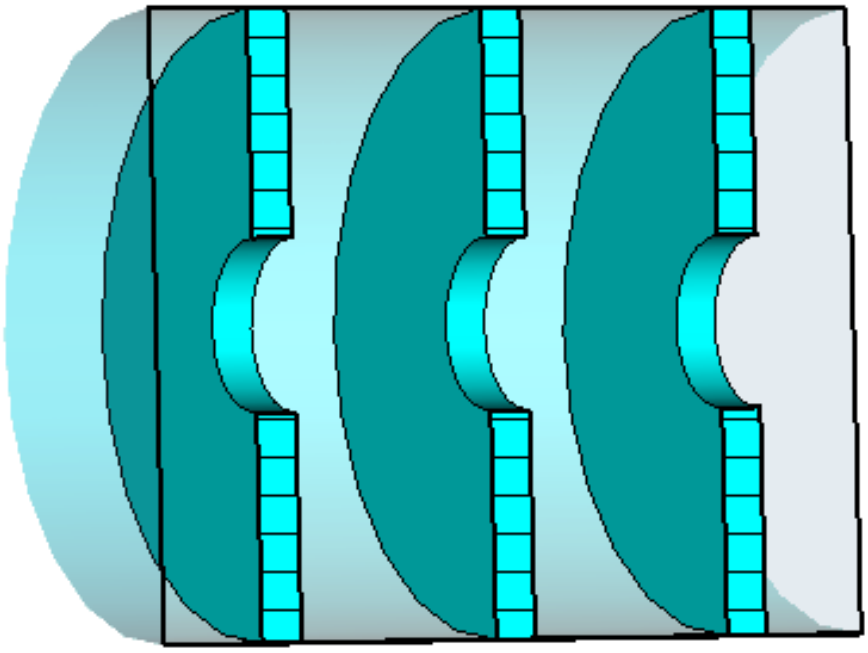

Figure 2.3: A conventional disk-loaded slow-wave structure

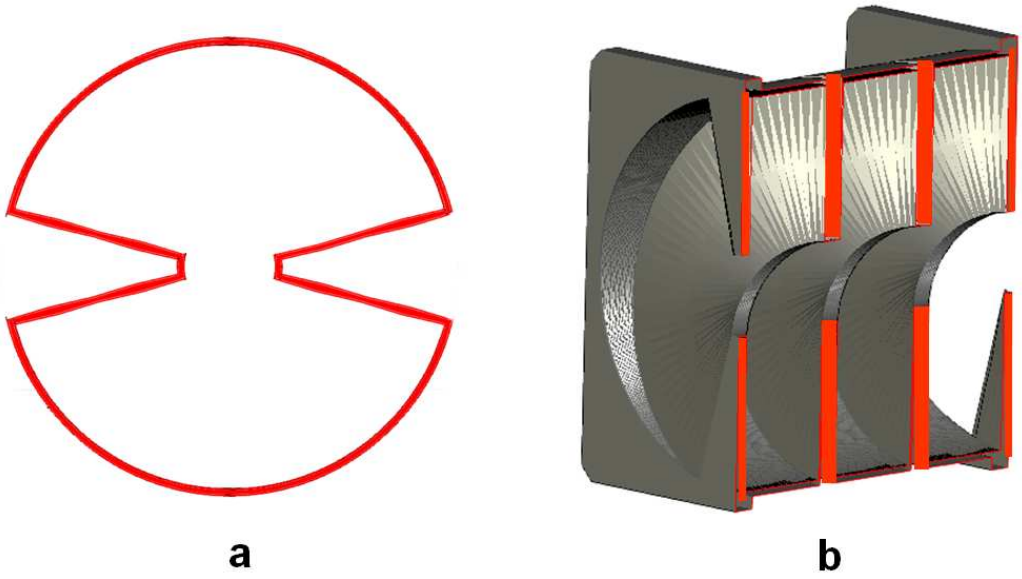

Figure 2.4: A longitudinal helical analog to the disk-loaded slow-wave structure. (a) shows the transverse cross section, while (b) shows a cutaway view of the 3D twisted structure.

polar coordinates (ρ, ϕ).

$$\rho(x,y) < g\left(\frac{\phi(x,y)\Delta z}{\pi}\right) \tag{2.15}$$

and set the twist rate

$$p = \frac{\pi}{\Delta z}. \tag{2.16}$$

The transformation of Equation 2.2 is then used to generate the analog. The longitudinal helical analog also allows some interesting comparisons to be made between twisted and rotationally symmetric non-twisted structures, as both can be used as slow wave structures.

The longitudinal helical analog defined above is not unique. It is easily observed that any two dimensional profile defined by

$$\rho(x,y) < g\left(\frac{m\phi(x,y)\Delta z}{2\pi}\right) \tag{2.17}$$

and twist rate

$$p = \frac{2\pi}{m\Delta z} \tag{2.18}$$

has an identical longitudinal cross section to the original rotationally symmetric structure for any even integer m. Although the longitudinal cross section of the generated structure will be the same for any even integer m, the slow wave performance may be quite different with different m values, which will be shown later on.

2.3 Electromagnetic Modes in Twisted Structures

2.3.1 Boundary Conditions

If we again use the twisted Cartesian coordinate system of Equation 2.2, the boundary conditions assuming perfectly conducting walls can be expressed simply. For the electric field, we have $\mathbf{E_t} = 0$, indicating that only a normal component of the electric field is allowed. Assume, for example, that an $x^1 = x' = constant$ boundary is under consideration. Since the basis vector $\mathbf{e^1}$ is normal to this surface already, the contravariant basis vector representation is the natural choice, immediately yielding

$$\begin{aligned} \mathbf{E} &= E_1\mathbf{e^1} \\ E_2 &= E_3 = 0. \end{aligned} \tag{2.19}$$

By permuting the indices, the boundary conditions for the $y' = constant$ and $z' = constant$ surfaces can be obtained in a similar fashion.

For the magnetic field, the perfectly conducting boundary condition requires that the normal component of $\mathbf{H}$ be zero. This indicates that the field must lie entirely along the basis vectors that

are tangential to the surface. If an x' boundary is considered, the covariant basis vectors $\mathbf{e_2}$ and $\mathbf{e_3}$ are tangential to the boundary surface. This gives

$$\begin{aligned} \mathbf{H} &= H^2\mathbf{e_2} + H^3\mathbf{e_3} \\ H^1 &= 0. \end{aligned} \tag{2.20}$$

2.3.2 Field Representation

Because the twisted waveguides under consideration are periodic in z, Floquet's theorem predicts that the fields will also have the same periodicity, except for a multiplicative phase factor. In this case, the period of the twisted waveguide will be $2\pi/p$. However, for the case of a uniformly twisted waveguide, it turns out that an even stronger statement can be made.

Assume the fields at some $z = z_0$ are known. Moving a distance dz along the axis of the twisted structure, the structure is exactly the same except for some rotation of angle $p\,dz$. Therefore, as shown in [14] for structures having "screw symmetry", the fields should be the same except for a phase factor $\phi\,dz$. This relation holds true for *any* dz, not just $dz = 2\pi/p$. In particular, we can send dz to zero and discover that for an infinite twisted waveguide, the variation of the fields along the axis of propagation involves only simple phase variation. In other words, except for the constant rotation of the fields, the z dependence can be factored out as $e^{-j\beta z}$ for some β. In terms of the twisted coordinates,

$$\mathbf{E}(x', y', z') = \mathbf{E_0}(x', y')e^{-j\beta z'} \tag{2.21}$$

In Equation 2.21, it was possible to replace $e^{-j\beta z}$ with $e^{-j\beta z'}$, since z and z' are numerically equal. Similar relations hold for $\mathbf{H}$. Thus, if a twisted coordinate system is used, the fields can be represented in much the same fashion as for an infinite straight waveguide. Another (more mathematical) way of showing this equivalence between straight and twisted fields in waveguides will be shown in Section 3.1. Obviously, these relations will not hold precisely if the structure is not infinite in extent. If a finite waveguide or cavity is considered, end effects must be taken into account, but the infinite approximation is often good enough to be very useful. Also, if a twisted cavity is considered instead of a waveguide, sin and cos functions should be used for the z' dependence rather than exponentials.

In addition to simplifying the analysis greatly, this property of the uniformity of the fields along the axis of propagation also provides practical advantages for several types of slow-wave structures. Whereas in a conventional slow-wave structure (like a corrugated or iris-loaded waveguide) the magnitude of the fields varies along the axis, there is no magnitude variation in an infinite twisted structure – only a phase variation. These advantages will be explored in greater detail later.

2.4 Summary

The geometry of twisted structures has been investigated. It is found that by using a coordinate transform, the boundary conditions can be expressed in a very simple fashion. Moreover, the coordinate transform offers a simple way to represent the fields in a twisted structure, allowing the longitudinal dependence of the fields to be factored out. This separation of the longitudinal coordinate will be key to the development of numerical methods to solve twisted structures.

The concept of helical analogs to nontwisted structures has been introduced. The two major analogs that we considered are transverse helical analogs and longitudinal helical analogs. For a transverse helical analog, the cross section in any transverse plane will be a twisted version of the corresponding cross section of the straight reference structure. For a longitudinal helical analog, the cross section in any longitudinal plane will be identical to the rotationally symmetric reference structure. These analogs are tools that will give us some intuition when comparing twisted waveguides and cavities to other, more well-known structures.

Chapter 3

Analysis Methods

Both analytic and numerical methods exist for the solution of twisted waveguides and cavities. Several analytic methods already exist based on the perturbation theory of [10–12] or field matching in a periodic structure [15–17]. Such methods yield closed form solutions for a limited class of these twisted structures, and can give some physical insight into the propagation characteristics of twisted structures. However, since these methods can only be used to solve a relatively small class of problems, numerical methods will also be investigated.

The numerical methods for investigating twisted waveguides and cavities can be divided into two main groups: 2D methods and 3D methods. 2D methods make use of assumed longitudinal dependence of the fields, and thus will yield good results for very long waveguides or cavities. In 2D analysis, end effects cannot be taken into account. On the other hand, 3D methods allow the calculation of the fields everywhere in the three dimensional domain including all end effects, at the expense of many more calculation points.

In this section, existing analytic and numerical methods will be investigated. The shortcomings of existing methods are presented, and new techniques are developed that address the limitations of these existing methods.

3.1 Straight Waveguide Equivalent

It has been recently pointed out by Shyroki [18] that there exists an exact equivalent for twisted and bent waveguide structures, based on the coordinate transformation properties discussed by Nicolet, Zolla, Agha, and Guenneau [19,20]. The essence of this transformation is to replace the twisted (or bent) waveguide with a straight waveguide whose transverse cross section is identical to the twisted one, but whose volume is filled with a nonuniform anisotropic material. This alone does not make the problem any easier, but for uniformly twisted structures it will be shown that the anisotropic permeability and permittivity are not functions of the z coordinate (i.e. not z-dependent). This allows much of the same machinery previously used to solve two-dimensional propagation problems

to be brought to bear on twisted waveguide problems.

Shyroki's recent research [18], which was done independently of this research, bears a number of similarities to the proposed methods, yet there are several areas of difference as well. First, [18] provides no experimental validation of the given theoretical results. Second, the application of two or three dimensional finite-difference time domain methods to solve twisted waveguide problems is not discussed, only frequency domain methods. Also, the handling of non-rectangular cross sections is not explicitly considered.

As an example for the twisted rectangular waveguide of interest, the coordinate system of Equation 2.2 is used and the boundary surfaces can be expressed as

$$\begin{aligned} x' = 0, x' = a \\ y' = 0, y' = b \end{aligned} \tag{3.1}$$

Obviously, other twisted cross sections can be analyzed by defining a different twisted coordinate system or by using Equation 2.2 and a "staircase-type" mesh. An example of such a staircase mesh is shown in Figure 3.1 for a circular shape. Any non-rectangular cross section in [18] must be treated using a staircase-type mesh. However, such a mesh has been shown be less accurate than a curvilinear mesh for a given mesh size [21]. Later on, we will discuss how the present numerical scheme can be used to solve twisted guides of arbitrary cross sections without resorting to a staircase-type mesh.

The problem now becomes one of computing the spatial derivatives used to find $\nabla \times \mathbf{E}$ and $\nabla \times \mathbf{H}$. It has been shown in [22] that the curl in nonorthogonal curvilinear coordinates can be expressed in a very similar fashion to Cartesian coordinates:

$$\nabla \times \mathbf{A} = g^{-\frac{1}{2}} \begin{vmatrix} \mathbf{e_1} & \mathbf{e_2} & \mathbf{e_3} \\ \dfrac{\partial}{\partial x^1} & \dfrac{\partial}{\partial x^2} & \dfrac{\partial}{\partial x^3} \\ A_1 & A_2 & A_3 \end{vmatrix}. \tag{3.2}$$

g is simply the determinant of the covariant metric tensor $[g_{ij}]$. However, this formula gives the contravariant components of the curl. Since the formula requires the input vector field $\mathbf{A}$ to be expressed in covariant components, a conversion will be necessary at each time stage.

The simple form of Equation 3.2 suggests an interesting equivalent structure which may be used to solve curved and twisted structures by transforming them to a straight structure. Maxwell's

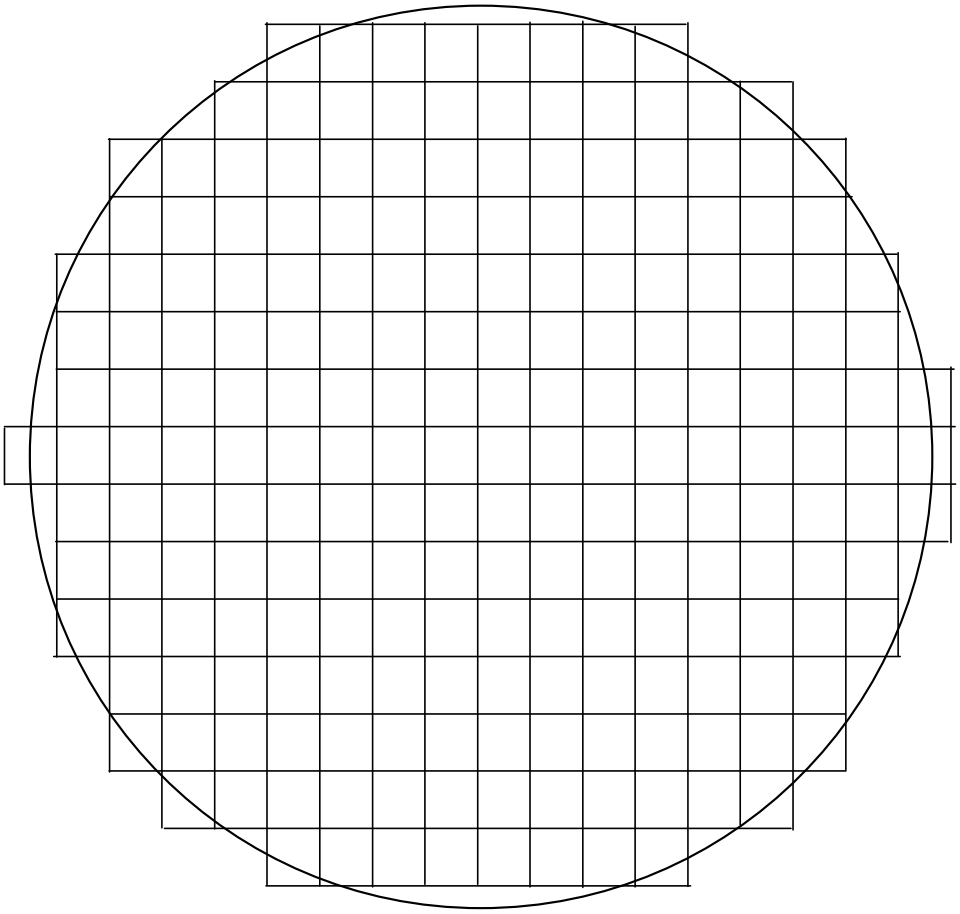

Figure 3.1: Example of a staircase mesh approximating a circular domain.

equations in empty space are first expressed along a contravariant basis:

$$\begin{aligned}(\nabla \times \mathbf{E}) \cdot \mathbf{e^i} &= -\mu_0 \frac{\partial H^i}{\partial t} \\ (\nabla \times \mathbf{H}) \cdot \mathbf{e^i} &= \epsilon_0 \frac{\partial E^i}{\partial t}.\end{aligned} \tag{3.3}$$

Then, using Equation 3.2,

$$\begin{aligned}\frac{1}{\sqrt{g}} \nabla_{c,i} \left(E_1, E_2, E_3\right) &= -\mu_0 \frac{\partial H^i}{\partial t} \\ \frac{1}{\sqrt{g}} \nabla_{c,i} \left(H_1, H_2, H_3\right) &= \epsilon_0 \frac{\partial E^i}{\partial t}\end{aligned} \tag{3.4}$$

where $\nabla_{c,i}$ returns the i component of the Cartesian curl operator operating on the following three components. Thus, we have

$$\begin{aligned}\frac{1}{\sqrt{g}} \nabla_{c,i} \left(E_1, E_2, E_3\right) &= -\mu_0 \frac{\partial H_j g^{ij}}{\partial t} \\ &= -\mu_0 g^{ij} \frac{\partial H_j}{\partial t}\end{aligned} \tag{3.5}$$

$$\begin{aligned}\frac{1}{\sqrt{g}} \nabla_{c,i} \left(H_1, H_2, H_3\right) &= \epsilon_0 \frac{\partial E_j g^{ij}}{\partial t} \\ &= \epsilon_0 g^{ij} \frac{\partial E_j}{\partial t}.\end{aligned} \tag{3.6}$$

If we substitute

$$\begin{aligned}\bar{\mu}^{ij} &= \mu_0 g^{ij} \sqrt{g} \\ \bar{\epsilon}^{ij} &= \epsilon_0 g^{ij} \sqrt{g},\end{aligned} \tag{3.7}$$

the problem becomes one of solving Maxwell's equations in ordinary Cartesian coordinates in a nontwisted structure, but subject to an anisotropic permittivity and permeability. The x, y, and z components of the solution fields correspond to the covariant components of the fields in the original twisted structure. This transformation makes the problem more intuitive by connecting it to another class of electromagnetic problems. Also, note that the spatial variation in the material parameters depends only on the metric tensor. Since the metric tensor for the twisted coordinate system is given by Equation 2.7, which only depends on the transformed x and y coordinates, the material has no variation along the longitudinal direction, as mentioned earlier.

Assuming the fields can be solved in this manner, the results can be converted back into Cartesian coordinates as follows. In the transformed (straight waveguide) problem, we can express

$$\mathbf{E} = E_1\mathbf{e^1} + E_2\mathbf{e^2} + E_3\mathbf{e^3}. \tag{3.8}$$

Taking dot products of this equation with $\hat{x}$, $\hat{y}$, and $\hat{z}$ results in

$$\begin{bmatrix} E_x \\ E_y \\ E_z \end{bmatrix} = \begin{bmatrix} \mathbf{e^1}\cdot\hat{x} & \mathbf{e^2}\cdot\hat{x} & \mathbf{e^3}\cdot\hat{x} \\ \mathbf{e^1}\cdot\hat{y} & \mathbf{e^2}\cdot\hat{y} & \mathbf{e^3}\cdot\hat{y} \\ \mathbf{e^1}\cdot\hat{z} & \mathbf{e^2}\cdot\hat{z} & \mathbf{e^3}\cdot\hat{z} \end{bmatrix} \begin{bmatrix} E_1 \\ E_2 \\ E_3 \end{bmatrix}. \tag{3.9}$$

By the definition of the contravariant basis vector

$$\mathbf{e^i} = \nabla x_i', \tag{3.10}$$

we can rewrite (3.9) as

$$\begin{bmatrix} E_x \\ E_y \\ E_z \end{bmatrix} = \begin{bmatrix} \frac{\partial x'}{\partial x} & \frac{\partial y'}{\partial x} & \frac{\partial z'}{\partial x} \\ \frac{\partial x'}{\partial y} & \frac{\partial y'}{\partial y} & \frac{\partial z'}{\partial y} \\ \frac{\partial x'}{\partial z} & \frac{\partial y'}{\partial z} & \frac{\partial z'}{\partial z} \end{bmatrix} \begin{bmatrix} E_1 \\ E_2 \\ E_3 \end{bmatrix} = \begin{bmatrix} \cos(pz') & -\sin(pz') & 0 \\ \sin(pz') & \cos(pz') & 0 \\ py' & -px' & 1 \end{bmatrix} \begin{bmatrix} E_1 \\ E_2 \\ E_3 \end{bmatrix}. \tag{3.11}$$

3.2 Analytic methods

3.2.1 Perturbation Theory (Rectangular Guide)

Lewin originally developed a solution for electromagnetic fields in a slowly twisted rectangular (and square) waveguide [10]. Because a slow twist rate was assumed, perturbation theory can be used since the fields are close to the fields in a transverse straight analog (in this case a straight rectangular waveguide). Only the dominant TE-like mode was investigated. Yabe and Mushiake later refined Lewin's original theory, correctly pointing out that the dominant TE-like mode in a straight waveguide becomes a hybrid mode when the waveguide is twisted [11]. Depending on the twist rate and the frequency, the wave can be either slow or fast. The formulas in [12] typically give dispersion curves similar to that in Figure 3.2. The dispersion curve is compared to the curve for a straight rectangular waveguide.

There are a few general observations that can be made from these dispersion curves. First, the cutoff frequency of the dominant TE-like mode in a straight waveguide will be lower than that of its transverse helical analog. Also, for low frequencies, the dominant TE-like mode of a twisted waveguide travels faster than the analogous mode in a straight waveguide. However, at higher frequencies, the dominant mode will be slower in the twisted structure and, at some point, the curve crosses the TEM asymptote – indicating slow-wave operation. In general, the higher the twist rate, the sooner the dispersion curve crosses the TEM limit and the lower the frequency at which the waveguide becomes slow wave.

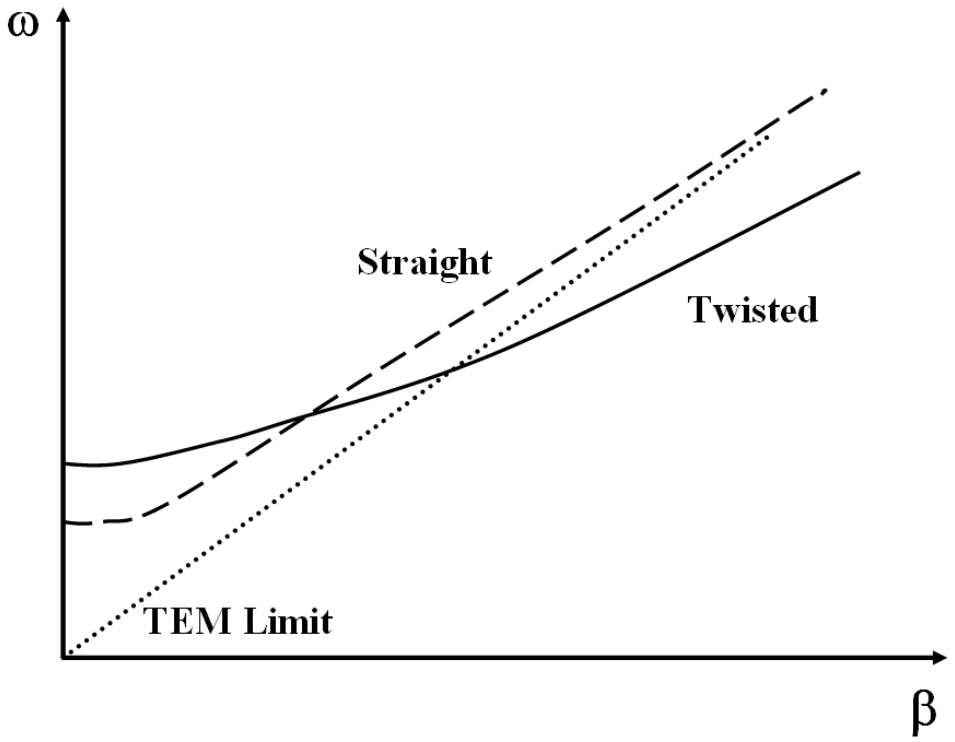

Figure 3.2: Typical dispersion curve of a twisted rectangular waveguide (solid line), compared to that of its transverse straight analog (dashed line), and the TEM limit (dotted line).

However, the perturbation theory approach also has additional serious limitations. First, the more rapid the twist rate, the less accurate the perturbation theory predictions found in [10] and [11,12]. This is due to the fact that the perturbation parameter p becomes large for rapid twist rates, so higher order corrections to the fields would have to be taken into account. Yet, the case of rapid twist rate is of interest in slow-wave applications, and so this case is investigated here. The precise range of twist rates over which perturbation theory is valid will be discussed in detail in Chapter 4. In this dissertation, when we speak of "slow twist rates", we refer to those cases where perturbation theory is generally valid, meaning that the product of the twist rate and the largest cross sectional dimension is less than 1.

Another limitation of Lewin's theory is that it is only suited for analyzing the dominant TE-like mode in an infinite rectangular twisted guide. Unfortunately, the dominant TE-like mode will have little practical application in accelerator applications since E_z, the z component of the electric field, will be very small. However, it should be noted that microwave undulators or deflecting cavities may use TE-like modes to produce a transverse deflection of the charged particle beam (without accelerating the particles). Finally, the perturbation theory approach cannot take end effects into account in a twisted cavity of finite length. As a result, it is necessary to have a more general theory of wave propagation in these twisted structures.

3.2.2 Helical Groove Waveguides

One type of rapidly twisted structure that has been examined analytically is the helical groove slow-wave structure, shown in Figure 3.3. Investigated by Flouds and Mansell in [15], the structure was of interest as a slow-wave structure for traveling wave tubes (TWT). The analysis was later extended by Wang, Yu, and Wei to include ridges in the step [16]. The theory was also extended to grooves of more arbitrary shape [17]. A single TE mode was assumed to exist in the groove region, and the pitch angle of the helix was assumed to be small (which corresponds to a high value for the twist rate p). In the center region, cylindrical solutions to the wave equation are assumed, and the coefficients are solved by matching the electric and magnetic fields at the opening of the groove. The result of this analysis is a theoretical prediction of the dispersion curves of the helical groove waveguide.

Note that this helical groove structure is very similar but not identical to the longitudinal helical analog to the disk-loaded waveguide structure shown in Figure 2.4. Since the disk-loaded waveguide is frequently used in particle accelerator applications, an extension of the theory of [15] is undertaken. We define the cross section using the method in Section 2.2. In this case, the transverse cross section of the helical structure should be defined in polar coordinates (ρ, ϕ) as

$$\rho < g\left(\frac{N_g \phi l_{cell}}{2\pi}\right) \tag{3.12}$$

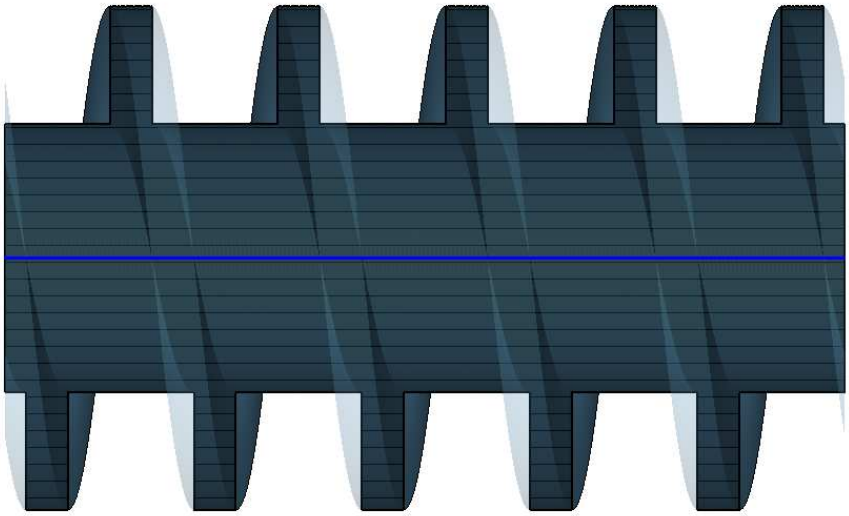

Figure 3.3: Helical groove waveguide geometry

where

$$g(z) = \begin{cases} r_a, & 0 < z < \dfrac{\Delta z}{N_g} - w \\ r_b, & \dfrac{\Delta z}{N_g} - w < z < \dfrac{\Delta z}{N_g} \end{cases} \tag{3.13}$$

Here, r_a is the disk radius, w is the groove width, r_b is the cell radius, Δz is the length of one complete twist, and N_g is the number of distinct grooves. It is assumed that $g(z)$ is periodic with period $\dfrac{\Delta z}{N_g}$. This mathematically defines the "keyhole" cross section. The curve swept out in the longitudinal cross section is shown in Figure 3.4, while Figure 3.5 shows the transverses and longitudinal cross sections for $1 < N_g < 4$. For the case $N_g = 1$, the helical groove waveguide of Flouds and Mansell is recovered. For any even integer N_g, the longitudinal cross section is identical to the disk-loaded waveguide. Our aim here is to extend this analysis for any N_g. Obviously, this method will only yield solutions for a limited type of cross section, but it is useful as a representative case of twisted guides.

Following the method of Wang, Yu, and Wei [16], we begin by expanding the fields in the cylindrical interaction region in terms of space harmonics:

$$\begin{aligned}
E_z^I &= \sum_{n=-\infty,\text{n multiple of } N_g}^{\infty} A_n^I \gamma_n^2 J_n(\gamma_n r) e^{j(n\phi - \beta_n z)} \\
E_r^I &= \pm j \sum_{n=-\infty,\text{n multiple of } N_g}^{\infty} \left[A_n^I \gamma_n \beta_n J_n'(\gamma_n r) - B_n^I \frac{n\omega\mu_0}{r} J_n(\gamma_n r) \right] e^{j(n\phi - \beta_n z)} \\
E_\phi^I &= \mp \sum_{n=-\infty,\text{n multiple of } N_g}^{\infty} \left[A_n^I \frac{n\beta_n}{r} J_n(\gamma_n r) - B_n^I \omega\mu_0 \gamma_n J_n'(\gamma_n r) \right] e^{j(n\phi - \beta_n z)} \\
H_z^I &= j \sum_{n=-\infty,\text{n multiple of } N_g}^{\infty} B_n^I \gamma_n^2 J_n(\gamma_n r) e^{j(n\phi - \beta_n z)} \\
H_r^I &= \pm \sum_{n=-\infty,\text{n multiple of } N_g}^{\infty} \left[A_n^I \frac{nk^2}{r\omega\mu_0} J_n(\gamma_n r) - B_n^I \gamma_n \beta_n J_n'(\gamma_n r) \right] e^{j(n\phi - \beta_n z)} \\
H_\phi^I &= \pm j \sum_{n=-\infty,\text{n multiple of } N_g}^{\infty} \left[A_n^I \frac{k^2 \gamma_n}{\omega\mu_0} J_n'(\gamma_n r) - B_n^I \frac{n\beta_n}{r} J_n(\gamma_n r) \right] e^{j(n\phi - \beta_n z)}.
\end{aligned} \tag{3.14}$$

Here,

$$\beta_n = \beta_0 + \frac{2n\pi}{\Delta z}. \tag{3.15}$$

These expressions are identical to those in Wang, Yu, and Wei except that here only those harmonics with values of n that are multiples of N_g are allowed. This is because for the symmetric multi-groove structure, Floquet's Theorem demands that the fields must be periodic with period $\dfrac{\Delta z}{N_g}$

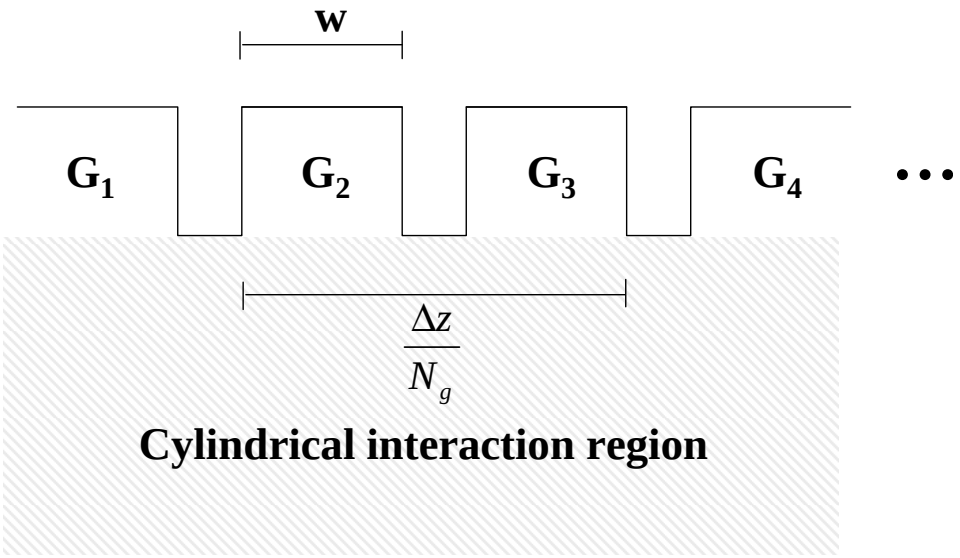

Figure 3.4: Longitudinal cross section of the general helical groove waveguide problem

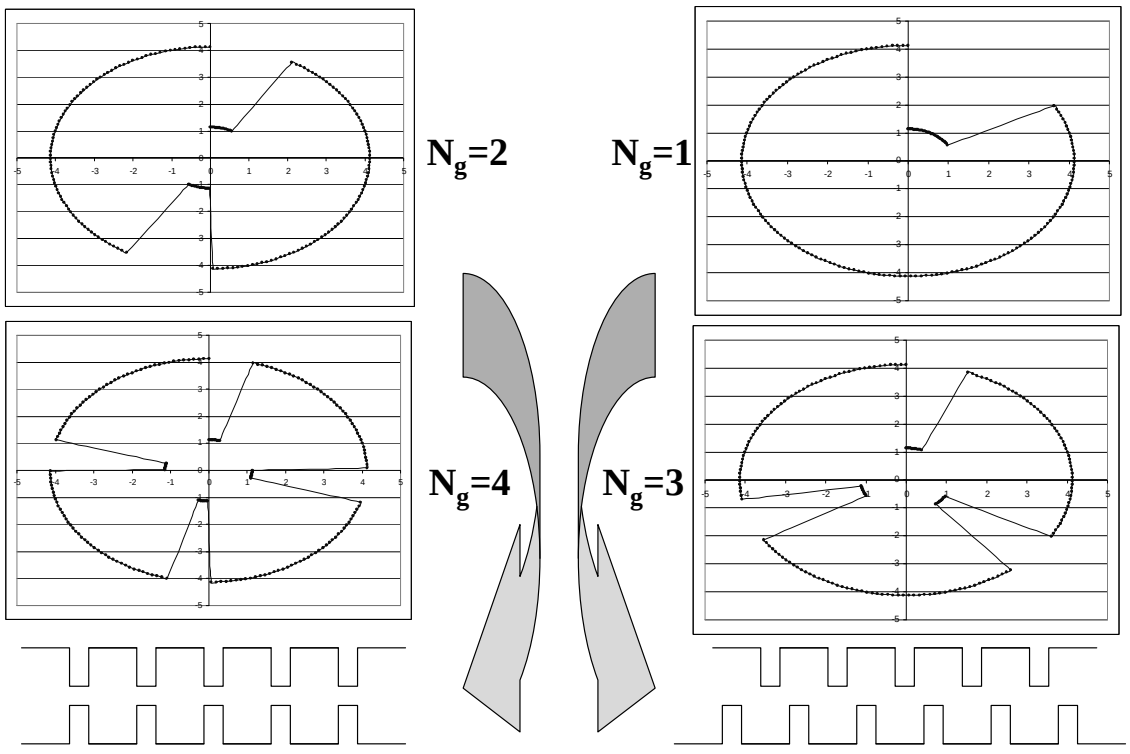

Figure 3.5: Cross sections for varying number of grooves

rather than the original period Δz.

In the groove regions, we assume a single TE mode whose electric field lies perpendicular to the groove, in a direction denoted by ξ, which will have a component along both the ϕ and z directions in cylindrical coordinates. In other words, we employ the coordinate transformation

$$\rho = r \tag{3.16}$$
$$\phi = \theta$$
$$z = \xi + \frac{\theta}{2\pi}\Delta z. \tag{3.17}$$

Using this transformation and resolving the components along appropriate unit vectors, the fields in the first groove can be expressed:

$$\begin{aligned} E_{\xi}^{G_1} &= \left[B^g Y_\nu(kr) - A^g J_\nu(kr)\right] e^{-j\nu\theta} \\ H_r^{G_1} &= \frac{\nu}{r\omega\mu_0}\left[B^g Y_\nu(kr) - A^g J_\nu(kr)\right] e^{-j\nu\theta} \\ H_\theta^{G_1} &= -j\frac{k}{\omega\mu_0}\left[B^g Y_\nu'(kr) - A^g J_\nu'(kr)\right] e^{-j\nu\theta} \\ E_r^{G_1} &= E_\theta^{G_1} = H_\xi^{G_1} = 0, \end{aligned} \tag{3.18}$$

where

$$\nu = \frac{\beta_0 \Delta z}{2\pi}. \tag{3.19}$$

Here, we have resolved along the contravariant ξ unit vector and the covariant θ unit vector in order to ensure their orthogonality. Once the fields in the first groove are expressed, the fields in each additional groove can be determined from Floquet's Theorem:

$$\mathbf{E^{G_i}} = \mathbf{E^{G_1}} e^{-j\beta_0 \Delta z (i-1)/N_g}. \tag{3.20}$$

Matching the fields in the groove regions to the fields in the cylindrical interaction region at $r = r_a$,

$$\begin{aligned} E_z^I &= E_\xi^{G_i} \cos\psi \\ E_\phi^I &= -E_\xi^{G_i} \sin\psi, \end{aligned} \tag{3.21}$$

where ψ, the pitch angle at radius r_a, is related to the twist rate p by

$$\tan\psi = \frac{\Delta z}{2\pi r_a}. \tag{3.22}$$

In order to match the electric fields at the interface, the fields on both sides of the matching

conditions are tested with the basis functions

$$e_m = e^{-j(\beta_0 z + 2\pi m z/\Delta z - m\phi)}, \tag{3.23}$$

leading to

$$\begin{aligned} A_m^I &= \frac{[B_g Y_\nu(kr_a) - A_g J_\nu(kr_a)]\sin[(m+\nu)\pi w/\Delta z]\cos\psi}{\pi(m+\nu)\beta_{\rho m}^2 J_m(\beta_{\rho m} r_a)} \sum_{i=1}^{N_g} e^{j2\pi m(i-1)/N_g} \\ B_m^I &= \frac{[B_g Y_\nu(kr_a) - A_g J_\nu(kr_a)]\sin[(m+\nu)\pi w/\Delta z]\left[\tan\psi\beta_{\rho m}^2 + m\beta_m/ra\right]\cos\psi}{\pi(m+\nu)\omega\mu_0\beta_{\rho m}^3 J_m'(\beta_{\rho m} r_a)} \times \\ &\sum_{i=1}^{N_g} e^{j2\pi m(i-1)/N_g}, \end{aligned} \tag{3.24}$$

where

$$\beta_{\rho m}^2 = k^2 - \beta_m^2. \tag{3.25}$$

As in [16], we also enforce the condition that the average magnetic field across the groove region is continuous

$$\int_{\text{groove i interface}} \left(H_\phi^I \cos\psi + H_z^I \sin\psi\right) dz = \int_{\text{groove i interface}} H_\theta^{G_i} dz. \tag{3.26}$$

Combined with the boundary condition for a vanishing electric field at the outside of the groove

$$E_\xi^{G_1}|_{r=r_b} = [B^g Y_\nu(kr_b) - A^g J_\nu(kr_b)]\, e^{-j\nu\theta} = 0, \tag{3.27}$$

the following condition is obtained:

$$\begin{aligned} \sum_{n=-\infty,\text{n multiple of } N_g}^{\infty} & \frac{w}{\Delta z}\left[\frac{\sin\left(\beta_n \frac{w}{2}\right)}{\beta_n \frac{w}{2}}\right]^2 \left[\frac{k\cos^2\psi}{\beta_{\rho n}}\right] \\ & \left[\frac{J_n'(\beta_{\rho n} r_a)}{J_n(\beta_{\rho n} r_a)} - \frac{1}{(k\beta_{\rho n})^2}\frac{J_n(\beta_{\rho n} r_a)}{J_n'(\beta_{\rho n} r_a)}\left(\beta_{\rho n}^2 \tan\psi + \frac{n\beta_n}{r_a}\right)^2\right] \\ & = \frac{1}{N_g}\frac{Y_\nu'(kr_a)J_\nu(kr_b) - J_\nu'(kr_a)Y_\nu(kr_b)}{Y_\nu(kr_a)J_\nu(kr_b) - J_\nu(kr_a)Y_\nu(kr_b)}. \end{aligned} \tag{3.28}$$

In this derivation, we have here assumed that the pitch angle $\psi \ll 1$. Equation 3.28 can be used to calculate the dispersion relationship for the N_g order helical groove waveguide structure. The results for a double helical groove waveguide (whose cross section is identical to a disk-loaded waveguide) are shown in Figure 3.6. For this test case, $\psi = 0.196, r_a = 8mm, r_b = 15mm$, and $d = 2.5mm$. The predicted dispersion curve is shown along side a CST numerical electromagnetic simulation of the same structure. For this case, the values from theory are close to those predicted by CST simulation (less than 1% frequency difference). A detailed study of the agreement between

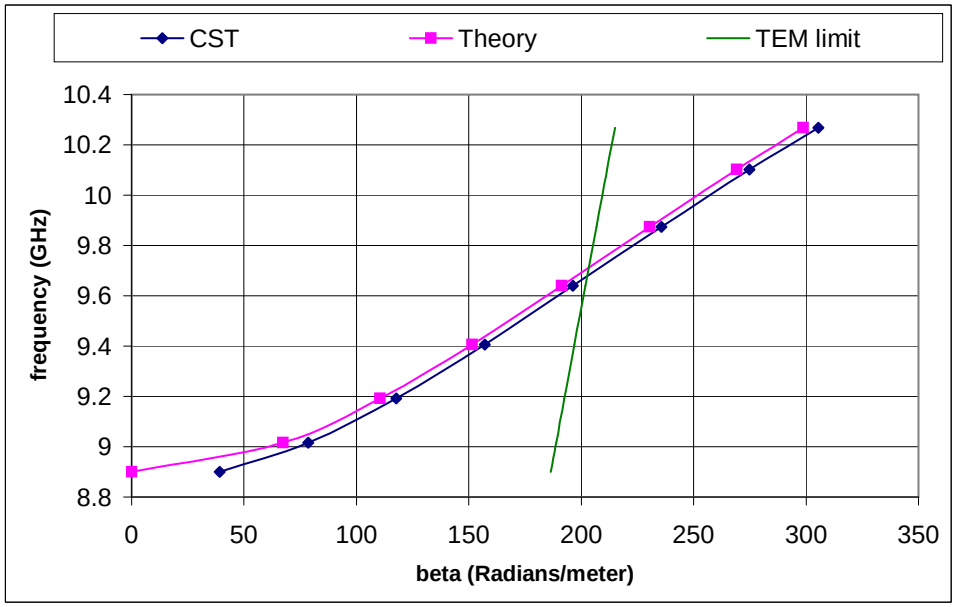

Figure 3.6: Dispersion curves for double helical groove waveguide.

CST simulation, field matching theory, and the developed numerical code will be given in Chapter 4.

However, this theoretical model based on field matching also has limitations. First, the groove(s) has to be narrow enough to assume a single TE mode in the groove region. This may not be the case in the disk-loaded structure, where the groove region is very wide compared to the disk region. Also, just as the perturbation theory is expected to break down for high values of p, the helical groove waveguide theory is expected to break down for *low* values of p, since one of the underlying assumptions made in the theory is that the pitch angle is small [16]. Therefore, although a great deal of physical insight may be gained by these analytic methods, there is also a need for more generic numerical methods that can be used to solve a wider class of problems.

In the coming sections, we will detail the development of two and three dimensional codes in the time and frequency domain. It will be shown that 3D codes are best for cavity problems when end effects need to be taken into account, while 2D codes are better for solving infinite twisted structures. The time domain solvers can be used to solve many modes at the same time, given some arbitrary initial condition. An FFT can be performed on the time domain results to determine the frequency of a mode of interest. Then, that frequency can be used as an initial guess in the frequency domain method. The frequency domain solvers can be used to directly calculate the eigenmodes of the twisted structures.

3.3 3D numerical methods

First, we examine 3D methods for solving a twisted geometry. Commercial software packages could be used to analyze twisted structures, but these often have difficulty meshing more rapidly twisted structures and converge sporadically. Also, it is anticipated that code specifically designed for a twisted geometry will be suited to solve those structures more efficiently than a more general solver.

This research focused mainly on the Non-orthogonal Finite Difference Time Domain method, or NFDTD, first proposed by Holland in 1993 [23] and later extended to a variety of problems in electromagnetics [24]. This method has the advantages of being able to simultaneously solve for a range of frequencies, being extendable to arbitrary orders, having a completely explicit updating scheme, and having a very simple form similar to the classical FDTD method.

Since the nonorthogonal curl operator can be reduced to the normal Cartesian curl operator followed by a simple matrix multiplication, finite differences can be used to compute the necessary spatial derivatives. However, a normal Yee grid cannot be used for this computation. This is because in a staggered Yee mesh, only one component of the curl is needed at each point in the grid. The field points necessary to compute that component of the curl are conveniently located adjacent to the point at which the curl is needed. In the present formulation, however, all three components of the curl are needed at every point in the updating scheme. As a result, other grids should be used such as the uniform grid, whose properties are investigated in [25]. An unstaggered

collocated grid has already been utilized in a 2D implementation of the NFDTD algorithm with good success [26]. It is proposed to use this unstaggered collocated grid in conjunction with the NFDTD method in the present research.

The finite differences could also be extended to obtain fourth order accuracy in space (rather than the second order accuracy normally obtained by the classical FDTD scheme). A 3D fourth order scheme has already been developed by the author and his collaborators, and has shown very promising results [27].

3.3.1 Boundary Treatment

A significant problem with the NFDTD method is the potential for a late-time instability if the analysis needs to be carried out for a long time [28]. A typical late-time instability is shown in Figure 3.7. It was shown by Hao and Railton that the late-time instability could be reduced by using a normal Cartesian grid except around the boundary, where the distorted mesh is retained [29]. However, the late-time instability was still not completely eliminated by this approach.

Schuhmann and Weiland showed that this problem was due to the asymmetric evaluation of the metric tensor matrix [30]. His solution was to retain the spatial interpolation, but change the way the metric tensor was evaluated.

Around the same time, Thoma and Weiland offered a proof for the stability of the spatial discretization method for a domain loaded with anisotropic material [31]. Assume that the field vectors have been vectorized, and the curl operators have been appropriately discretized, leading to the well-known Maxwell Grid Equations (MGE's) used in the finite-integration technique [32]:

$$\begin{aligned} C\boldsymbol{e} &= -\dot{\boldsymbol{b}} \\ C^T\boldsymbol{h} &= -\dot{\boldsymbol{d}}, \end{aligned} \tag{3.29}$$

where $\boldsymbol{d}$, $\boldsymbol{e}$, $\boldsymbol{b}$, and $\boldsymbol{h}$ are the discrete vectorized representations of the fields. (The fact that the curl operator acting on the electric field is the transpose of the curl operator acting on the magnetic field is essential to the demonstration of stability.) The corresponding discrete material relations are

$$\begin{aligned} \boldsymbol{d} &= D_\epsilon \boldsymbol{e} \\ \boldsymbol{b} &= D_\mu \boldsymbol{h}, \end{aligned} \tag{3.30}$$

where D_ϵ and D_μ are matrix operators corresponding to the discretized permittivity and permeability of the material, respectively. In [31], Thoma and Weiland showed that the spatial discretization scheme is stable if the curl operators were related by a transpose as in Equation 3.29, and the material operators were symmetric. The late-time stability of the scheme was demonstrated theoretically by proving non-increasing total field energy.

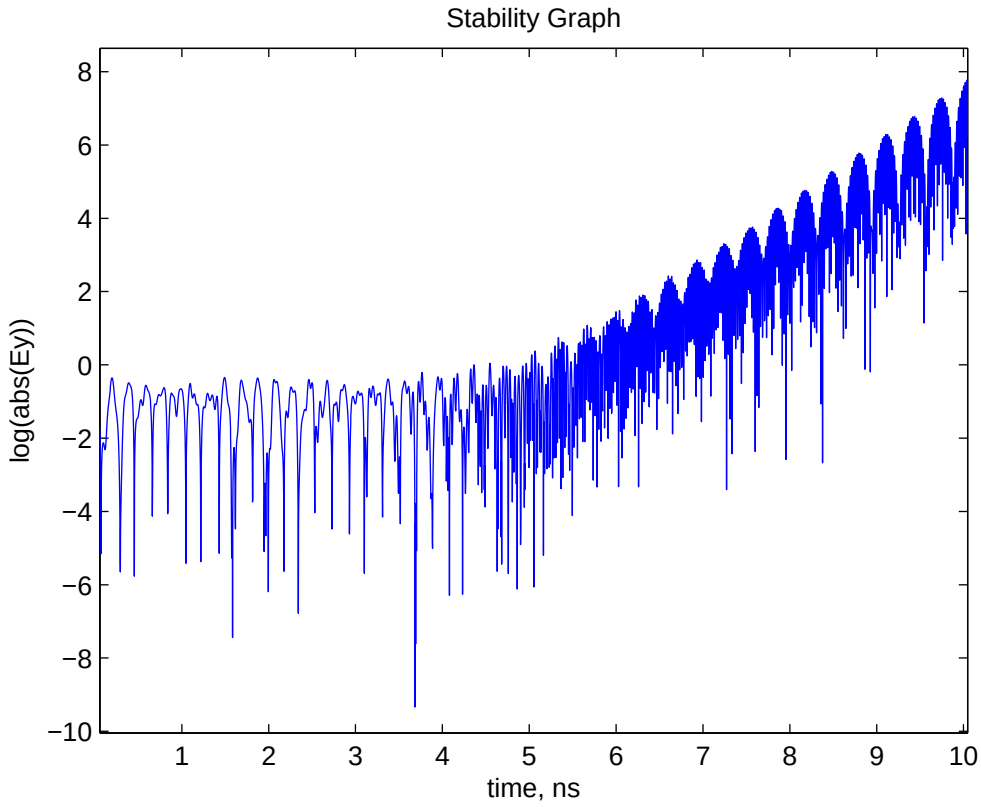

Figure 3.7: log plot of magnitude of E_y at sample point using NFDTD simulation showing late-time instability.

An alternative to this approach is to use the nonuniform, unstaggered mesh developed by Liu and Janaswamy [25, 26]. Forward differences are employed for the electric field, while backward differences are employed for the magnetic field. For a classic second order scheme,

$$\begin{aligned} \frac{dE_i}{dx_j} &= \frac{E_i(x_j + h) - E_i(x_j)}{h} \\ \frac{dH_i}{dx_j} &= \frac{H_i(x_j) - H_i(x_j - h)}{h}. \end{aligned} \tag{3.31}$$

Liu [25] demonstrated that the dissipative errors from the forward and backward difference operators cancel each other out in such a way that the resulting wave operator is accurate to second order and has no dissipative error. It is easily demonstrated that for this mesh structure, the material operators are symmetric if the metric tensor is symmetric at every point, which is guaranteed from the definition of the metric tensor. However, a challenge presents itself around a perfectly conducting boundary, since enforcing the transpose condition on the curl operators is nontrivial. This condition requires, for example, that if the computation of $(\nabla \times \boldsymbol{E})_x (i, j, k)$ involves a term $mE_y(i, j, k + 1)$ for some constant m, then the computation of $(\nabla \times \boldsymbol{H})_y (i, j, k + 1)$ must have a term $mH_x(i, j, k)$. For interior points, where Equation 3.31 applies, this condition is satisfied automatically. Near a perfectly conducting boundary, the computation of $\nabla \times \boldsymbol{H}$ is typically altered to enforce the boundary condition on the electric field. If a perfectly conducting boundary exists at $i = N_x$,

$$\begin{aligned} &(\nabla \times \boldsymbol{E})_y (N_x - 1, j, k) \\ &= \frac{E_x(N_x - 1, j, k + 1) - E_x(N_x - 1, j, k)}{\Delta z} \\ &- \frac{0 - E_z(N_x - 1, j, k)}{\Delta x}, \\ &(\nabla \times \boldsymbol{H})_z (N_x, j, k) \\ &= \frac{H_y(N_x, j, k + 1) - H_y(N_x - 1, j, k)}{\Delta x} \\ &- \frac{H_x(N_x, j, k) - H_x(N_x, j - 1, k)}{\Delta y}. \end{aligned} \tag{3.32}$$

Since $(\nabla \times \boldsymbol{H})_z (N_x, j, k)$ involves a term $-\frac{H_y(N_x-1,j,k)}{\Delta x}$ but $(\nabla \times \boldsymbol{E})_y (N_x - 1, j, k)$ does not have a $-\frac{E_z(N_x,j,k)}{\Delta x}$ term, the transpose condition is not satisfied, and there is no guarantee of stability around the boundary. Clearly, another method for enforcing the boundary conditions must be implemented. To do this, a careful examination of the boundary condition is necessary around a conducting boundary, namely

$$(\nabla \times \boldsymbol{H})_x = \frac{dD_x}{dt} = \epsilon^{1j} \frac{dE_j}{dt} = \epsilon^{11} \frac{dE_x}{dt}, \tag{3.33}$$

for an $x = constant$ boundary, leading to the updating formula

$$\frac{dE_x}{dt} = \frac{1}{\epsilon^{11}}(\nabla \times \boldsymbol{H})_x = \frac{1}{\epsilon_0\sqrt{g}g^{11}}(\nabla \times \boldsymbol{H})_x. \tag{3.34}$$

The contravariant metric tensor component g^{11} can be obtained by calculating the $(1,1)$ component of $[g_{ij}]^{-1}$. Writing in terms of the covariant metric tensor,

$$\begin{aligned}\frac{dE_x}{dt} &= \frac{1}{\epsilon_0\sqrt{g}} \\ &\times \left(g_{11} + \frac{g_{12}g_{21}g_{33} + g_{13}g_{22}g_{31} - g_{12}g_{31}g_{23} - g_{13}g_{21}g_{23}}{g_{23}g_{32} - g_{22}g_{33}}\right) \\ &\times (\nabla \times \boldsymbol{H})_x.\end{aligned} \tag{3.35}$$

Making use of the symmetry of the metric tensor,

$$\begin{aligned}\frac{dE_x}{dt} &= \frac{1}{\epsilon_0\sqrt{g}} \\ &\times \left(g_{11} + \frac{g_{21}^2 g_{33} + g_{31}^2 g_{22} - 2g_{21}g_{31}g_{23}}{g_{32}^2 - g_{22}g_{33}}\right)(\nabla \times \boldsymbol{H})_x.\end{aligned} \tag{3.36}$$

Using this relation, the material parameters can be modified along the boundary:

$$[\epsilon]^{-1} = \begin{bmatrix} \frac{1}{\epsilon_0\sqrt{g}}\left(g_{11} + \frac{g_{21}^2 g_{33} + g_{31}^2 g_{22} - 2g_{21}g_{31}g_{23}}{g_{32}^2 - g_{22}g_{33}}\right) & 0 & 0 \\ 0 & 0 & 0 \\ 0 & 0 & 0 \end{bmatrix}. \tag{3.37}$$

In practice, a very small number is used for the zero elements of this matrix in order to ensure that the material operator D_ϵ^{-1} remains invertible. Now, since the boundary condition around the boundary is satisfied implicitly, the expression for the curl of $\boldsymbol{E}$ around the boundary can be

$$\begin{aligned}&(\nabla \times \boldsymbol{E})_y (N_x - 1, j, k) \\ &= \frac{E_x(N_x - 1, j, k+1) - E_x(N_x - 1, j, k)}{\Delta z} \\ &- \frac{E_z(N_x, j, k) - E_z(N_x - 1, j, k)}{\Delta x},\end{aligned} \tag{3.38}$$

satisfying the transpose condition and ensuring stability. This modification of the material parameters around a conducting boundary in an unstaggered collocated nonorthogonal FDTD scheme to ensure stability is novel to this approach, and has not been done by others.

3.3.2 Time Stepping and Stability

The time stepping algorithm commonly used for the FDTD algorithm is the leap frog method, which is second order accurate in time. Although there is no rigorous mathematical proof of stability available for a twisted coordinate system, it has been shown in [28] that for a skew nonorthogonal coordinate system,

$$\Delta t \leq \frac{1}{c\sqrt{\frac{g^{ij}}{\Delta x^i \Delta x^j}}}. \tag{3.39}$$

This relation does not hold when the coordinate lines are curved, but it can provide a reasonable estimate in regions where the lines are not severely curved.

It has been demonstrated by the author and his collaborators [27] that the CFL stability condition on the time step can be weakened by a factor of $2\sqrt{2}$ by implementing the fourth order, four stage Jameson method time integrator. The stability domain is shown in Figure 3.8. As long as the eigenvalues of the discrete curl operator remain within the region enclosed in the complex domain, stability will be ensured. Used in conjunction with the fourth order spatial derivatives discussed earlier, the Jameson method time integrator can provide fourth order accuracy.

3.4 2D numerical methods

For physically long twisted structures where end effects can be neglected, a 2D method should be used to solve twisted structures. For this, we introduce two complementary simulation techniques, the 2D NFDTD method, or non-orthogonal finite difference time domain method, and the 2D NFDFD method, or non-orthogonal finite difference frequency domain method.

3.4.1 2D NFDTD Method

Simulating periodic structures in the time domain presents a challenge, because the phase shift boundary conditions on the ends of the propagating structure are in the frequency domain. Ordinarily, to translate the phase shift condition into the time domain, data points are needed for many previous time steps around the boundary, adding complexity to the algorithm. More recently, a scheme has been developed by Harms, Mittra, and Ko [33, 34] to implement a periodic boundary condition using a combination of sin and cos excitations, which eliminates the need for storage of many previous time steps. This method comes at a cost of having to essentially run two separate but coupled FDTD algorithms side by side, one for the sin response, and the other for the cos response.

However, for the twisted guide, the algorithm can be simplified much further, since the period can essentially be reduced to zero if the appropriate coordinate system is chosen, giving a 2D mesh. A 2D FDTD algorithm was proposed by Xiao, Vahldieck, and Jin for the efficient solution of straight

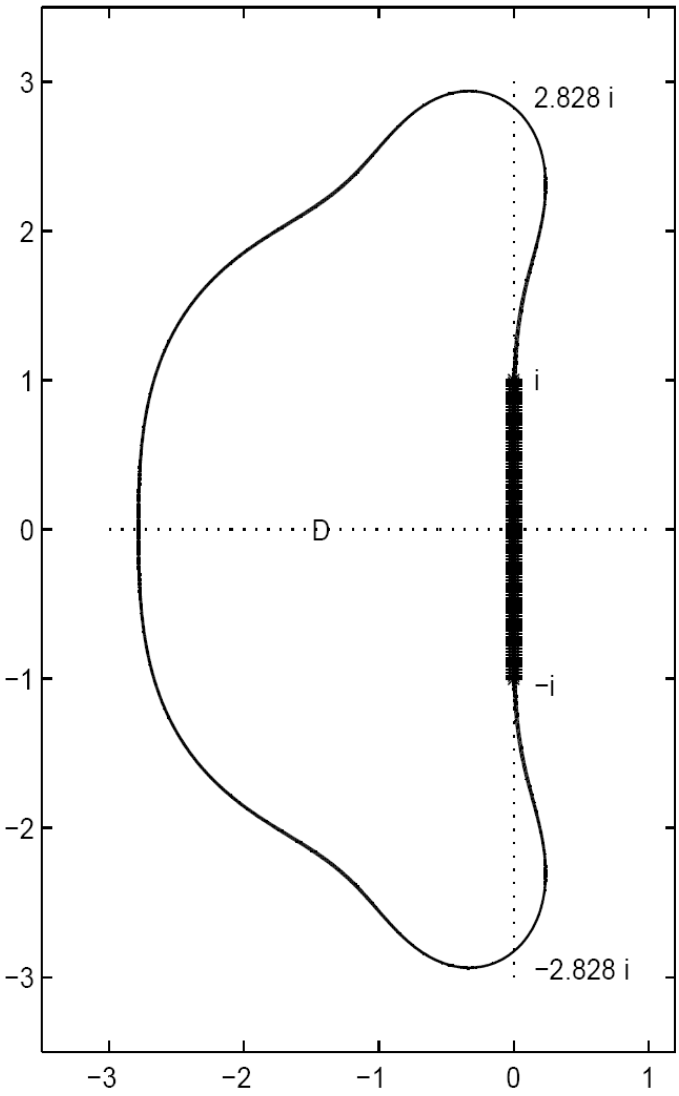

Figure 3.8: Stability domain for Jameson method time integrator

waveguide propagation problems [35], [36]. This should not be confused with a conventional 2D FDTD method where the fields are assumed to be uniform in one direction. Here, the idea is to assume a solution of the form

$$\begin{aligned} \boldsymbol{E}(x,y,z,t) &= \Re\Big\{\boldsymbol{E_1}(x,y,t)e^{-j\beta z}\Big\} \\ \boldsymbol{H}(x,y,z,t) &= \Re\Big\{\boldsymbol{H_1}(x,y,t)e^{-j\beta z}\Big\}. \end{aligned} \tag{3.40}$$

$\Re\{\}$ represents the real part. The value of β is a running variable from 0 to ∞. Each value of β will result in a number of modes with different frequencies. This technique allows dispersion curves to be obtained efficiently for a large number of modes. We do this by running a number of simulations while sweeping the value of β. Then, instead of the z derivatives being calculated in the conventional sense using finite differences, they are calculated using an exact formula by multiplying that field component by $-j\beta$. Although this means that the computations will now involve complex quantities rather than the purely real computations of the classical FDTD method, the mesh can now be reduced from three dimensions to two.

It was shown in [36] that the disadvantages of complex computations could be eliminated by adding a factor of j in the representation of E_z, H_x, and H_y, making all field quantities real even for anisotropic permittivities. The original fields in three dimensions can be recovered by substituting the computed solutions in for $\mathbf{E_1}$ and $\mathbf{H_1}$ in Equation 3.41 and solving for $\mathbf{E}$ and $\mathbf{H}$. Although not explicitly stated in [36], the real nature of the time domain fields is only preserved if the permittivity tensor elements $\epsilon_{13} = \epsilon_{23} = \epsilon_{31} = \epsilon_{32} = 0$, so for the twisted case, complex arithmetic must still be used.

It must be pointed out that we cannot solve twisted waveguide problems directly in Cartesian coordinates using this method, since the fields do not strictly satisfy Equation 3.41. However, if a helical coordinate system is introduced, the fields could indeed have this form and a 2D method could be employed. The anisotropic equivalent problem discussed in Section 3.1 provides another way of thinking about this: it allows the twisted structure to be solved as a straight structure with anisotropic and nonuniform $\bar{\mu}$ and $\bar{\epsilon}$. Of course, as soon as the structure is transformed into a long straight structure, Equation 3.41 holds, and 2D solution methods are valid. The finite difference operators along each of the nonorthogonal coordinate axes can be defined using the coefficients derived by Liu for an orthogonal coordinate system [25]. For the second order case, this mesh reduces to a "collapsed" version of the Yee grid, discussed by Xiao and Vahldieckin [36]. This mesh is shown in Figure 3.9.

3.4.2 2D NFDFD Method

The Finite Difference Frequency Domain method was investigated in detail by Lui and Chen [37]. In it, the fields are assumed to be harmonic in time and in the z direction, so the explicit time

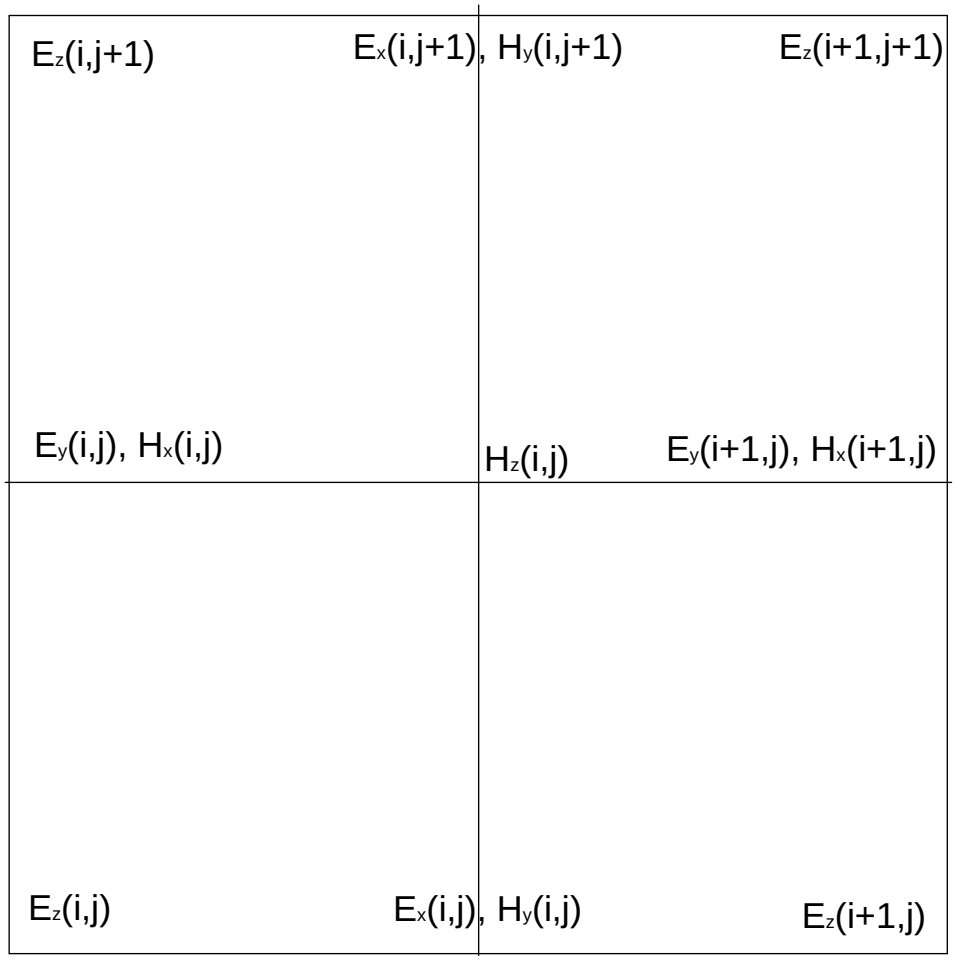

Figure 3.9: "Collapsed" Yee grid used in the second order 2DNFDTD method.

updating scheme of the FDTD method is eliminated completely and replaced by an eigenvalue problem. In it, all six field components are solved for directly. Later, it was found that the number of actual solved field components and the number of nonzero matrix elements could be reduced significantly [38], [39]. The solution of curved waveguides using 2D FDFD has previously been attempted by Lavranos and Kyriacou [40]. However, their formulation depended on an orthogonal coordinate system and the ability to separate the field into axial and transverse components, which was mentioned in [40] to be invalid for high curvature rates (or small curvature radii).

By contrast, this research proposes to solve the twisted structure in nonorthogonal coordinates which is based on an exact equivalent, and does not make any simplifying assumptions that would be invalid for high twist rates. To use this method to solve the Maxwell equations for a twisted waveguide structure, the vector Helmholtz equation in general curvilinear coordinates is derived. Using the anisotropic equivalent structure defined by Equation 3.7 and solving in Cartesian coordinates, the Maxwell curl equations become

$$\frac{1}{\sqrt{g}}[g_{ij}]\nabla \times \bar{\mathbf{E}} = -j\omega\mu_0\bar{\mathbf{H}} \tag{3.41}$$

$$\frac{1}{\sqrt{g}}[g_{ij}]\nabla \times \bar{\mathbf{H}} = -\omega\epsilon_0\bar{\mathbf{E}}, \tag{3.42}$$

from which we can also write from Equation 3.42,

$$\nabla \times \bar{\mathbf{H}} = \sqrt{g}j\omega\epsilon_0[g^{ij}]\bar{\mathbf{E}}. \tag{3.43}$$

Taking the curl of Equation 3.41,

$$\begin{aligned} \nabla \times \left(\frac{1}{\sqrt{g}}[g_{ij}]\nabla \times \bar{\mathbf{E}}\right) &= \nabla \times \left(-j\omega\mu_0\bar{\mathbf{H}}\right) \\ &= -j\omega\mu_0\nabla \times \bar{\mathbf{H}} \\ &= -j\omega\mu_0\sqrt{g}j\omega\epsilon_0[g^{ij}]\bar{\mathbf{E}} \\ &= \omega^2\mu_0\epsilon_0\sqrt{g}[g^{ij}]\bar{\mathbf{E}} \\ &= k_0^2\sqrt{g}[g^{ij}]\bar{\mathbf{E}} \end{aligned} \tag{3.44}$$

which leads to the eigensystem

$$\frac{1}{g}[g_{ij}]\nabla \times \left([g_{ij}]\nabla \times \bar{\mathbf{E}}\right) = k_0^2\bar{\mathbf{E}}. \tag{3.45}$$

In this scheme, three vector components have to be computed at each grid point. For example, if a 20 by 20 grid was employed to solve a twisted square waveguide, the dimension of the system would be $20 \times 20 \times 3 = 1200$, and the total number of matrix elements would be $1200^2 = 1.44 \times 10^6$. Fortunately, the use of finite differences assures us that the matrix will likely be sparse. If the

sparsity of the matrix is taken into account, it can drastically reduce memory and calculation time.

3.5 Extension to Arbitrary Cross Sections

Thus far, we have only considered twisted waveguides of rectangular cross sections. Fortunately, our choice of a twisted coordinate system allows a simple cascaded coordinate transform that permits a solution to arbitrary twisted guides. The coordinate transform of Equation 2.2 is combined with a planar transform

$$\begin{aligned} x' &= x'(u,v) \\ y' &= y'(u,v) \\ z' &= w, \end{aligned} \tag{3.46}$$

giving

$$\begin{aligned} x &= x'(u,v)\cos pw - y'(u,v)\sin pw \\ y &= y'(u,v)\cos pw + x'(u,v)\sin pw \\ z &= w \end{aligned} \tag{3.47}$$

for the overall transformation. This cascaded transform is illustrated in Figure 3.10. The functions u and v can be derived using finite differences from any commercial or freeware software package capable of generating 2D structured planar meshes. We have made use of a free utility called UNAMALLA [41] to generate such meshes. The covariant metric tensor for this cascaded transform can be obtained using the well-known rule

$$(g_{ij})_u = (g_{mn})_{x'} \frac{\partial x'^m}{\partial u^i} \frac{\partial x'^n}{\partial u^j}. \tag{3.48}$$

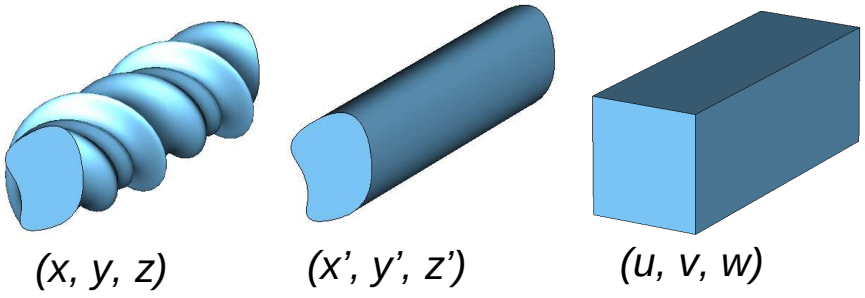

Figure 3.10: Cascaded coordinate transformation used to analyze arbitrary twisted structures.

Here, $(g_{mn})_{x'}$ is the metric tensor for the transform from cartesian coordinates to the primed coordinates (in this case, Equation 2.2). For such arbitrary cross sections,

$$[g_{ij}] = \tag{3.49}$$
$$\begin{bmatrix} x'^2_u + y'^2_u & x'_u x'_v + y'_u y'_v & px'y'_u - py'x'_u \\ x'_u x'_v + y'_u y'_v & x'^2_v + y'^2_v & px'y'_v - py'x'_v \\ px'y'_u - py'x'_u & px'y'_v - py'x'_v & 1 + p^2(x'^2 + y'^2) \end{bmatrix}.$$

Since the mesh generation program outputs the coordinates of each point on the grid, u and v at each mesh point are known. The derivatives x'_u, x'_v, y'_u, and y'_v are calculated using finite differences. Such a simple form of the metric tensor is a consequence of the particular helical coordinate system chosen. Also, note again that the longitudinal coordinate does not appear in the metric tensor, allowing two dimensional methods to be used. From here, the relations of Equation 3.7 can be used to calculate the material properties of the transformed guide.

Such a planar transformation is demonstrated for the twisted "keyhole" structure. The cross section, along with the generated UNAMALLA mesh, is shown in Figure 3.11.

3.6 Summary

A number of numerical methods have been presented that are capable of solving both slowly and rapidly twisted structures. 3D codes give good results for closed (cavity) problems where end effects are significant, while 2D codes are much faster and can give good results for infinite structures or for closed structures that are long enough that end effects are not as significant. Both the 2D and 3D codes can be used in either the time or frequency domain. The time domain code allows one to select an initial condition guess that is close to the desired eigenmode and to solve for many modes simultaneously. An FFT can then be performed to extract frequency domain data, which in turn can serve as an initial guess for the frequency domain solver. The frequency domain solver is the appropriate choice when solving for specific eigenmodes of the twisted structure.

When used in conjunction, the time and frequency domain numerical methods based on a straight equivalent waveguide can be used to solve twisted guides of any arbitrary cross section. Therefore, these numerical techniques are more generally applicable than other methods of solving twisted guides (like the perturbation theory and mode matching approaches), which are applicable only for limited cross sectional shapes. They are also more efficient then existing commercial codes for solving twisted guides because they are specifically designed to handle the challenges associated with rapidly twisted geometries.

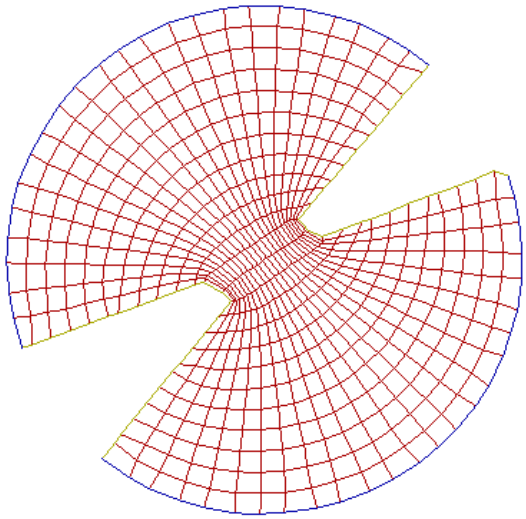

Figure 3.11: Keyhole cross section and corresponding mesh.

Chapter 4

Result Validation

Accurate electromagnetic simulation results are important in designing accelerating cavities. Typically, resonant frequencies should be within a couple percent of their predicted values from simulation. In practice, accelerating cavities must be fine tuned either through mechanical deformation or active devices such as ferrite tuners. This is because of mechanical errors introduced by manufacturing tolerances. To further complicate matters, Lorentz forces due to the high accelerating fields within the cavity cause periodic deformations of the cavity shape. Such forces make it impossible to exactly tune the cavities without active tuning elements. Nevertheless, electromagnetic simulation should provide a very good initial guess for the cavity frequency.

Since exact closed-form expressions for the electromagnetic fields in a twisted cavity or waveguide do not exist, computing the error of any given method is not a trivial problem. Therefore, we will use several separate methods to validate results. Although there is some degree of error present in each individual validation method, taken together these methods give substantial credence to the validity of the model in question.

First, we validate the code by comparing it to other well-known software packages such as CST Microwave Studio [42] for cases when we anticipate the commercial code will perform well. Then, we validate the code by comparing the results to analytic expressions that are valid for very specific twisted geometries. Finally, we perform experimental investigation.

4.1 Existing Electromagnetics Software

In this section, we compare our code to CST Microwave studio for the case of a twisted rectangular guide of moderate twist rate. For such rates, perturbation theory will fail, and it would be quite difficult to derive any analytic expression. To test the numerical method for such a case, a moderate twist rate is chosen such that the CST software is still anticipated to be accurate. We choose dimensions of 8.16 cm by 3.63 cm. Since CST and other commercial software cannot support a continuously varying twist rate, a fixed twist rate of 30 $\frac{R}{m}$ was selected. At this twist rate, there

is already significant difference between the developed 2D code and the results of the perturbation theory.

Figure 4.1 shows that for this moderate twist rate, the results of CST and the results provided by the 2D FDFD code align nearly perfectly. This particular simulation was carried out using a 50 X 50 mesh with our developed code. The fact that agreement is so good lends credibility to the proposed numerical model and its effectiveness at solving twisted guides with slow to moderate twist rates.

4.2 Special Cases

For the first special case, we discuss validating our numerical methods through a comparison with the results of Lewin and of Yabe and Mushiake. Since these methods are based on perturbation theory, with the twist rate as the perturbation parameter, we expect to see good agreement between [10] and [12] and the present theory at slow twist rates.

To test the time-domain code, a five inch section of uniformly twisted X-band waveguide was simulated. The twist rate was 49.47 $\frac{R}{m}$. This corresponds to one complete twist over the five inch length. An initial condition was chosen to excite the dominant mode of interest. The accuracy was checked by performing an FFT on the electric field at a sample point and comparing to the resonant frequencies predicted by the perturbation theory results developed by Yabe and Mushiake [12]. Only the first three TE-like modes were tested. Since the twist rate is fairly low, the perturbation theory results are expected to be relatively accurate. The comparison results are shown in Table 4.1, and the time domain fields and the spectrum are shown in Figure 4.2.

The simulation was carried out to a final time of 6×10^{-8} sec, and an 18 by 8 by 100 mesh was used. No late-time instability was observed during the simulation. A raised cosine window function was used for the FFT. The frequency of the resonances was determined by locating each of the peaks of the spectrum.

The perturbation theory predictions are only valid for the dominant TE_{10}-like mode of the twisted waveguide, so the complete spectrum of the twisted cavity cannot be obtained by the theory in [11, 12]. However, the resonant frequencies corresponding to TE_{10n} modes of the cavity can be obtained by setting

$$\beta_z = \frac{n\pi}{L}, \tag{4.1}$$

where L is the cavity length. The ω versus β relationship predicted by perturbation theory can then be used to calculate the resonant frequencies. Note that although the metal walls on either end of the cavity will introduce some end effects not accounted for in the theory, the results of Table 4.1 demonstrate that this effect does not significantly alter the result (at least for this value of twist rate).

Another trial was devised in which an arbitrary rectangular waveguide is twisted at different

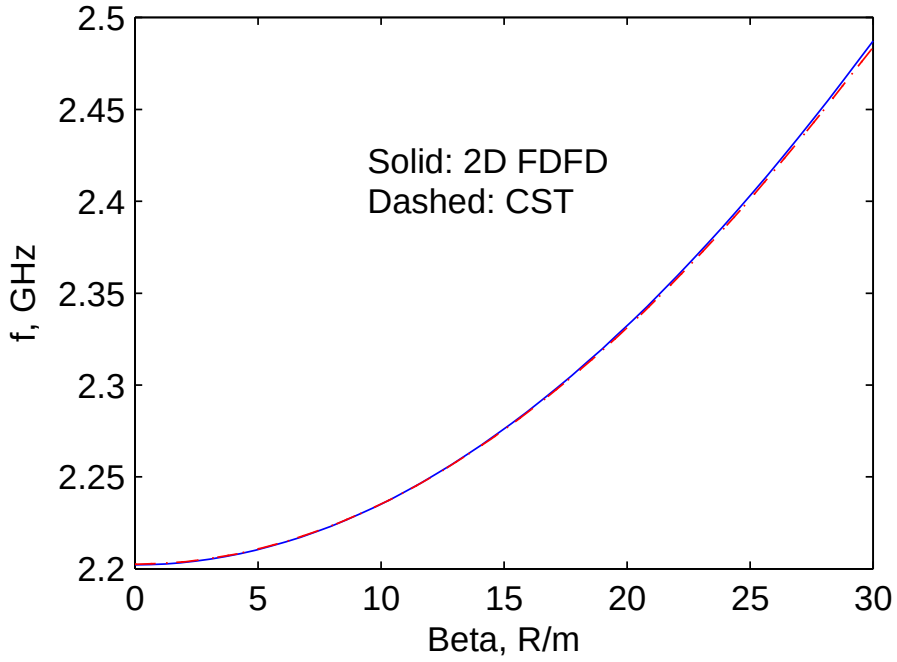

Figure 4.1: Dispersion relationship for 8.16 cm by 3.63 cm rectangular waveguide with twist rate of 30 $\frac{R}{m}$.

Table 4.1: Results for 3D NFDTD simulation of twisted waveguide

	Mode 1	**Mode 2**	**Mode 3**
Perturbation Theory	6.9684 GHz	7.2348 GHz	7.6580 GHz
3D NFDTD code	6.9849 GHz	7.2526 GHz	7.6771 GHz
% difference	0.237%	0.246%	0.249%
Straight waveguide (known)	6.6626 GHz	6.9692 GHz	7.4522 GHz

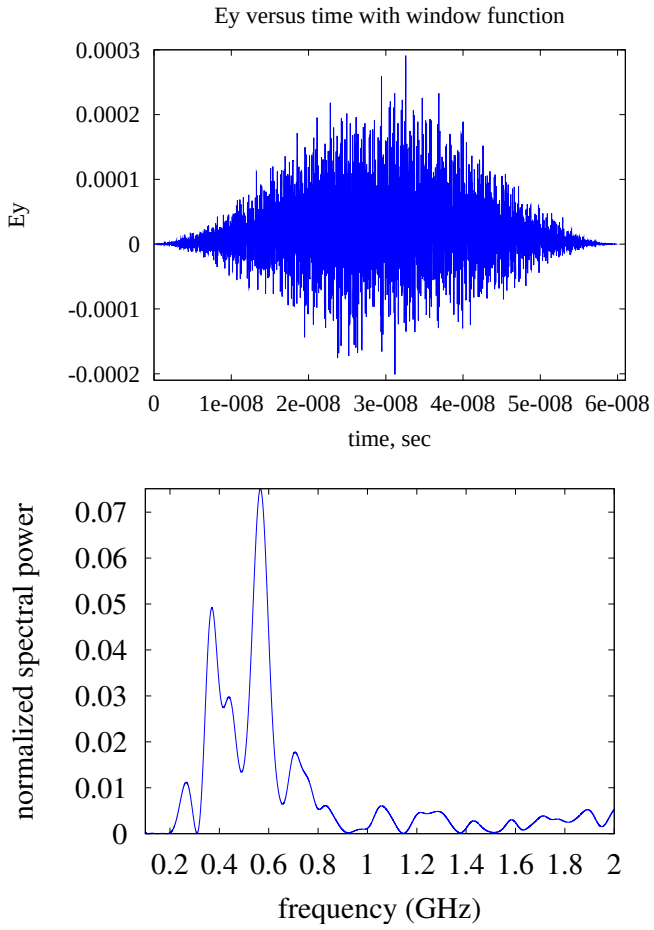

Figure 4.2: Simulated Ey multiplied by raised cosine window function, and corresponding spectrum.

rates and the cutoff frequency is calculated. The cutoff frequency is easily obtained using the 2D finite-difference time domain and 2D finite-difference frequency domain techniques discussed in Chapter 3. One must simply set the propagation constant $\beta = 0$ and solve for the frequency of the TE_{10}-like mode. The comparison for an 8.16 cm by 3.63 cm waveguide is shown in Figure 4.3.

The results of this trial show that at low twist rates, the developed numerical models yield results that are very close to those of the perturbation theory methods. However, at higher twist rates the agreement is not as good; this is expected, since the perturbation techniques were never intended to be used for rapidly twisted cases.

A second special case is that of the helical groove waveguide. The theory of this rapidly twisted structure was given in [15] and refined to any number of grooves in Section 3.2.2. For this case, we expect to see good agreement for rapid twist rates. For this case, we used a single helical groove. The inner radius was 8 mm and the outer radius was 15 mm. The angle subtended by the "notch" section in the twisted cross section was 90°. For this structure, we compared the cutoff frequency of the dominant TE_{10}-like mode predicted by the present 2D code to the predictions of helical groove theory and CST commercial software. For the commercial code, a periodic boundary condition was established over one half twist, and a 0° phase shift was implemented between the phase shift boundaries to simulate the cutoff condition. The 2D FDFD code was run with a 25 X 25 mesh, a 50 X 50 mesh, and a 75 X 75 mesh. The comparison is shown in Figure 4.4.

Here, we can see that as the mesh is refined, the results approach the helical groove theory for rapid twist rates. Also, the results of CST are very good for slow to moderate twist rates, but become inaccurate for high twist rates. For extremely rapid twist rates, CST fails altogether with a mesh generation error. It is difficult to give a definitive rule regarding how many mesh points are needed for a good simulation. In general, it will depend greatly on the judicious choice of a structured mesh. In practice, one should run several cases with varying degrees of mesh refinement to determine when convergence has been achieved.

4.3 Experimental Investigation

The final method that is used for result validation is experimental investigation. The measurement results are so important that a separate chapter (Chapter 6) is devoted to their discussion. Obviously, there are errors present in the experiment as well (mechanical tolerance, losses, probes, etc.), yet close agreement with experiment is a crucial test of the validity of any electromagnetic model.

4.4 Summary

In this chapter, we have validated the accuracy of the developed numerical techniques by comparing the results to commercial software [42] as well as two special cases where analytic expressions are available. Specifically, good agreement was obtained with the perturbation theory [10–12] for

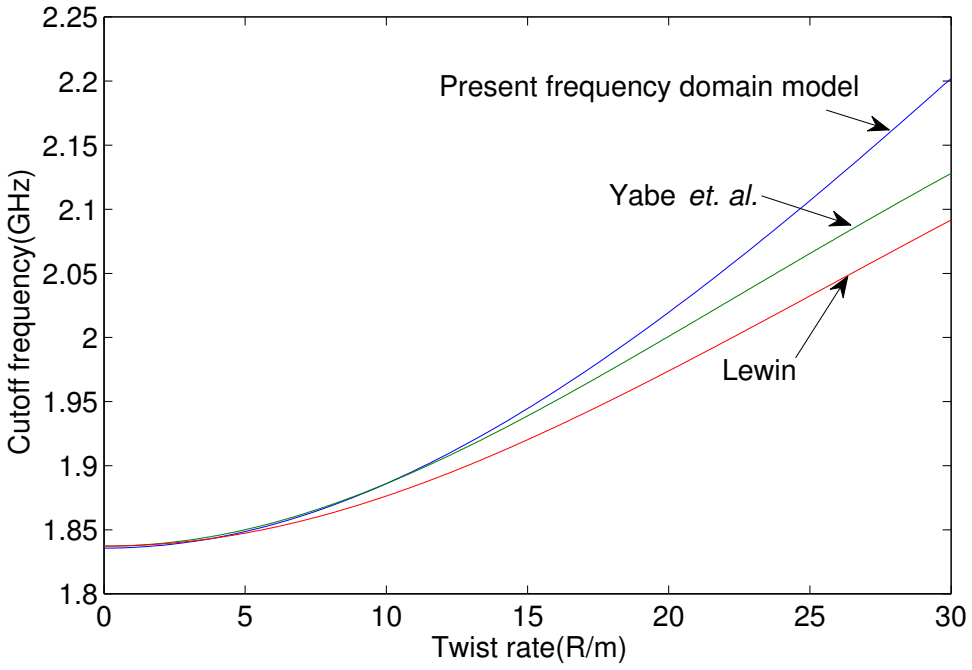

Figure 4.3: Cutoff frequencies predicted for 8.16 cm by 3.63 cm rectangular waveguide.

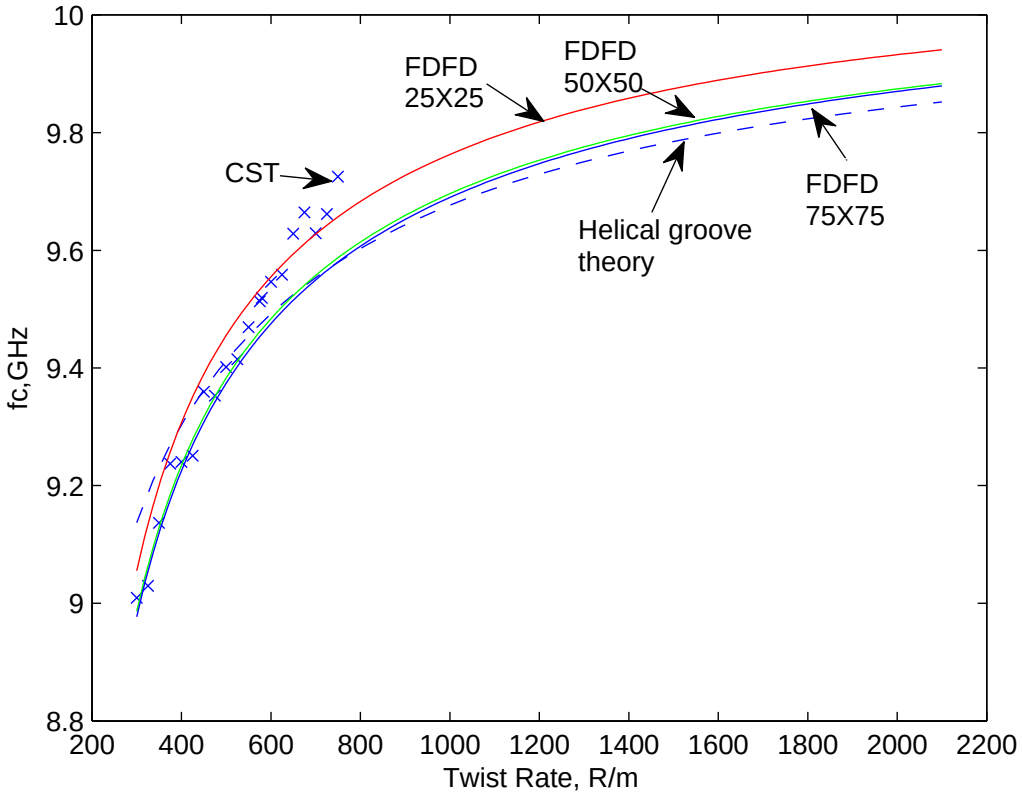

Figure 4.4: Cutoff frequencies predicted for a single helical groove waveguide with varying twist rates.

rectangular guides at low twist rates and with field matching theory [15, 16] for helical groove waveguides at high twist rates. A detailed experimental investigation is undertaken in Chapter 6.

These validation results indicate that the developed numerical models of Chapter 3 can give accurate results for arbitrary cross sections for both slowly and rapidly twisted structures. The results of the validation study also provide an idea of the limits of accuracy for the perturbation theory and field matching techniques for solving twisted guides. The validation study also showed the limitations of commercial electromagnetic codes.

Chapter 5

The Twisted Cavity as an Accelerating Structure

One of the important potential applications for twisted cavities is in the area of particle accelerators. The idea of a twisted waveguide accelerating structure was proposed by Kang in 2000 [8]. Normally, reactive loading is employed in accelerating cavities in order to slow the phase velocity of the electromagnetic wave [5] [6]. However, since these types of cavities all have a non-uniform cross section, they tend to be difficult to machine, requiring complicated welding or brazing processes which increase the total cost. It was demonstrated that the twisted waveguide, possessing a uniform (although constantly rotating) cross section, also offers the potential to support slow-wave modes. In this research, a detailed comparison is to be made between several conventional accelerating structures and their longitudinal helical analogs. This is possible because most accelerating structures are rotationally symmetric or very nearly so.

In considering accelerator applications, only TM modes are of interest. This is because only TM modes have a z component to the electric field, which is effective in producing an accelerating force on a charged particle. TE modes have been considered for producing a transverse force on the particle (useful for undulators and wigglers), but for the present we will focus on the accelerating TM modes.

Our analysis shall concentrate mainly on two types of twisted accelerating prototypes. The first is the longitudinal helical analog of the disk-loaded accelerating structure. This is essentially a disk-loaded structure whose geometry is shown in Figure 2.3. The second is analogous to the TESLA-type superconducting cavity used as a medium-beta superconducting cavity at the Spallation Neutron Source (SNS). The cross section of a TESLA type accelerating cavity is shown in Figure 5.1. The outline is constructed by connecting two sets of ellipses with tangent lines. This outline then defines the ρ vs z profile of the rotationally symmetric accelerating cavity in cylindrical coordinates.

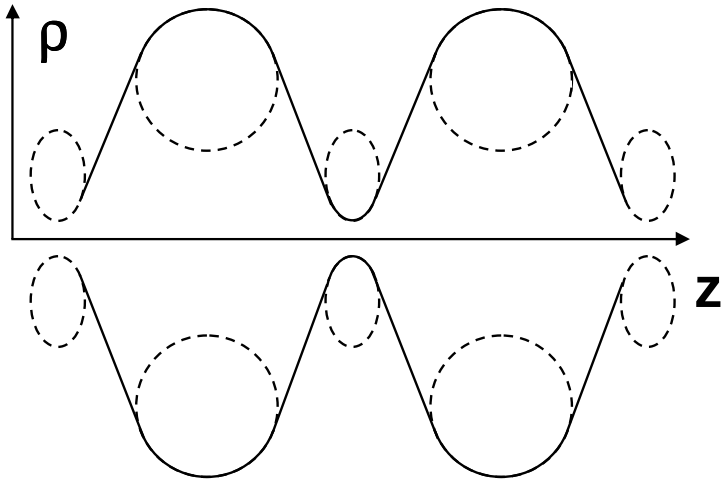

Figure 5.1: Construction of the outline for a TESLA-type accelerating cavity

5.1 Quantities of Interest for Accelerating Cavities

In comparing cavity types, it is necessary to compute several standard figures of merit commonly used in accelerating structures. The first quantity of interest is the *accelerating gradient*, which is the maximum $|E_z|$ on the z axis of the cavity. A higher accelerating gradient corresponds to more accelerating force exerted on the particle. The accelerating gradient is usually normalized to some other accelerator parameter, like total stored energy, to make it more useful.

The accelerating voltage can be computed as an integral of $|E_z|$ along the z axis of the cavity.

$$V_{acc} = \int_0^{L_{cavity}} |E_z| \; dz, \rho = 0. \tag{5.1}$$

We also define the particle beta as

$$\beta = \frac{v_{particle}}{c}. \tag{5.2}$$

If the input power to the cavity P is known and stored energy U is known, then

$$Q = \frac{\omega U}{P} \tag{5.3}$$

$$R = \frac{V_{acc}^2}{2P} \tag{5.4}$$

$$\frac{R}{Q} = \frac{V_{acc}^2}{2\omega U} \tag{5.5}$$

where $R = R_{shunt}$ is commonly called the shunt impedance, or the resistance of the equivalent

parallel RLC circuit corresponding to the accelerating cavity. Of these, the quantity $\frac{R}{Q}$ is of particular interest as a figure of merit, since it is not directly dependent on the dissipated power P. It will depend, therefore, purely on the geometry of the cavity rather than the material of the cavity. Loosely speaking, it describes how much accelerating voltage can be obtained with a given amount of energy stored in the cavity. Typically, the value of $\frac{R}{Q}$ scales linearly with the cavity length for a given cavity geometry, so it is also useful to normalize $\frac{R}{Q}$ to the length:

$$\frac{R}{Ql} = \frac{V_{acc}^2}{2\omega U l} \tag{5.6}$$

In this chapter, we will also speak of accelerating modes defined by the amount of phase shift of the fundamental space harmonic per unit cell. For example, in a π mode of operation, the electric field in each cell is offset from the neighboring two cells by a phase shift of 180° or π radians. In a twisted structure, it is also possible to define a "cell" by the amount of twisting required to map the transverse cross section back onto itself. As such, we will loosely use the same nomenclature for accelerating modes in a twisted structure as is commonly applied to nontwisted accelerating structures.

Another important parameter is the *transit time factor* T, which provides a correction to the acceleration of a particle due to the time-variation of the fields in a cavity. Note that in Equation 5.1, E_z is assumed to be the magnitude of the z component of the time-harmonic field $\bar{\mathbf{E}}$. In reality, this field will change with time as the particle physically moves down the accelerator, so a correction factor is needed. T can have any value between 0 and 1. The total kinetic energy (K.E.) gained by a particle in the cavity is

$$\Delta K.E. = qV_{acc}T, \tag{5.7}$$

where q is the charge of the particle.

5.2 Advantages of Twisted Accelerating Structures

There are a number of advantages of twisted accelerating structures over periodic reactively loaded ones. In a periodic structure, the fields can be expressed by an infinite Floquet expansion. For example,

$$\boldsymbol{E} = \sum_{n=-\infty}^{\infty} \boldsymbol{E}_n(x,y)e^{j\beta_n z} \tag{5.8}$$

where

$$\beta_n = \beta_0 + \frac{2\pi n}{\Delta z}. \tag{5.9}$$

However, in the twisted coordinate system of (2.2), we have $\boldsymbol{E}_n = 0$ for all $n \neq 0$, due to the fact that the waveguide becomes equivalent to a straight waveguide under the coordinate transformation. Thus, only a single space harmonic is present. In conventional coordinates (cylindrical or cartesian), an infinite number of space harmonics will still be needed, but along the z axis (which coincides with the z axis of the twisted coordinate system) all higher space harmonics must vanish:

$$\boldsymbol{E}_n(x = 0, y = 0) = 0, n \neq 0. \tag{5.10}$$

The implication of this is that along the axis of an infinite twisted structure there is no variation in the magnitude of the fields – only in the phase. This distinguishes the twisted guide from conventional slow-wave structures (like corrugated or iris-loaded waveguides). Since only the $\boldsymbol{E}_0$ harmonic travels synchronously with the particle beam and acts cumulatively to accelerate the particles, the elimination of other harmonics is very desirable, and it could be accomplished using the twisted structure. In terms of the transit time factor T, this implies that $T = 1$ for twisted accelerating structures for an on-axis particle.

A second advantage of twisted accelerating structures involves what are known as "trapped modes". Higher order trapped modes are troublesome in most conventional periodically loaded accelerating structures because of the appearance of stop-bands in the dispersion characteristic. When beam energy is deposited in such a stop band, the excited fields cannot propagate out of the structure to higher-order mode dampers, and they can remain "trapped" in the accelerating cavity. Such modes are particularly problematic in superconducting cavities, because the large Q values allow these unwanted resonances to continue for a long time before finally decaying due to wall losses. In the case of the twisted guide, however, there are no stop bands above the cutoff frequency of the fundamental propagating mode. In essence, these modes can be thought of to continue on to infinitely high values of β by virtue of the straight waveguide equivalent. This means that undesired modes will be able to propagate out of the structure and be damped by higher order mode (HOM) dampers.

A third observation relates to mode spacing in these accelerating structures. Many periodically loaded accelerating cavities operate very efficiently close to π mode, or 180 degrees of phase shift per unit cell. However, near the point on the dispersion curve where $\beta = \frac{\pi}{\Delta z}$, the group velocity (calculated as $\frac{d\omega}{d\beta}$) typically approaches zero. This prohibits effective operation, since nearby unwanted modes would be excited very easily. One solution to eliminate the problem of zero group velocity at π mode is the deliberate creation of confluent pass bands, with the point of confluence judiciously selected as the point of the desired π mode operation [43]. However, this requirement places a significant constraint on the design of the periodic accelerating structure. In the case of the twisted waveguide no such problem exists, as the group velocity remains nonzero for all values of the phase constant β.

5.3 Twisted Disk-Loaded Accelerating Structure

Consider the SLAC two-mile accelerating structure, which was designed to accelerate electrons. Since the electron has such a small mass to charge ratio, it can be accelerated to relativistic velocities very quickly. Thus, the SLAC cavities were designed assuming the particle bunch is traveling at the speed of light (beam beta = 1), and the phase velocity of the electromagnetic wave is matched to this speed. A longitudinal helical analog for a disk-loaded accelerating structure was defined in Section 2.2. The transverse cross section of such a structure is the keyhole shape shown in Figure 2.4. The parameters of the original SLAC disk-loaded structure are shown in Table 5.1.

Each cavity consists of a number of "cells" which are separated from one another by an iris (or disk). A CST simulation of a 3-cell variation of this disk-loaded structure reveals the accelerating mode of interest. Figure 5.2 shows the simulated electric field distribution in a longitudinal cross section. The eigenmode simulation has been normalized such that the stored energy in this 3-cell cavity is 1 Joule. An electron traveling along the z axis would be synchronized with the EM wave in such a way that E_z is always negative, producing a force in the positive z direction, adding to the kinetic energy of the particle. The phase shift for this 3-cell cavity is $\frac{2\pi}{3} \cdot 3 = 2\pi$. The three-cell cavity is a good approximation to an infinite structure, since the electric field is directed mostly along the z axis, so the presence of an electric wall at the z boundaries will not significantly perturb the fields. The CST simulated resonant frequency, 2.826 GHz, is very close to the design value of 2.856 GHz. If the phase shift for the cavity is θ, the phase velocity of the wave can be calculated as $v_{ph} = \frac{\omega}{\beta_z} = \frac{2\pi f L_{cavity}}{\theta} = 2.967 \times 10^8 \frac{m}{s} \approx c$. Also note that the accelerating mode is *not* the dominant mode, which is usually the case for an accelerating cavity. (In this case, CST predicts that the mode of interest is Mode 3.)

We now turn to the longitudinal helical analog to this structure. This analog was defined in Section 3.2.2. The twist rate parameter p is found using Equation 2.18 to be $89.76 \frac{radians}{m}$. Entering this structure into CST and simulating, we obtain the electric field shown in Figure 5.3. If Mode 8

Table 5.1: Parameters for the SLAC accelerating cavities

Parameter	**Value**	**Unit**
Frequency	2.856	GHz
Length	3.048	m
Cell radius	4.13	cm
Iris radius	1.135	cm
Cell length	3.5	cm
Phase advance per cell	$\frac{2\pi}{3}$	Radians
Disk thickness	0.584	cm
Quality factor	13,000	

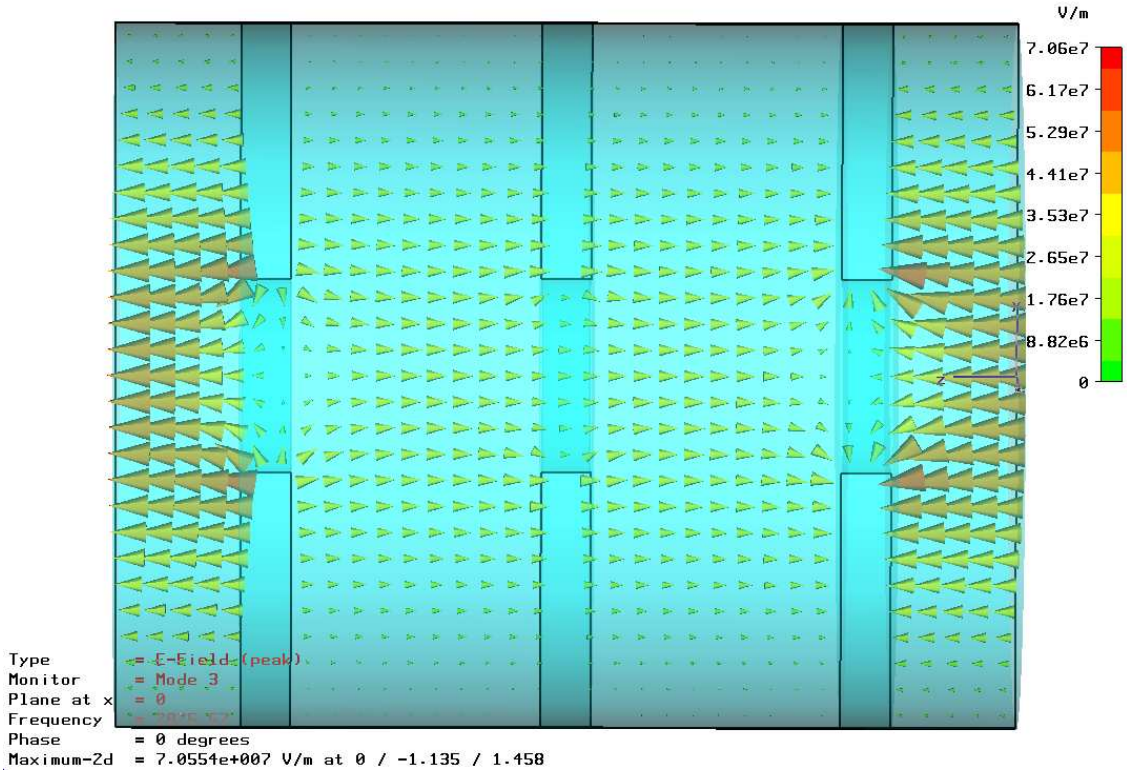

Figure 5.2: CST Simulation: Electric field in the SLAC Accelerating structure

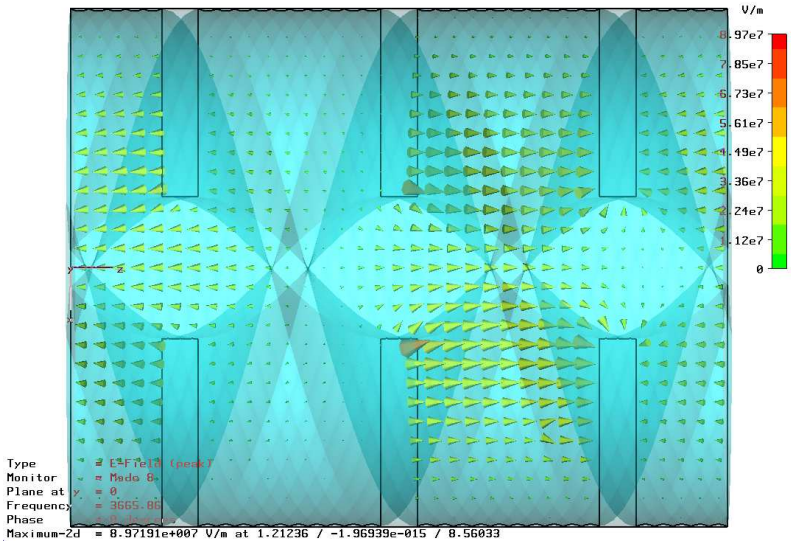

Figure 5.3: CST Simulation: Electric field in the longitudinal helical analog to the SLAC Accelerating structure

is examined, it is found that the electric field profile is directed along the z axis, and thus may be useful for particle acceleration.

However, the resonant frequency of the accelerating mode has changed to 3.67 GHz. This implies that the phase velocity of the wave is no longer c, but somewhat greater. In this case, $v_{ph} = 3.854 \times 10^8 \frac{m}{s} \approx 1.3c$. Therefore, the exact longitudinal helical analog will not give the desired accelerating mode, but the structure will have to be modified slightly to bring the phase velocity back down to c. This indicates that the procedure discussed in Section 2.2 for creating a twisted structure analog does not preserve the resonant frequency of the original structure. The parameters of the cavity must be altered slightly, and numerical methods must be used to predict the precise resonant frequency.

As another point of interest, the CST simulation of the disk-loaded accelerating structure took 48 seconds on a 3.6 GHz Pentium(R) 4 CPU with 2.5 GB of RAM, whereas the simulation of its longitudinal helical analog took 1 hour 31 min. (The same solver parameters were used for both simulations.) This is an indication of the tremendous difficulty conventional simulation softwares have with twisted structures and the need for more efficient simulation methods for these structures.

To lower the frequency (and thus the phase velocity), the cavity should be adjusted to be larger. However, the length of the cavity should not increase, because then both ω and β would decrease. Instead, only r_{cell} is increased, lowering ω and keeping β fixed, thus lowering v_{ph}. Choosing $r_{cell} = 5.493$ cm, CST simulation now predicts a mode with resonant frequency of 2.84 GHz, corresponding to a phase velocity of $2.98 \times 10^8 \frac{m}{s}$ for the electromagnetic wave in the cavity. This mode is shown in Figure 5.4 and appears to have roughly $\frac{2\pi}{3}$ phase advance per cell. Note that periodic boundary conditions were used for the walls in the z direction. When metal walls are used instead, the frequency changes to 3.046 GHz. Intuitively, we expect that as the cavity length gets longer (i.e. more cells are used), the resonant frequency will approach the solution using periodic boundary conditions. Table 5.2 compares values of f_{res}, V_{acc}, $\frac{R}{Q}$, and v_{ph} for the original SLAC structure, its longitudinal helical analog, and a helical structure whose outer radius has been increased to 5.493 cm. In these simulations, periodic boundary conditions were assumed for the end walls.

We also investigate the claim that at the center of the guide, only the fundamental (accelerating) space harmonic is present. A periodic boundary condition was established at the ends of the twisted structure. The Microwave Studio solution represents a standing wave rather than a traveling wave solution. Such a solution can be easily constructed from two counterpropagating traveling wave solutions. The z component of the electric field is plotted in Figure 5.5 for a particle on the z-axis, a particle 0.6 cm off axis, and a particle 0.9 cm off axis. Very far from the center of the guide near the groove region, it is easily seen that the field does not vary sinusoidally with the longitudinal coordinate z, indicating that many space harmonics are present in this region. On the other hand, close to the center of the guide, the field variation is sinusoidal as all space harmonics except the fundamental disappear. This verifies the claim of single space harmonic operation.

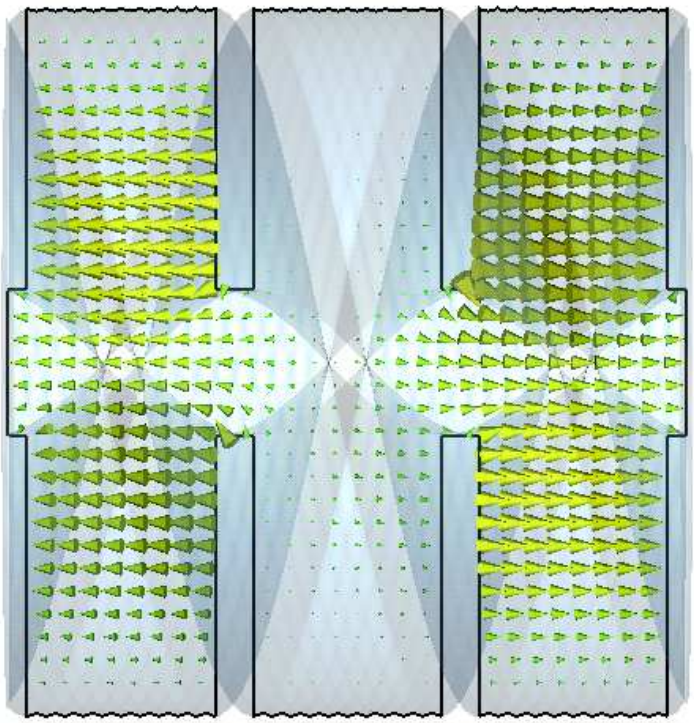

Figure 5.4: CST Simulation of Twisted SLAC-type cavity: Electric field with increased outer radius

Table 5.2: Comparison of disk loaded accelerating structures

	Original SLAC cavity	**Helical analog**	**Helical analog, increased outer diameter**
Frequency (GHz)	2.82	3.63	2.83
$\mathbf{V_{acc}(V)}$	3.99×10^6	3.63×10^6	2.16×10^6
U (Joules)	1	1	1
$\frac{\mathbf{R}}{\mathbf{Q}}$ (ohms)	448.6	287.9	131.3
$\mathbf{v_{ph}}\left(\frac{m}{s}\right)$	2.96×10^8	381×10^8	2.97×10^8

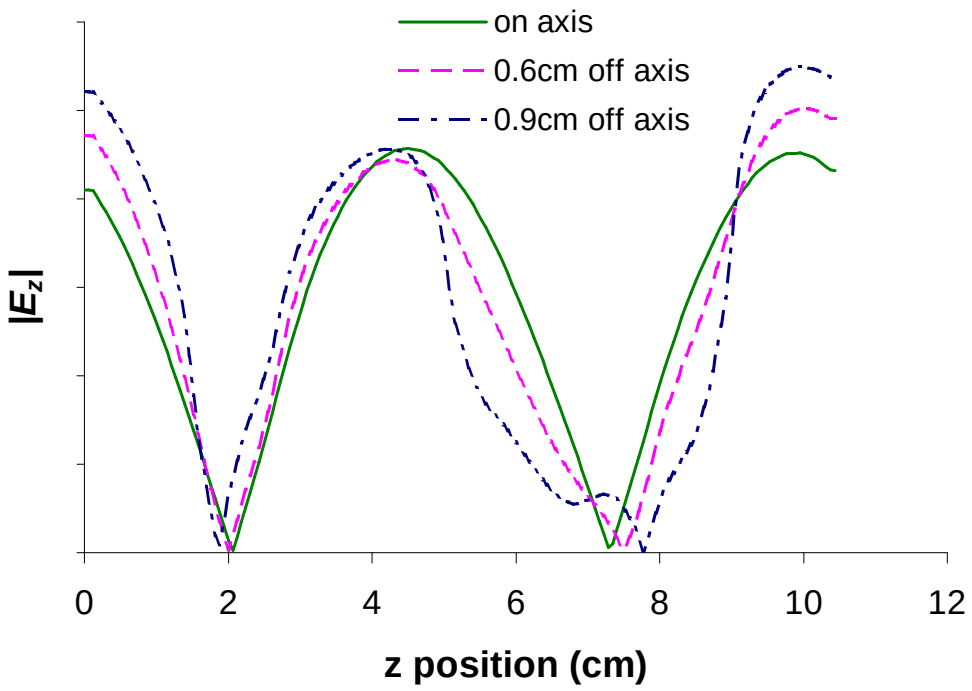

Figure 5.5: Magnitude of $\boldsymbol{E_z}$ for on-axis and off-axis particles: CST simulation

5.4 The Disk-loaded Accelerating Structure: an Optimization Case Study

To illustrate a typical design procedure for a twisted accelerating cavity, we demonstrate in this section how the developed model of twisted waveguides can be used to produce valuable design data for practical accelerators. We begin with the twisted disk-loaded structure just discussed. While there are infinite number of possible cross sections, this shape can be particularly instructive due to its simplicity. Other cavity shapes, such as the twisted elliptical cavity, can be thought of (at least to first order approximation) as a disk-loaded analog with rounded edges. We hold this transverse cross section constant, and require that the phase velocity of the mode of interest be equal to the speed of light. We allow the twist rate to vary, and also permit the frequency to change, as long as β changes so as to keep $v_{ph} = \frac{\omega}{\beta}$ the same. Say that the quantity we desire to optimize is $\frac{R}{Q}$.

The two dimensional frequency domain method is well-suited for this problem, since eigenmodes can be extracted easily by numerical eigen decomposition of the system matrix. For each twist rate, the value of β is first selected as to make the phase velocity c. This is done using many successive simulations and an iterative numerical root finding method (MATLAB's fzero function). At this point, the eigenvector can be extracted and the $\frac{R}{Q}$ value calculated. When this is performed for a variety of different twist rates, an appropriate twist rate can be chosen to ensure a high $\frac{R}{Q}$.

To calculate $\frac{R}{Q}$, we need to know the accelerating voltage as well as the total stored energy in the system (and of course the frequency, which we already know from the eigenvalue). For the 2D method, we do this for an infinitesimally small slice of the twisted guide of length dl, effectively giving $\frac{R}{Q}$ *per unit length.*

$$\begin{aligned} \frac{R}{Qdl} &= \frac{(V_{acc}/dl)^2}{2\omega(dU/dl)} \\ &= \frac{(E_z)^2}{2\omega(dU/dl)}. \end{aligned} \tag{5.11}$$

Next, we show that the energy stored per unit length in the twisted structure is the same whether calculated in cartesian coordinates or in twisted coordinates. In the original (nontransformed) system,

$$\begin{aligned} dE &= \frac{1}{2}\left(\bar{D}\cdot\bar{E} + \bar{B}\cdot\bar{H}\right)dxdydz \\ &= \frac{1}{2}\left(\epsilon\left|\bar{E}\right|^2 + \mu\left|\bar{H}\right|^2\right)dxdydz. \end{aligned} \tag{5.12}$$

The cartesian field components can be converted into components in the curvilinear coordinate

system using

$$\begin{bmatrix} E_x \\ E_y \\ E_z \end{bmatrix} = \left[\frac{\partial(x',y',z')}{\partial(x,y,z)}\right]^T \begin{bmatrix} E_1 \\ E_2 \\ E_3 \end{bmatrix} = J^T \begin{bmatrix} E_1 \\ E_2 \\ E_3 \end{bmatrix}, \tag{5.13}$$

where J is recognized as the Jacobian matrix of the transformation. Then,

$$\begin{aligned} dE =& \frac{1}{2}\left(\epsilon_0 \sum_i \left(\sum_j J_{ij}^T E_j\right)^2 + \mu_0 \sum_i \left(\sum_j J_{ij}^T H_j\right)^2\right) dxdydz \\ &= \frac{1}{2}\left(\epsilon_0 \sum_{i,j,k} J_{ij}^T J_{ik}^T E_j E_k + \mu_0 \sum_{i,j,k} J_{ij}^T J_{ik}^T H_j H_k\right) dxdydz \\ &= \frac{1}{2}\left(\epsilon_0 \sum_{j,k} E_j E_k \sum_i J_{ij}^T J_{ik}^T + \mu_0 \sum_{j,k} H_j H_k \sum_i J_{ij}^T J_{ik}^T\right) dxdydz \\ &= \frac{1}{2}\left(\epsilon_0 \sum_{j,k} E_j E_k \sum_i J_{ji} J_{ik}^T + \mu_0 \sum_{j,k} H_j H_k \sum_i J_{ji} J_{ik}^T\right) dxdydz \\ &= \frac{1}{2}\left(\epsilon_0 \sum_{j,k} E_j E_k g^{jk} + \mu_0 \sum_{j,k} H_j H_k g^{jk}\right) dxdydz. \end{aligned} \tag{5.14}$$

We can also relate the differential volume element $dxdydz$ to $dx'dy'dz'$ using

$$dxdydz = \left|\frac{\partial(x,y,z)}{\partial(x',y',z')}\right| dx'dy'dz' = \sqrt{g}dx'dy'dz', \tag{5.15}$$

where $g = det([g_{ij}])$. This gives

$$dE = \frac{1}{2}\left(\epsilon_0 \sum_{j,k} E_j E_k g^{jk} + \mu_0 \sum_{j,k} H_j H_k g^{jk}\right) \sqrt{g}dx'dy'dz'. \tag{5.16}$$

Next, we derive an expression for the energy in the transformed structure.

$$\begin{aligned} dE &= \frac{1}{2}\left(\bar{D}\cdot\bar{E} + \bar{B}\cdot\bar{H}\right) dx'dy'dz' \\ &= \frac{1}{2}\left([\epsilon]\bar{E}\cdot\bar{E} + [\mu]\bar{H}\cdot\bar{H}\right) dx'dy'dz'. \end{aligned} \tag{5.17}$$

Using the equivalent permittivity and permeability of Equation 3.7,

$$dE = \frac{1}{2}\left(\sum_i \sum_j \sqrt{g}\epsilon_0 g^{ij} E_j E_i + \sum_i \sum_j \sqrt{g}\mu_0 g^{ij} H_j H_i\right) dx'dy'dz'. \tag{5.18}$$

This is the same expression as Equation 5.16, indicating that the energy (or energy per unit length, as the case may be) calculated in the transformed coordinates is the same as in cartesian coordinates. This simplifies computation of quantities such as $\frac{R}{Q}$ using the proposed numerical methods.

The other quantity to be evaluated is the z component of the electric field on the center axis of the twisted guide. (This is used to calculate V_{acc}.) To do this, we utilize Equation 5.13 to obtain the component of the field along the cartesian z axis. We consider the generalized coordinate transformation of Equation 3.47. For this coordinate system,

$$\frac{\partial(u,v,w)}{\partial(x,y,z)} = \frac{1}{x'_u y'_v - y'_u x'_v} \begin{bmatrix} y'_v \cos pw + x'_v \sin pw & y'_v \sin pw - x'_v \cos pw & p(x'x'_v + y'y'_v) \\ -x'_u \sin pw - y'_u \cos pw & x'_u \cos pw - y'_u \sin pw & -p(x'x'_u + y'y'_u) \\ 0 & 0 & x'_u y'_v - y'_u x'_v \end{bmatrix}. \tag{5.19}$$

Conveniently, at the center of the guide (where $x' = y' = 0$), this yields the relation

$$E_z|_{x'=y'=0} = E_3|_{x'=y'=0}. \tag{5.20}$$

If a two dimensional method is used, this leads to the formula

$$\frac{R}{Ql} = \frac{(E_3|_{x'=y'=0})^2}{\omega \int\int \left(\epsilon_0 \sum_{i,j} g^{ij} E_i E_j + \mu_0 \sum_{i,j} g^{ij} H_i H_j \right) \sqrt{g} du dv} \tag{5.21}$$

To calculate the actual $\frac{R}{Q}$ value, the above formula should be multiplied by the length of the waveguide or cavity. This is because (neglecting end effects) the energy per unit length in the longitudinal direction is constant along the guide length.

We utilize this simple formula, combined with the two dimensional nonorthogonal finite difference frequency domain method to optimize a disk-loaded accelerating structure for $\frac{R}{Q}$ performance. Since the optimization requires many evaluations for different values of twist and propagation constant, the speed of the two dimensional method is a distinct advantage. Each simulation takes less than one second for a 25 by 25 mesh on a 1.86 GHz Intel processor. The dispersion curves for varying twist rates are shown in Figure 5.6.

In the current study, it was investigated how to maximize the value of $\frac{R}{Q}$ with respect to the rate of twisting for the twisted analog to the disk-loaded accelerating structure. We assumed that the structure was constrained to have a phase velocity equal to c for accelerating relativistic particles. For each value of the twist rate p, the frequency was adjusted in simulation in order to satisfy the phase velocity constraint. For the twisted analog to the disk loaded accelerating structure, we show $\frac{R}{Q}$ performance for inner radii of 0.7 cm, 1.135 cm (design value), and 1.5 cm. This is shown as a

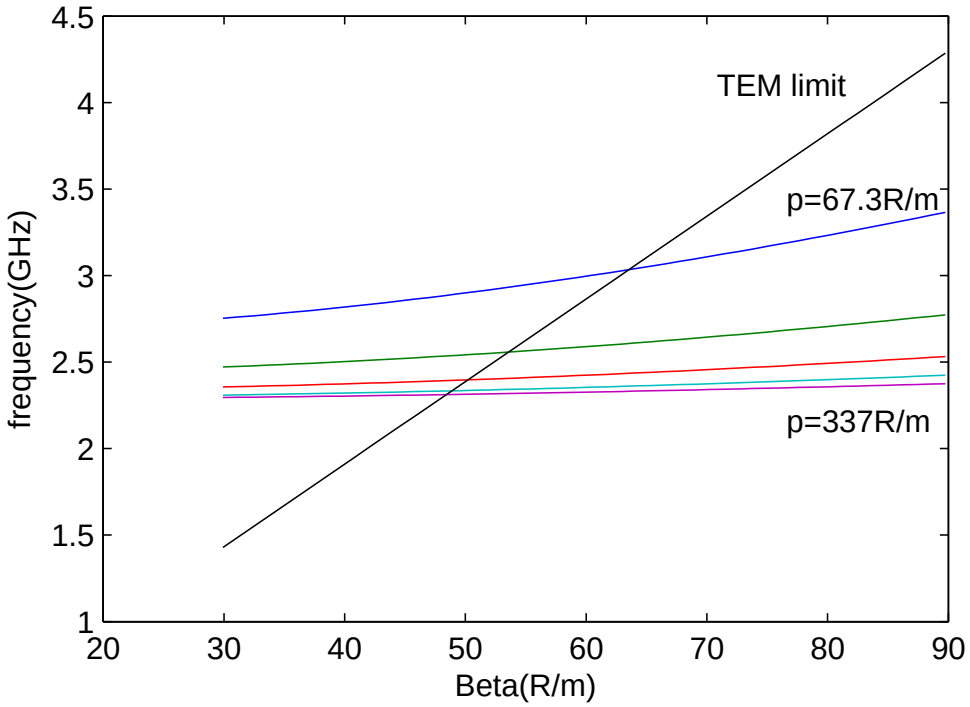

Figure 5.6: Predicted dispersion curves of the disk loaded twisted equivalent using the 2D frequency domain method for varying twist rates.

function of the twist rate in Figure 5.7. For the design case of 1.135 cm inner radius, the frequency should be adjusted as a function of the twist rate as shown in Figure 5.8.

In conventional accelerator cavities, a small iris radius is desirable for higher shunt impedances, but has the drawback that it decreases the maximum allowable size of the beam; so a design tradeoff is often needed. For the experimental prototype, the twist rate was only 89.76 $\frac{Rad}{m}$, so in practice a relatively higher value for the twist rate will yield higher values of $\frac{R}{Q}$. However, Figure 5.7 indicates that while the $\frac{R}{Q}$ can be increased somewhat by choosing a smaller inner radius, at low twist rates, a larger radius can actually be desirable.

We then investigated changing the parameter m in Equation 2.17. For a given twist rate, changing m leads to either compressing or expanding the longitudinal cross sectional shape in the axial direction. For even values of m, the cross section will be identical to that of a disk loaded cavity. For odd values of m, the cross section would be a "staggered" version of the original cross section. Again, we hold all other parameters constant, and show the effect of changing m on $\frac{R}{Q}$ as a function of the twist rate. We considered values of m ranging from 1 to 3, with $m = 2$ the design value. The results are presented in Figure 5.9. In general, the value of m does not effect the $\frac{R}{Q}$ value significantly except at high twist rates. However, higher values of m lead to a more complex structure and may be more difficult to manufacture. Generally, then, lower m values are preferable.

5.5 Twisted Elliptical (TESLA-type) Accelerating Structure

The TESLA (Tera electron-volt Energy Superconducting Linear Accelerator) cavity was designed to optimize performance for superconducting acceleratorating structures. The longitudinal cross section of a TESLA-type cavity is shown in Figure 5.1. The major and minor radii of the ellipses, the distance from each ellipse to the center axis, and the spacing of the ellipses along the z axis vary between accelerator designs.

To construct the longitudinal helical analog, we again follow the procedure in Section 2.2. The twisted cross section in this case resembles a "dumbell" shape, and is shown in Figure 5.10. This cross section, when rotated uniformly, gives the twisted structure shown in Figure 5.11.

The superconducting accelerator at the SNS currently employs two elliptical cavity designs; one for medium particle beta, and one for high particle beta. The medium beta cavity is selected for comparison with its longitudinal helical analog. Table 5.3 gives some important parameters of this SNS structure. A CST simulation of the fields in the cavity is shown in Figure 5.12. The operating frequency is 805 MHz. Only half of a full six-cell SNS cavity is simulated, making use of the symmetry of the structure which assures that $E_x \approx E_y \approx 0$ along the equator of each cell.

Upon simulating the longitudinal helical analog of the SNS cavity, it is discovered that the frequency is higher than the frequency of the normal SNS cavity (as was the case for the longitudinal helical analog of the SLAC-type cavity). Again, this change in frequency would result in a faster

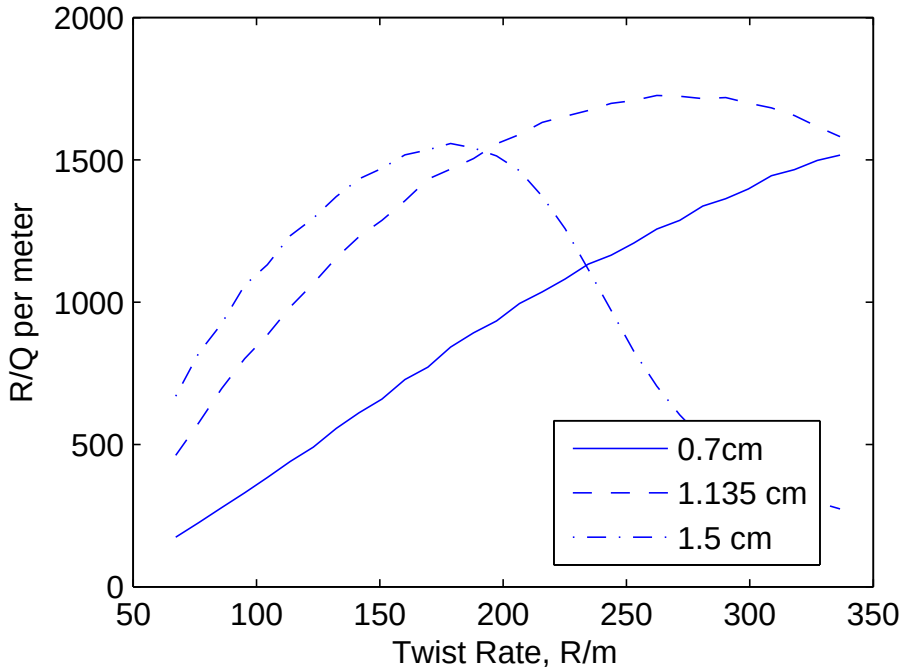

Figure 5.7: Simulated effect of changing the inner radius on $\frac{R}{Q}$.

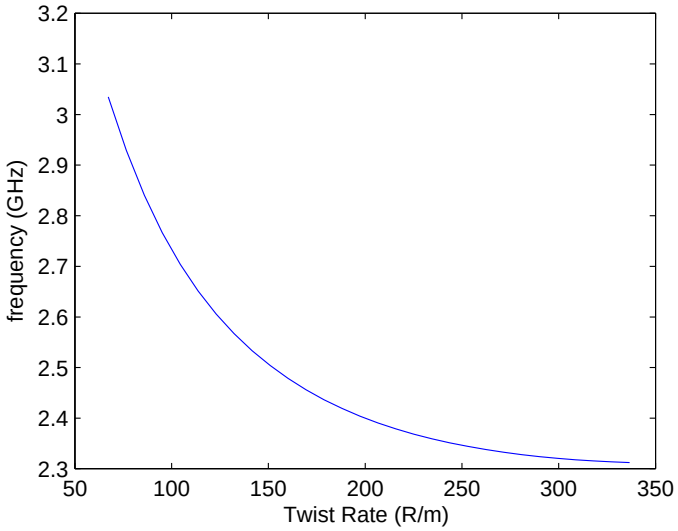

Figure 5.8: Simulated frequency as a function of twist rate. (Phase velocity held equal to c.)

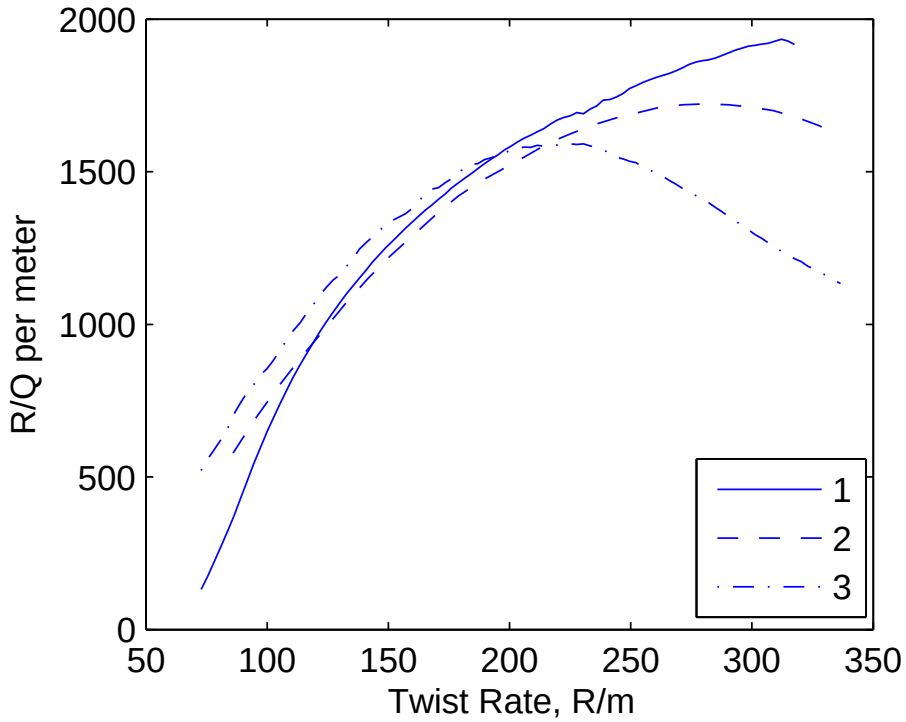

Figure 5.9: Simulated effect of changing m on $\frac{R}{Q}$.

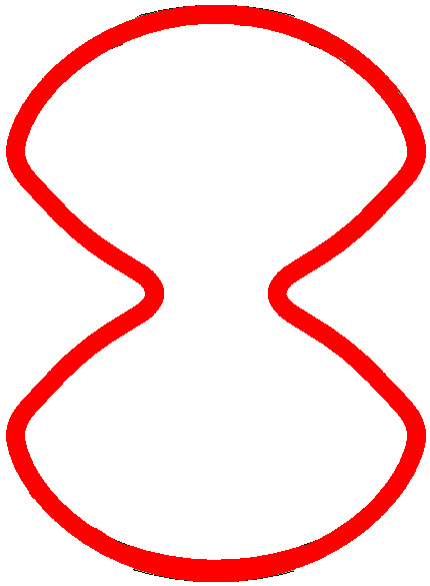

Figure 5.10: Twisted cross section for longitudinal helical analog to TESLA structure.

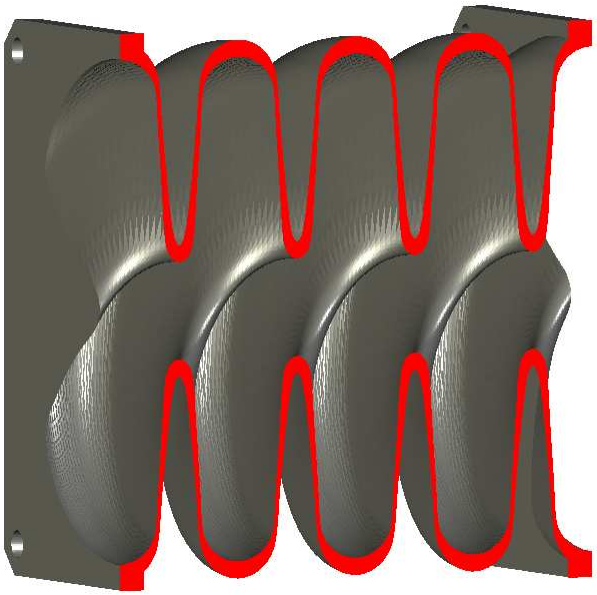

Figure 5.11: Longitudinal cross section of twisted TESLA-type cavity.

Table 5.3: Parameters for the SNS medium beta (beam beta = 0.61) accelerating cavity

Parameter	**Value**	**Unit**
Frequency	805	MHz
Length per Cell	11.36	cm
Inner radius	4.3	cm
Outer radius	16.396	cm
Phase advance per cell	π	Radians

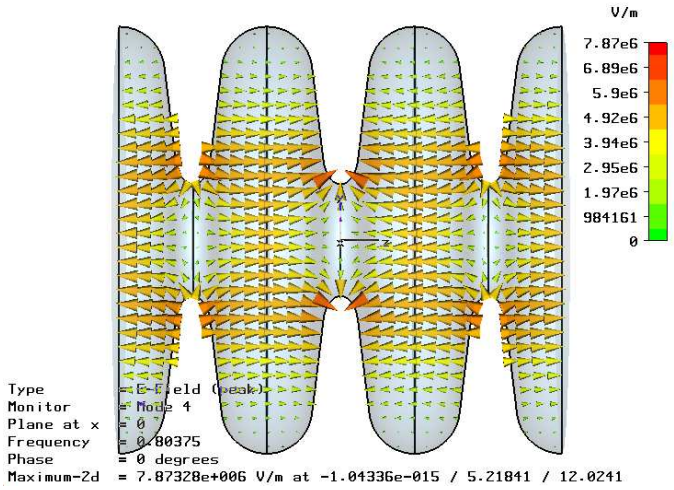

Figure 5.12: CST simulation of an SNS superconducting three-cell half-cavity.

phase velocity for the wave, so a slight redesign is necessary. In this case, the outer radius of the structure was increased from 16.4 cm to 22.16 cm, bringing the frequency down close to the original 805 MHz.

Some accelerating parameters of interest are shown in Table 5.4. Here, the original SNS medium beta superconducting accelerating cavity [44] is compared with its longitudinal helical analog as well as a variation with a larger diameter. The fields for the enlarged longitudinal helical analog are shown in Figure 5.13.

Table 5.4: Comparison of TESLA-type accelerating structures

	Original SNS cavity	**Helical LCS analog**	**LCS analog, increased outer diameter**
Frequency (MHz)	805	1059	797
$\mathbf{V_{acc}(V)}$	2.21×10^6	1.08×10^6	7.88×10^5
U (Joules)	2	1	1
$\frac{\mathbf{R}}{\mathbf{Q}}$ (ohms)	242.2	88.3	62.0
$\mathbf{v_{ph}}\left(\frac{m}{s}\right)$	1.83×10^8	2.41×10^8	1.81×10^8

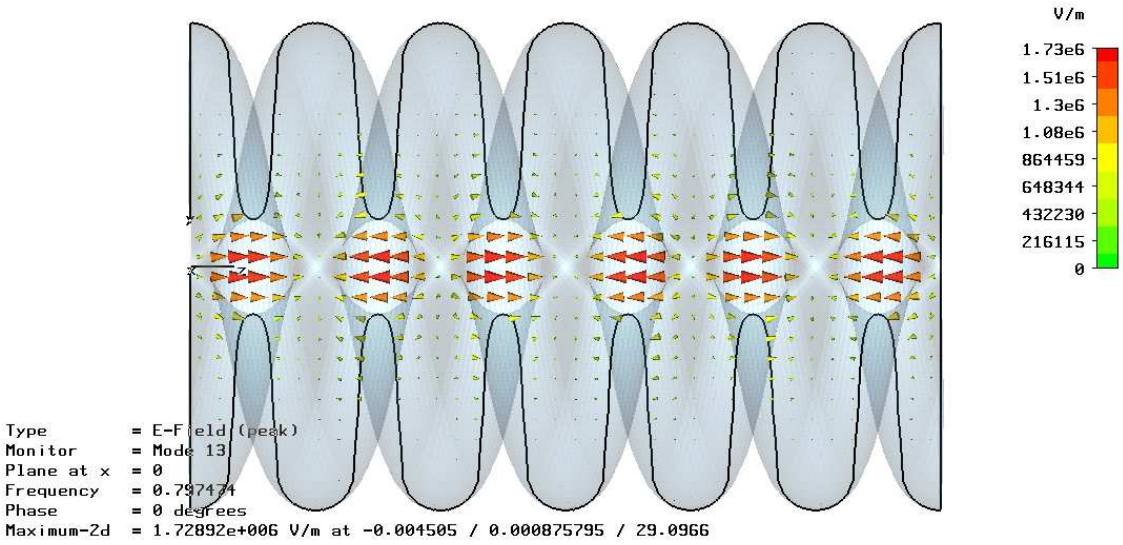

Figure 5.13: Electric field along a cross section of a helical TESLA-type cavity.

Chapter 6

Experimental Investigation

The properties of twisted structures are investigated by fabricating and measuring three types of twisted cavities. The prototypes were printed using a 3-D SLA printer. The structure was first printed layer by layer using a photo-curable liquid resin. It was then hardened using UV radiation. The inner surface and the flanges were then electroplated with copper to ensure electrical conductivity. The disadvantage of the SLA printing method is that due to its finite layer thickness, fine ridges can be seen on the surface. However, this can be tolerated for 2.8 GHz operation.

To measure the structures, shorting walls are introduced to form a cavity resonator whose resonant frequencies can be measured and compared with simulation results. With two probes located at different places throughout the structure, S_{21} can be measured and from this the resonant frequencies can be obtained. Moreover, the electric field distribution along the axis of the structure can be measured through a technique known as "bead pulling" (see [45], for example). In this method, a small hollow cylindrical conductor is pulled through the cavity via a small hole. As the metallic bead moves, it interacts with the electric field and causes a change in resonant frequency proportional to the strength of the electric field at the location of the bead. Such a measurement system has been prepared and is shown in Figure 6.1.

For these measurements, the bead used was a small needle whose volume was calculated to be $\Delta V = 1.12 \times 10^{-9} m^3$. The needle had length $l = 3.6mm$ and diameter $d = 0.63mm$. This leads to an aspect ratio of 5.71. According to [46], for $l/d \gg 1$, the metallic cylinder can be considered to be a spheroid of major axis $l/2$ and minor axis $d/2$. Making this approximation, we calculate the eccentricity

$$e = \sqrt{1 - \frac{d^2}{l^2}} = 0.985. \tag{6.1}$$

From here, the depolarization is calculated using [46].

$$L_{\parallel} = \frac{1+e^2}{e^3}\left(\frac{1}{2}\ln\frac{1+e}{1-e} - e\right), \tag{6.2}$$

Figure 6.1: Bead and test setup for bead pull measurements.

from which we have the depolarization factor

$$F_1 = \frac{1}{3L_\parallel}. \tag{6.3}$$

Finally, the $\frac{R}{Q}$ is calculated from the formula

$$\frac{R}{Q} = \frac{1}{3\pi f_0 \Delta V F_1 \epsilon_0} \left[\left(\int \sqrt{\frac{\Delta f}{f_0}} \cos kz \, dz \right)^2 + \left(\int \sqrt{\frac{\Delta f}{f_0}} \sin kz \, dz \right)^2 \right], \tag{6.4}$$

which is the same as the formula given in [46], except for a factor of 2 which is due to the fact that we used the definition

$$\frac{R}{Q} = \frac{V_{acc}^2}{2\omega U}, \tag{6.5}$$

where V_{acc} is the on-axis accelerating voltage and U is the stored energy. Δf was measured indirectly through measuring the phase of the transmission coefficient S_{21} and using the approximation

$$\frac{\Delta f}{f_0} = \frac{\tan(\angle S_{21})}{2Q_L}, \tag{6.6}$$

where Q_L is the measured (loaded) Q of the cavity. Since Δf is proportional to E_z^2, it always has the same sign. To calculate $\sqrt{\frac{\Delta f}{f_0}}$, then, requires that the correct branch of the square root be judiciously chosen. To do this, we examined the Δf data and found points where it was nearly zero and the corresponding intervals in between such zero points. Every other interval was then multiplied by -1 to recover the appropriate sign for $\sqrt{\frac{\Delta f}{f_0}}$.

To investigate whether end effects played a significant role in the twisted cavity, two identical prototypes were made of each type. The two prototypes could be joined together using the attached flanges in order to make a new prototype that was twice as long as the individual ones. By so increasing the length of the cavity, it could be seen whether there was any significant difference in the resonant frequencies and directly attribute any such differences to end effects.

6.1 Twisted Rectangular Prototype

A twisted rectangular prototype was designed to work near 2.8 GHz. Each prototype has cross-sectional dimensions 3.214" by 1.429" and has two complete twists over a length of 8.929". Figure 6.2 shows this completed prototype.

Initial measurements were taken on this prototype by placing a copper plate on each end of

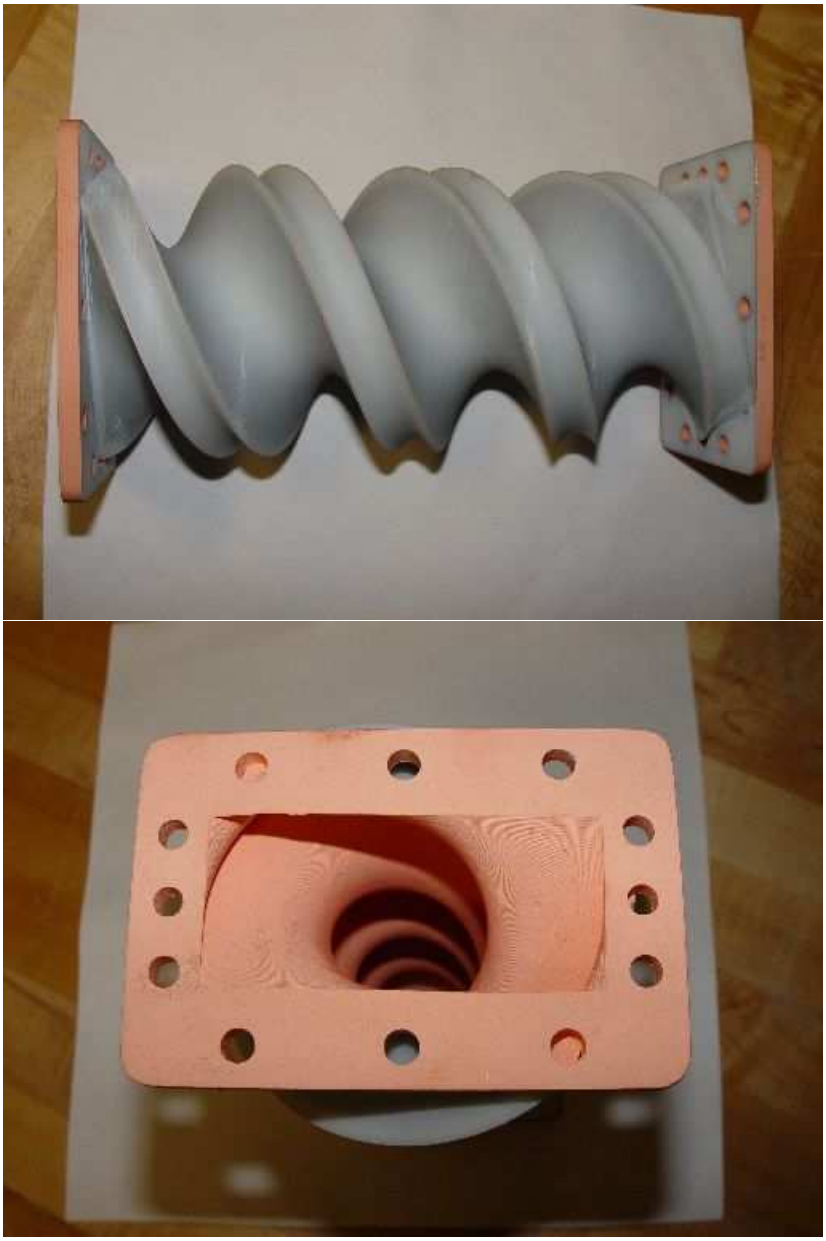

Figure 6.2: Twisted rectangular waveguide prototype.

the waveguide, effectively turning it into a resonant cavity as described above. Two small probes were inserted in the end plates, and a vector network analyzer was used to measure S_{21} over a wide range of frequencies. The maxima of $|S_{21}|$ correspond to the resonant modes of the cavity structure. Figure 6.3 shows S_{21} over the range of frequencies spanning the first four TE-type modes of the resonant cavity. The frequencies and Q values for these modes are shown in Table 6.1. These measurements were used to validate the newly developed three dimensional NFDTD solver. The measured frequencies are compared with simulation results and found to be within 0.5% of each other. An 18 X 8 X 50 grid was employed, and the simulation was allowed to run to 50 ns.

Since the cavity is rather short, end effects were found to limit the effectiveness of the two dimensional code for this case. This is because the 2D code solves the structure as if it were infinite. (For this particular prototype, the 2D codes yielded up to 1.8% frequency deviation from experiment.) Therefore, to further validate the effectiveness of the 2D code, the two identical prototypes were placed together to make one twisted guide that was twice as long (now with 4 complete twists). The measurement results for the short and long cavities as well as the 2D NFDTD and 2D NFDFD results are shown in Table 6.2. A 72 X 32 mesh was used.

The trend in the experimental results of Table 6.2 indicates that as the cavity gets longer, the measured resonant frequency approaches the predictions of the 2D methods, as expected. In the limiting case of an infinite structure, end effects should become negligible, and it is expected that the 2D method will perform quite well. The dispersion curves for the short prototype are shown in Figure 6.4.

Clearly for this (rather rapid) twist rate, the perturbation theory method fails to provide adequate results. This is to be expected, of course, since perturbation theory was designed to work only when the twist rate is small. Among the other simulation methods presented here, the 3D methods outperform the 2D methods. This could be explained by the finite length of the prototypes. The short twisted rectangular prototype has only two complete twists, so end effects introduced by the copper end walls could play a significant role in the electromagnetics of the resonator. The longer prototype has twice as many turns, so end effects should be reduced to some extent. It is for such long structures that the 2D codes begin to show their real advantage.

The bead pull measurement system was tested on this rectangular twisted structure. Figure 6.5 shows an example of the measurement results for the third mode (at 2.95 GHz). The three distinct minima in $arg\,(S_{21})$ indicate the three half cycles of the electric field magnitude along the length of the cavity. These minima correspond to the positions along the cavity at which the magnitude of the electric field is the greatest. The irregularities on both edges of the cavity are evidence of the role of end effects. Thus, the bead pull system can be useful in identifying individual modes.

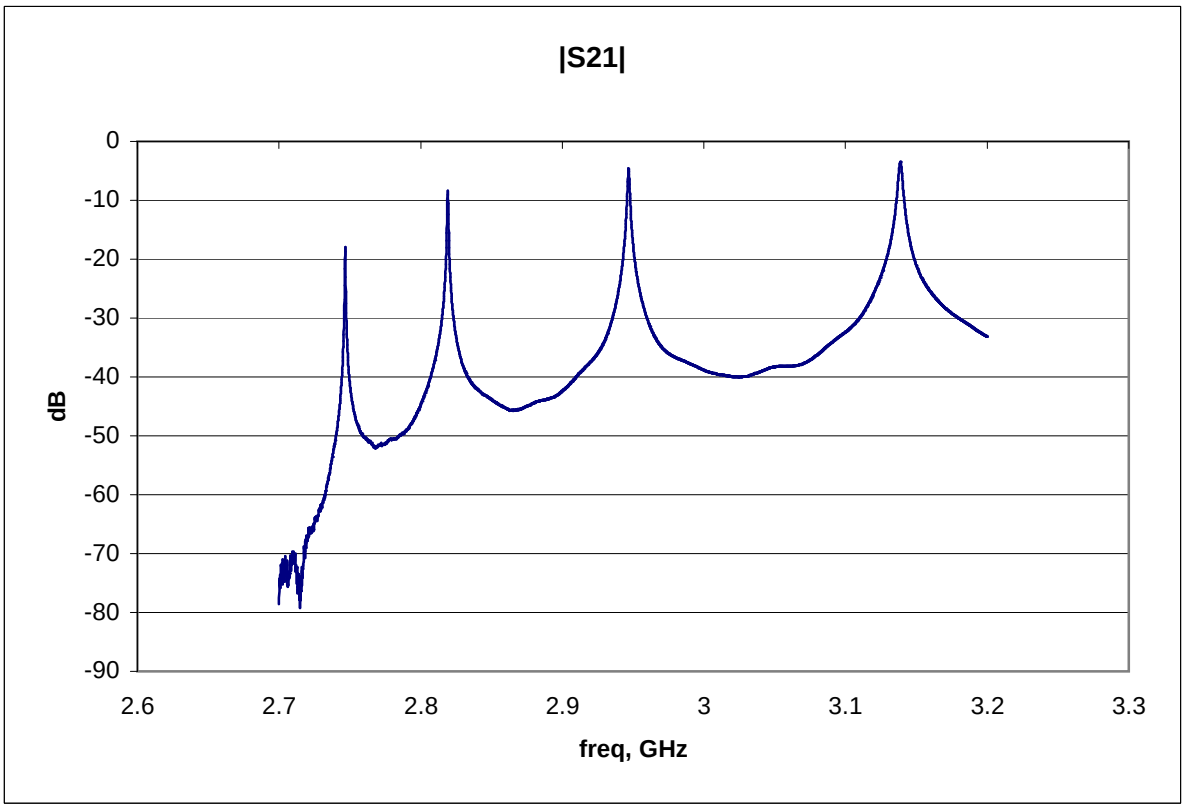

Figure 6.3: $|S_{21}|$ for the twisted rectangular prototype showing resonances.

Table 6.1: Experimentally measured first four TE modes for the twisted rectangular prototype compared to 3D simulation method results.

	Measured frequency	**Q**	**Simulation Frequency (3D NFDTD)**	**Deviation from experiment**
Mode 1	2.747 GHz	7001	2.734 GHz	0.47%
Mode 2	2.820 GHz	3977	2.808 GHz	0.43%
Mode 3	2.947 GHz	1921	2.940 GHz	0.24%
Mode 4	3.139 GHz	1003	3.135 GHz	0.13%

Table 6.2: Short and long prototype resonant frequencies compared to 2D simulation method results.

Short prototype frequency	Long prototype frequency	2DNFDTD	2DNFDFD
2.747 GHz	2.743 GHz	2.734 GHz	2.735 GHz
2.820 GHz	2.808 GHz	2.794 GHz	2.794 GHz
2.947 GHz	2.932 GHz	2.907 GHz	2.906 GHz
3.139 GHz	3.119 GHz	3.083 GHz	3.082 GHz

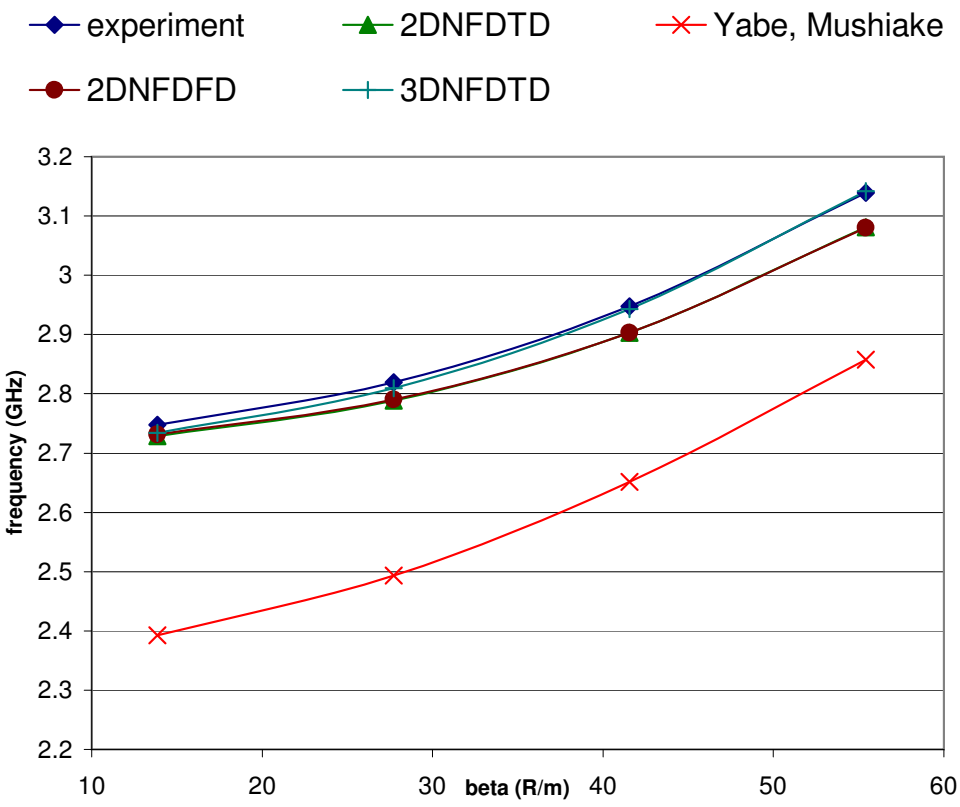

Figure 6.4: Dispersion curves showing measured and predicted resonant frequencies for twisted rectangular cavity.

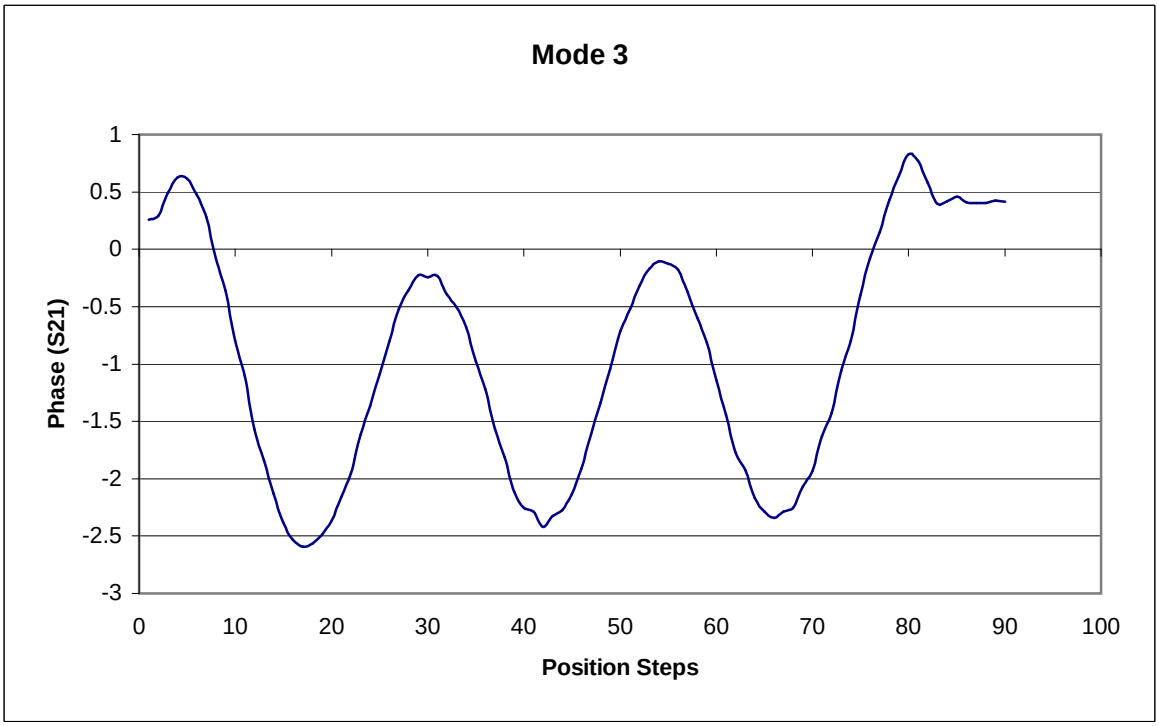

Figure 6.5: Bead pull measurement of the large twisted rectangular prototype for third mode. Measurements for other modes were similar, except with different number of cycles.

6.2 Twisted Disk-Loaded Analog Prototype

A twisted version of a disk-loaded waveguide has also been designed. The base design was taken directly from SLAC, although the outer radius was increased as discussed in Section 5.3 in order to bring the phase velocity of the mode of interest down to c. Table 6.3 gives the physical parameters of the twisted disk loaded equivalent. The 2.8 GHz disk loaded prototype is shown in Figure 6.6. The measurements were performed using two prototypes joined end-to-end to achieve six complete twists.

First, the spectrum of the cavity was obtained by measuring $|S_{21}|$ on a network analyzer. The results are given in Figure 6.7. Since many modes were present in this spectrum, bead pull measurements were performed on many different modes to determine the intensity of the electric field on the axis of the guide. Since the mode of interest here is the $\frac{2\pi}{3}$ mode, the bead pull measurement should reveal two complete cycles over the six cell cavity. This mode was indeed found, and the bead pull results are shown in Figure 6.8. Note again that the phase advance per $\frac{1}{2}$ turn is determined by the number of twists in a structure, and is not directly related to the phase advance defined in conventional corrugated structures.

The appearance of the electric field along the cavity axis is seen to be roughly sinusoidal in the center of the cavity. Since theory predicts the existence of only one space harmonic along the center axis, and hence a simple sinusoidal variation of the electric field, a sinusoidal curve was designed to fit the measured data and is shown alongside the data in Figure 6.8. The sinusoid fit has distribution

$$y = A\sin(kz + \phi), \tag{6.7}$$

where

$$k = \frac{\omega}{\beta c}. \tag{6.8}$$

Here, β is the relativistic quantity that is equal to 1 for the twisted analog of the disk-loaded cavity. The other constants, A and ϕ, are chosen to best fit the measured data. These data show that the electric field has a sinusoidal appearance close to the center of the cavity, while end effects cause a deviation close to the cavity end walls. This is expected from our analysis results.

Table 6.3: Parameters for twisted analog to disk-loaded accelerating cavity

Parameter	**Value**	**Unit**
Outer radius	5.493	cm
Inner radius	1.135	cm
Twist Rate	89.76	Radians/m
Phase advance per $\frac{1}{2}$ turn	$\frac{2\pi}{3}$	Radians
Notch angle	30	Degrees

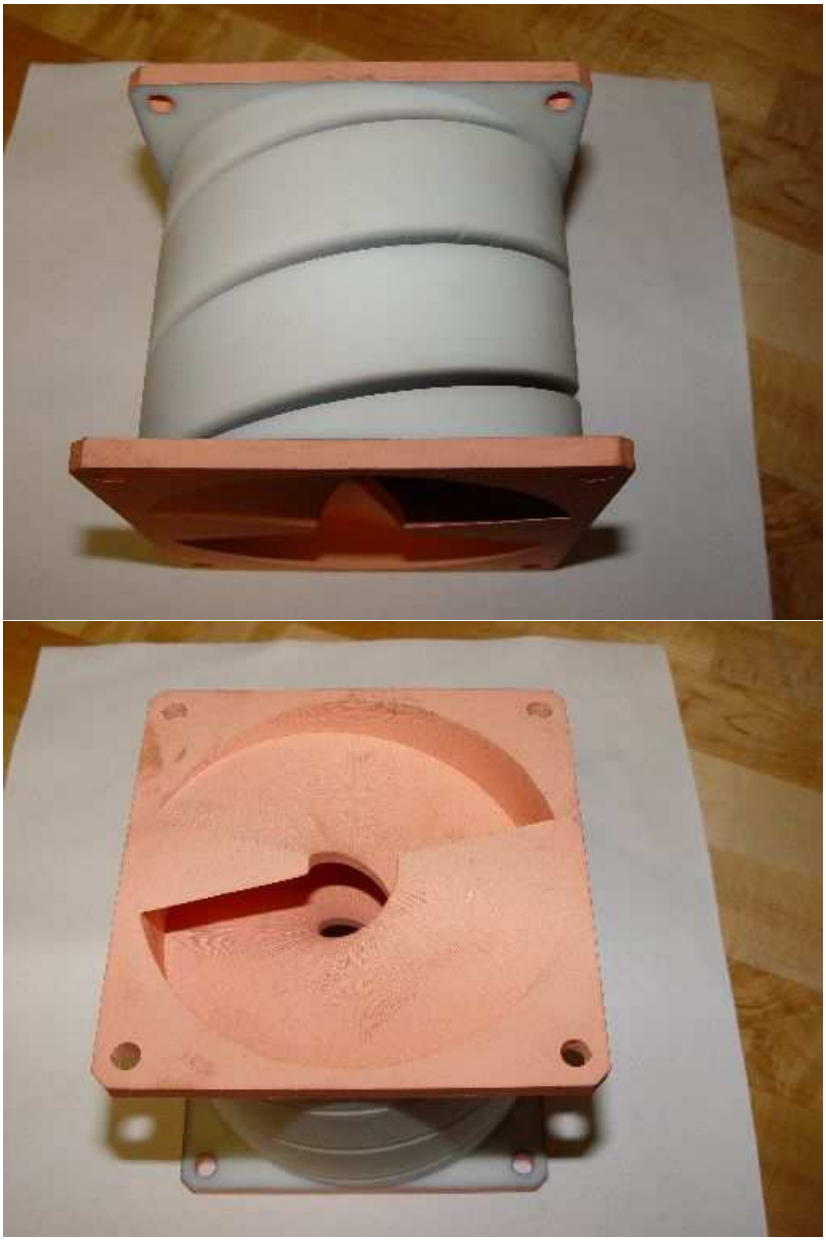

Figure 6.6: Large twisted disk-loaded waveguide prototype.

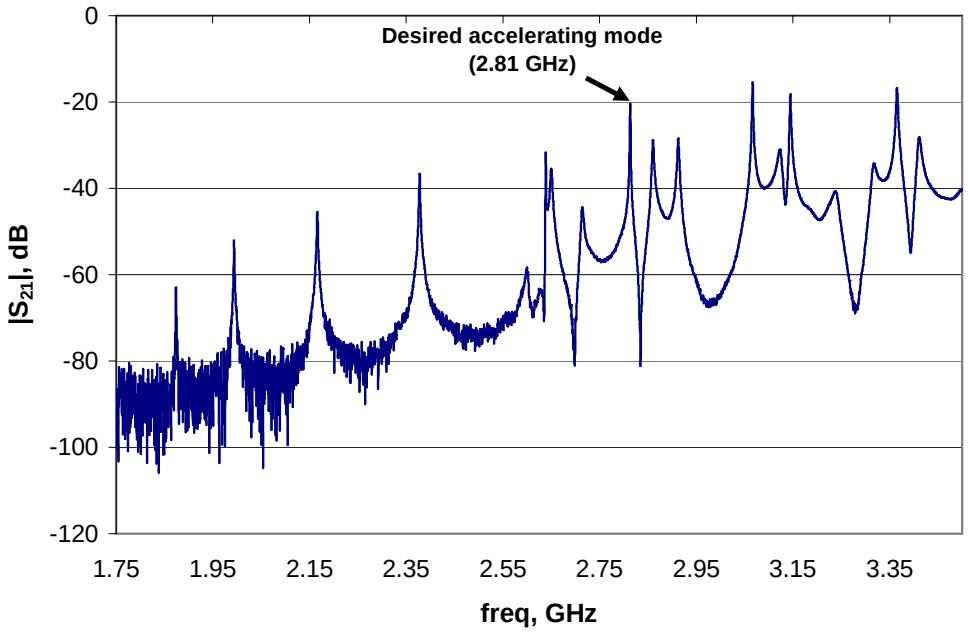

Figure 6.7: Measured transmission spectrum of twisted analog of the disk-loaded cavity, showing resonances.

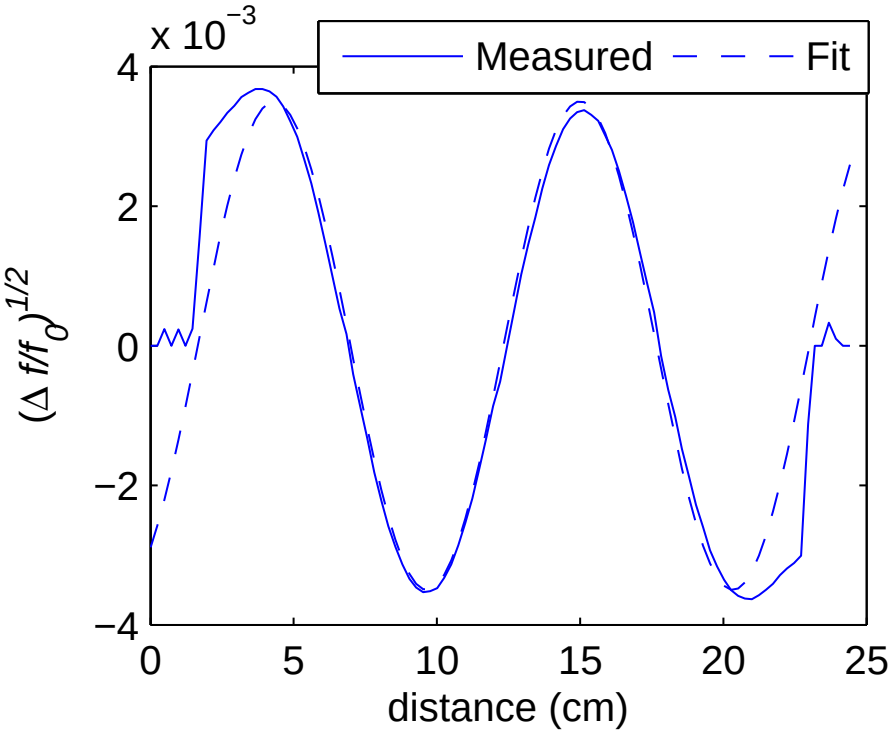

Figure 6.8: Measured field in the twisted analog of the disk-loaded cavity.

Using bead pull measurements for several surrounding modes as well, it was possible to determine the value of the phase constant for each mode as well as the frequency. This allowed us to construct the dispersion curves for several different modes and compare to the dispersion curves predicted by the developed numerical model. The comparison is shown in Figure 6.9.

Since the disk loaded twisted equivalent has potential accelerator application, the $\frac{R}{Q}$ value was determined experimentally. The measured $\frac{R}{Q}$ was for a standing wave pattern, while in the simulation we assumed a traveling wave. If a standing wave mode is considered a sum of two traveling wave modes, it is obvious that only the forward traveling wave (traveling synchronously with the particle) contributes to the acceleration, and thus to the value of V_{acc}. However, the energy of the wave will reflect both the forward and backward components. As a result, the traveling wave $\frac{R}{Q}$ is twice the standing wave value. Thus, to calculate the traveling wave $\frac{R}{Ql}$, the measured $\frac{R}{Q}$ was multiplied by 2 and taken over the length of the cavity.

Using this method to calculate $\frac{R}{Q}$ for the accelerating mode, a measured $\frac{R}{Ql}$ of 776 Ω/m was obtained, while simulation predicted 716 Ω/m. There are several sources of measurement error. The formulas given in [46] (and repeated in Equation 6.4) are only valid if all other field components except E_z are zero, which is a good approximation, but may not be exactly the case for the measured twisted structures. Temperature drift during the measurement and uncertainty regarding the precise value of the form factor for the perturbing metal bead also contributed some error. In addition, end effects may play a role, causing an increase of the field strength close to the metal end walls of the cavity. This would cause the measured $\frac{R}{Ql}$ to be more than what would be predicted assuming the twisted structure was infinite in length, explaining why the measured $\frac{R}{Ql}$ values to be higher than predicted for an infinite structure.

The problem of reducing end effects requires careful consideration. Although not addressed in detail here, it has been shown previously [8] that in some cases the end effects can be mitigated by introducing a curved boundary surface as the end wall. Another approach is to eliminate the end walls and leave them open to a waveguide interface, which then has to be properly matched to the twisted structure. These considerations are beyond the scope of the present research.

6.3 Twisted TESLA-type Prototype

An elliptical twisted cavity based on the TESLA design was constructed. The base design was the same as for the SNS medium beta superconducting cavity (although the dimensions have been scaled for 2.8 GHz operation (the original frequency was 805 MHz). Also, the outer diameter of the cavity has been increased, as discussed in Section 5.5. Thus, the phase velocity and beam beta is the same for the prototype as for the original SNS cavity. This facilitates a more direct comparison between cavity types. Figure 6.10 shows the 2.8 GHz TESLA-type prototype.

Carrying out the measurements in the same way as for the disk-loaded equivalent, we first measured the spectrum. The transmission is shown in Figure 6.11. Since the mode of interest here

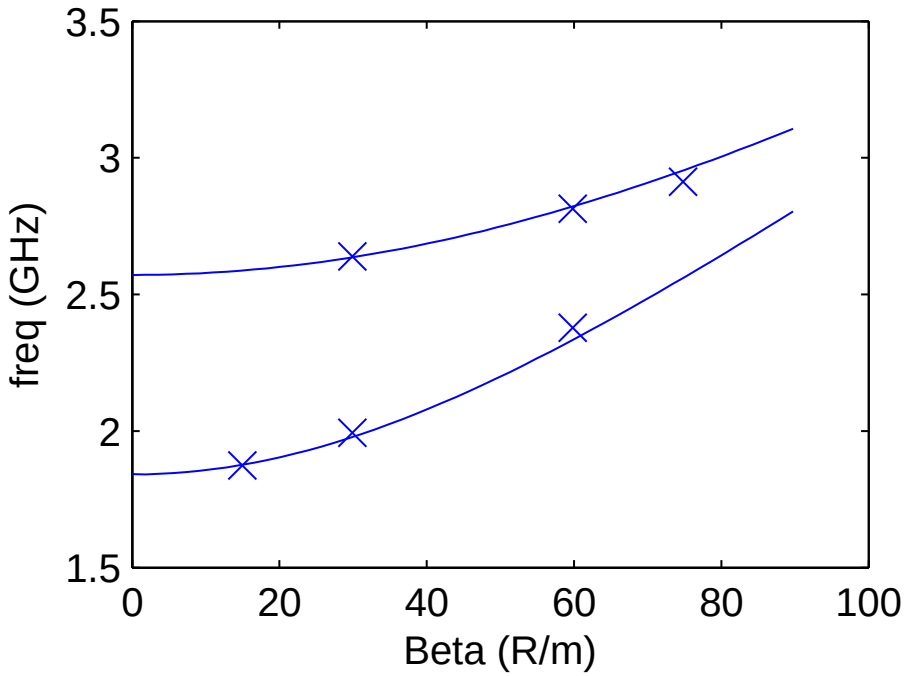

Figure 6.9: Predicted and measured dispersion curves for two modes of a twisted analog to a disk-loaded cavity. The mode with higher frequency is the TM accelerating mode. The x's are experimental points.

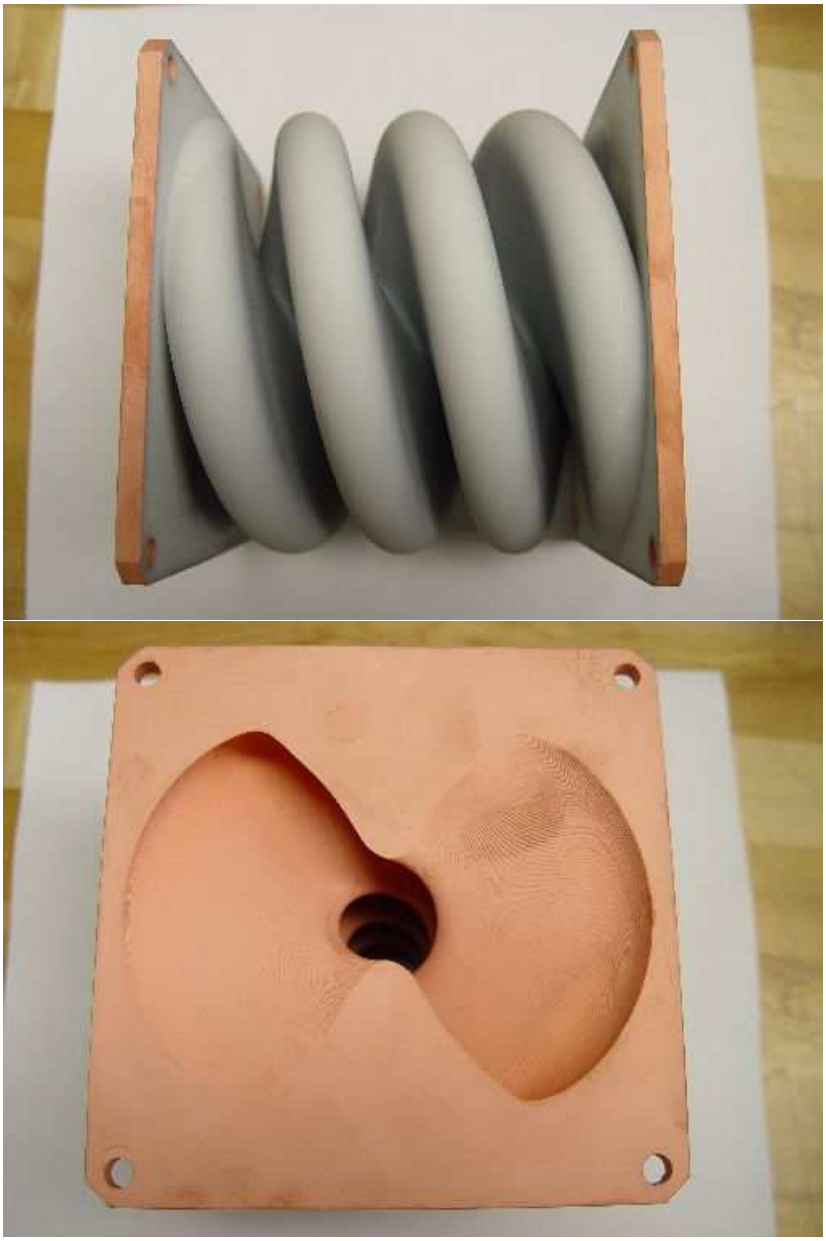

Figure 6.10: Large twisted TESLA-type waveguide prototype.

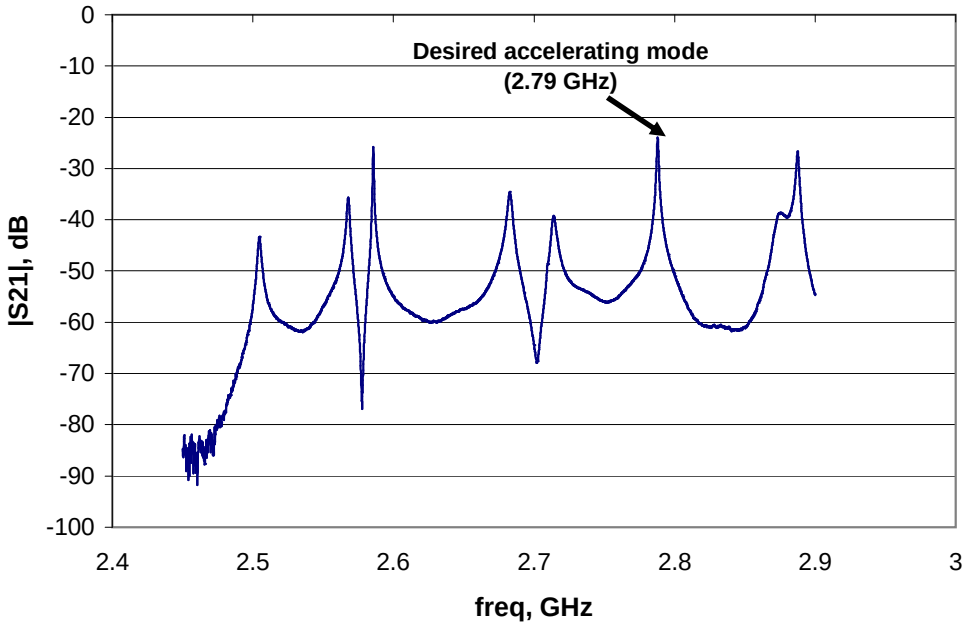

Figure 6.11: Measured transmission spectrum of twisted analog of the elliptical cavity, showing resonances.

is the π mode, the bead pull measurement should reveal eight complete cycles over the six cell cavity. This mode was found, and the bead pull results are shown in Figure 6.12.

The dispersion curve for the accelerating mode is shown in Figure 6.13. Many additional resonances were observed other than the ones shown in Figure 6.13, but their relatively low Q values afforded by the rough cavity walls and other experimental factors prohibited an accurate bead pull measurement of these modes. However, the data points gathered for the accelerating mode of interest show good agreement with theory.

The $\frac{R}{Q}$ of the structure was measured using the same technique as before, and a value of 248 Ω/m was obtained, compared to a simulated value of 223 Ω/m.

6.4 Summary

Three types of twisted prototypes were designed and fabricated, and a number of measurements were performed. The spectrum for each prototype was obtained by transmission measurement using a network analyzer. The resonant frequencies were obtained in this manner. Several modes were then selected for bead pull measurements, which allowed an investigation of the intensity of the electric field on the axis of the twisted guide. The measured electric field distributions confirmed the prediction from theory that only a fundamental space harmonic is present on the axis of the guide.

The bead pull results also provided a value for the phase constant for each mode. This allowed the dispersion curves to be experimentally obtained and compared with numerical simulation. There was generally excellent agreement between measurement and simulation, further validating the accuracy of the numerical model. The bead pull results also allowed the correct accelerating mode to be selected. This accelerating mode was evaluated for $\frac{R}{Q}$ performance, and good agreement was obtained between measured results and those predicted by numerical simulation.

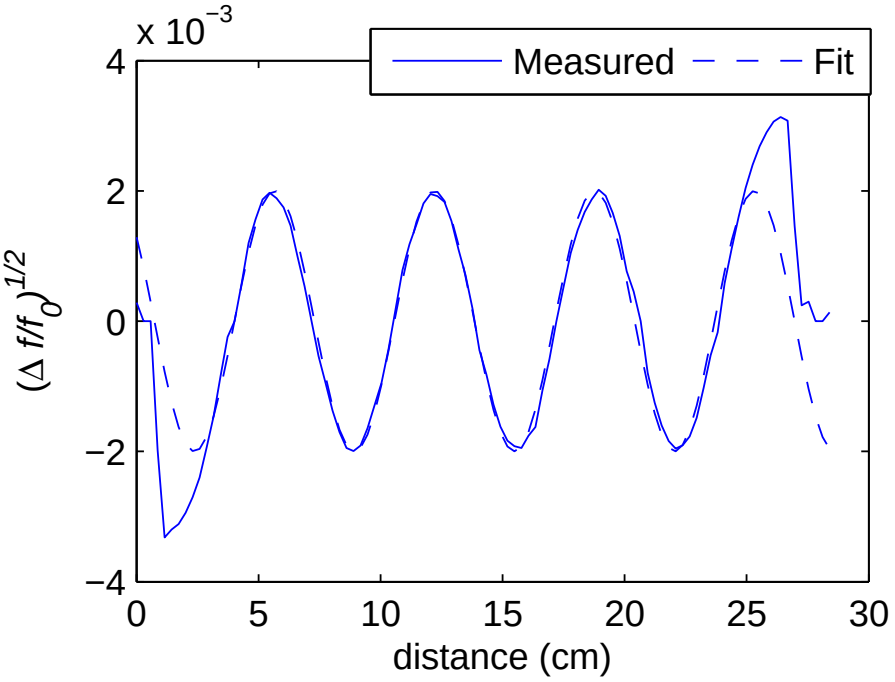

Figure 6.12: Measured field in the twisted analog of the elliptical cavity.

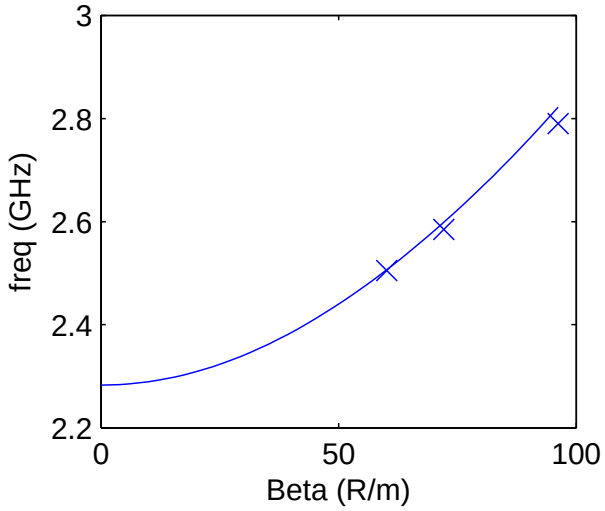

Figure 6.13: Predicted and measured dispersion curves for the accelerating mode of an elliptical twisted guide. The x's are experimental points.

Chapter 7

Conclusion

Twisted waveguides of various cross-sectional geometries were considered and analyzed. In particular, the slow-wave and dispersion properties of twisted structures were investigated. It was shown that a twisted waveguide can support waves that travel at speeds slower than c. The structures considered here have many potential applications in electron traveling wave tubes, linear particle accelerators, undulators, and wigglers.

Since there is no closed form solution for the electromagnetic fields within a twisted waveguide or cavity, several previously proposed approximate methods were analyzed, and new numerical methods were developed that could be generalized to arbitrary cross sections. Finite difference-based numerical methods were developed in both the time and frequency domains, and in 2D and 3D. 3D methods have advantages for analyzing short structures, where end effects play less of a role in determining the overall electromagnetic properties of the structure. 2D methods, on the other hand, are capable of simulating an infinite twisted structure much more efficiently. The time domain methods that have been developed have the advantage of being simple, completely explicit, and capable of solving many modes simultaneously given an initial condition. The frequency domain method, on the other hand, is not in danger of instability, and is capable of directly extracting the eigenmodes of the guides.

Twisted waveguides and cavities offer a number of advantages as accelerating structures. In designing a good accelerating cavity, it is very important to maximize the accelerating space harmonic with respect to all other harmonics, which do not contribute to acceleration and can have detrimental effects on the beam. A twisted guide, on the other hand, has no higher space harmonics on the beam axis. Also, the twisted guide could offer much improved handling of higher order trapped accelerating modes, since such modes can propagate freely out of the twisted guide and into the higher order mode dampers. This is a consequence of the uniform cross section of the guide. Finally, the group velocity at π mode can be nonzero, improving mode spacing.

Three particular cross sections were selected for analysis. First, a twisted rectangular cavity is analyzed as a reference case. This is because the shape is simple and perturbation theory already

gives a good approximate solution for slow twists. Secondly, a symmetrically notched circular cross section is investigated, since its longitudinal cross section is comparable to the well known disk-loaded cavity (used in many accelerator designs, including SLAC). Also, the notched cross section can be analyzed analytically to some extent using periodic structure theory and field matching. Finally, a "dumbbell" shaped cross section is analyzed because of its similarity to the well-known TESLA-type elliptical accelerating cavity.

To validate the results of the theory and simulations, several prototypes were developed employing these three basic shapes. These prototypes were designed for operation at 2.8 GHz. Measurements were performed on the prototype cavities to determine the field distributions within the cavities and the dispersion characteristics. These measurements indicated that there is good agreement between theory and experimental data in terms of resonant frequencies, dispersion characteristics, and axial electric field strength.

Bibliography

Bibliography

[1] B. A. et al., "Superconducting TESLA cavities," in *Physical Review Special Topics - Accelerators and Beams, 092001*, vol. 3, 2000.

[2] C. Jing, W. Gai, J. Power, R. Konecny, S. Gold, W. Liu, and A. Kinhead, "High-power RF tests on x-band dielectric-loaded accelerating structures," *IEEE Transactions on Plasma Science*, vol. 33, no. 4, pp. 1155–1160, Aug. 2005.

[3] J. Power, W. Gai, S. Gold, A. Kinkead, R. Konecny, C. Jing, W. Liu, and Z. Yusof, "Observation of multipactor in an alumina-based dielectric-loaded accelerating structure," *Physics Review Letters*, vol. 92, no. 16, Apr. 2004.

[4] C. Jing, W. Liu, W. Gai, J. Power, and A. Kanareykin, "34.272 GHz multilayered dielectric-loaded accelerating structure," in *Proceedings of 2005 Particle Accelerator Conference*, 2005, pp. 1952–1954.

[5] R. P. Borghi, A. L. Eldredge, G. A. Loew, and R. B. Neal, *Design and Fabrication of the Accelerating Structure for the Stanford Two-Mile Accelerator.* Academic Press, New York, N. Y., vol. 1.

[6] J. Sekutowicz, "TESLA superconducting accelerating structures," *Measurement Science and Technology*, vol. 18, no. 8, pp. 2285–2292, 2007.

[7] T. Wangler, *RF Linear Accelerators, Second, Completely Revised and Expanded Edition.* John Wiley & Sons, 2008.

[8] Y. W. Kang, "Twisted waveguide accelerating structure," in *9th Workshop on Advanced Accelerator Concepts*, Aug. 2000.

[9] F. Marhauser, H.-W. Glock, P. Hulsmann, M. Kurz, and H. Klein, "Search for trapped modes in tesla cavities," in *Proceedings of the 1997 Particle Accelerator Conference*, vol. 1, May 1997, pp. 527–529.

[10] L. Lewin, *Theory of Waveguides.* London, Newness-Butherworths, 1975.

[11] H. Yabe and Y. Mushiake, "An analysis of a hybrid-mode in a twisted rectangular waveguide," *IEEE Transactions on Microwave Theory and Techniques*, vol. 32, no. 1, pp. 65–71, Jan. 1984.

[12] H. Yabe, K. Nishio, and Y. Mushiake, "Dispersion characteristics of twisted rectangular waveguides," *IEEE Transactions on Microwave Theory and Techniques*, vol. 32, no. 1, pp. 91–96, Jan. 1984.

[13] J. Stratton, *Electromagnetic Theory*. McGraw-Hill Book Company, Inc., 1941.

[14] P. Crepeau and P. McIsaac, "Consequences of symmetry in periodic structures," *Proceedings of the IEEE*, vol. 52, pp. 33–43, 1964.

[15] K. H. Flouds and J. R. Mansell, "Propagation of an electronic wave through a helical waveguide," *Proc of IEE*, vol. 3, no. 11, pp. 1789–1798, 1964.

[16] W. Wang, G. Yu, and Y. Wei, "Study of the ridge-loaded helical-groove slow-wave structure," *IEEE Transactions on Microwave Theory and Techniques*, vol. 45, no. 10, pp. 1689–1695, Oct. 1997.

[17] L. Hong-Tao, W. Yan-Yu, G. Yu-Bin, Y. Ling-Na, and W. Wen-Xiang, "Accurate analysis of arbitrarily-shaped helical groove waveguide," *Chinese Physics*, vol. 15, no. 9, pp. 2114–2119, Sep. 2006.

[18] D. Shyroki, "Exact equivalent straight waveguide model for bent and twisted waveguides," *IEEE Transactions on Microwave Theory and Techniques*, vol. 56, no. 2, pp. 414–419, 2008.

[19] A. Nicolet, F. Zolla, and S. Guenneau, "Modelling of twisted optical waveguides with edge elements," *European Physics Journal Applied Physics*, vol. 28, pp. 153–157, 2004.

[20] A. Nicolet, F. Zolla, Y. Agha, and S. Guenneau, "Leaky modes in twisted microstructured optical fibers," *Waves in Random and Complex Media*, vol. 17, no. 4, pp. 559–570, Nov. 2007.

[21] P. Harms, J. Lee, and R. Mittra, "A study of the nonorthogonal FDTD method versus the conventional FDTD technique for computing resonant frequencies of cylindrical cavities," *IEEE Transactions on Microwave Theory and Techniques*, vol. 40, no. 4, pp. 741–746, Apr. 1992.

[22] P. L. Khare, "Divergence and curl in nonorthogonal curvilinear coordinates," *American Journal of Physics*, vol. 38, no. 7, pp. 915–916, 1970.

[23] R. Holland, "Finite-difference solutions of Maxwell's equations in generalized nonorthogonal coordinates," *IEEE Transactions on Nuclear Science*, vol. 30, pp. 4589–4591, Dec. 1993.

[24] M. Fusco, "FDTD algorithm in curvilinear coordinates," *IEEE Transactions on Antennas and Propagation*, vol. 38, no. 1, pp. 76–89, Jan. 1990.

[25] Y. Liu, "Fourier analysis of numerical algorithms for the Maxwell equations," *Journal of Computational Physics*, vol. 124, no. 2, pp. 396–416, Mar. 1996.

[26] R. Janaswamy and Y. Liu, "An unstaggered colocated finite-difference scheme for solving time-domain Maxwell's equations in curvilinear coordinates," *IEEE Transactions on Antennas and Propagation*, vol. 45, no. 11, pp. 1584–1591, Nov. 1997.

[27] A. E. Fathy, C. Wang, J. Wilson, and S. Yang., "A fourth order difference scheme for the maxwell equations on yee grid," *Accepted for publication in Journal of Hyperbolic Differential Equations*, Sep. 2007.

[28] Y. Hao, V. Douvalis, and C. G. Parini, "Reduction of late time instabilities of the finite-difference time-domain method in curvilinear co-ordinates," in *Computation in Electromagnetics*, Apr. 8–11, 2002.

[29] Y. Hao and C. Railton, "Analyzing electromagnetic structures with curved boundaries on cartesian FDTD meshes," *IEEE Transactions on Microwave Theory and Techniques*, vol. 46, no. 1, pp. 82–88, Jan. 1998.

[30] R. Schuhmann and T. Weiland, "Stability of the FDTD algorithm on nonorthogonal grids related to the spatial interpolation scheme," *IEEE Transactions on Magnetics*, vol. 34, no. 5, pp. 2751–2754, Sep. 1998.

[31] P. Thoma and T. Weiland, "Numerical stability of finite difference time domain methods," *IEEE Transactions on Magnetics*, vol. 34, no. 5, pp. 2740–2743, Sep. 1998.

[32] T. Weiland, "Time domain electromagnetic field calculation with finite difference methods," *International Journal of Numerical Modelling*, vol. 9, pp. 295–319, 1996.

[33] P. Harms, R. Mittra, and W. Ko, "Implementation of the periodic boundary condition in the finite-difference time-domain algorithm for FSS structures," *IEEE Transactions on Antennas and Propagation*, vol. 42, no. 9, pp. 1317–1324, Sep. 1994.

[34] W. Ko and R. Mittra, "Implementation of floquet boundary condition in FDTD for FSS analysis," in *Antennas and Propagation Society International Symposium.*, vol. 1, Jun. 1993, pp. 14–17.

[35] S. Xiao, R. Vahldieck, and H. Jin, "Full-wave analysis of guided wave structures using a novel 2-D FDTD," *IEEE Microwave and Guided Wave Letters*, vol. 2, no. 5, pp. 165–167, May 1992.

[36] S. Xiao and R. Vahldieck, "An efficient 2-D FDTD algorithm using real variables," *IEEE Microwave and Guided Wave Letters*, vol. 3, no. 5, pp. 127–129, May 1993.

[37] M.-L. Lui and Z. Chen, "A direct computation of propagation constant using compact 2-D full-wave eigen-based finite-difference frequency domain technique," in *Proceedings of the 1999 International Conference on Computational Electromagnetics Applications*, 1999, pp. 78–81.

[38] Y.-J. Zhao, K.-L. Wu, and K.-K. M. Cheng, "A compact 2-D full-wave finite-difference frequency-domain method for general guided wave structures," *IEEE Transactions on Microwave Theory and Techniques*, vol. 50, pp. 1844–1848, Jul. 2002.

[39] L.-Y. Li and J.-F. Mao, "An improved compact 2-D finite-difference frequency-domain method for guided wave structures," *IEEE Microwave and Wireless Components Letters*, vol. 13, no. 12, pp. 520–522, Dec. 2003.

[40] C. S. Lavranos and G. A. Kyriacou, "A finite difference frequency domain study of curvature lifted modes degeneration," in *Progress in Electromagnetics Research Symposium*, Aug. 27–30, 2007, pp. 222–226.

[41] P. Barrera, G. Gonzalez, L. Castellanos, and A. Prez. (2008, May) Unamalla mesh generation package. [Online]. Available: http://www.mathmoo.unam.mx/unamalla

[42] *CST Microwave Studio 2006 Users Manual.* CST Ltd., Darmstadt, Germany.

[43] D. McDiarmid and G. Walker, "Two examples of "confluence" in periodic slow wave structures," *IEEE Transactions on Microwave Theory and Techniques*, vol. 16, no. 1, pp. 2–6, Jan. 1968.

[44] C. Rode, "The SNS superconducting linac system," in *Proceedings of the 2001 Particle Accelerator Conference*, vol. 1, Jun. 18–22, 2001, pp. 619–623.

[45] D. Goldberg and R. Rimmer, "Measurement and identification of HOMs in RF cavities," in *Proceedings of the 1997 Particle Accelerator Conference*, vol. 3, May 12–16, 1997, pp. 3001–3003.

[46] P. Matthews, T. Berenc, F. Schoenfeld, A. Feinerman, Y. Kang, and R. Kustom, "Electromagnetic field measurements on a millimeter wave linear accelerator," *IEEE Transactions on Microwave Theory and Techniques*, vol. 44, no. 8, pp. 1401–1409, Aug. 1996.

Appendices

Appendix A

Selected Relevant Publications

1. Joshua L. Wilson, Cheng Wang, Aly E. Fathy, and Yoon W. Kang. "Analysis of Rapidly Twisted Hollow Waveguides." *Accepted for publication in IEEE Transactions on Microwave Theory and Techniques. August, 2008. (included as Appendix B)*

2. Joshua Wilson, Cheng Wang, Songnan Yang, Aly E. Fathy, and Yoon W. Kang. "An Accurate and Stable Fourth Order Finite Difference Time Domain Method" *IEEE MTT-S International Microwave Symposium. Atlanta, 2008*

3. A. E. Fathy and C. Wang and J. Wilson and S. Yang. "A fourth order difference scheme for the Maxwell Equations on Yee grid." *Accepted for publication in Journal of Hyperbolic Differential Equations. Sep. 2007.*

4. Joshua L. Wilson, Yoon W. Kang, Cheng Wang, and Aly Fathy. "Numerical Simulation of Twisted Rectangular Waveguide Using Fully Nonorthogonal Finite Difference Computation." Proceedings of 2007 National Radio Science Meeting, Ottawa, Canada.

5. Y. Zhang, I. E. Campisi, C. Deibele, J. Galambos, S. Henderson, Y. W. Kang, H. Ma, J. L. Wilson. "SRF Cavity Transient Beam Loading Detection - Simulation and Measurement." Proceedings of PAC07, Albuquerque, New Mexico, USA.

Appendix B

Analysis of Rapidly Twisted Hollow Waveguides: Submitted to MTT Transactions

Analysis of Rapidly Twisted Hollow Waveguides

Joshua L. Wilson, *Student Member, IEEE,* Cheng Wang, Aly E. Fathy, *Fellow, IEEE,*
and Yoon W. Kang, *Senior Member, IEEE*

***Abstract*—The propagation characteristics of twisted hollow waveguides are considered, and various analysis methods are proposed. It is shown that a twisted hollow waveguide can support waves that travel at a speed slower than the speed of light c. These modes are of particular interest, as slow-wave structures have many potential applications in accelerators and electron traveling wave tubes. Since there is no exact closed form solution for the electromagnetic fields within a twisted waveguide or cavity, several previously proposed approximate methods are examined. It is found that the existing perturbation theory methods yield adequate results for slowly twisted structures; however, our efforts here are geared toward analyzing rapidly twisted structures using newly developed finite difference methods. To validate the results of the theory and simulations, rapidly twisted cavity prototypes have been designed, fabricated and measured. These measurement results are compared to simulated results, and very good agreement has been demonstrated.**

I. Introduction

IT is a well known fact that straight hollow waveguides with a uniform cross section will only support modes whose phase velocity is greater than c. At the same time, many useful microwave devices depend on the interaction of charged particles with an electromagnetic wave. This is one reason why there has been interest in slow-wave electromagnetic structures, which support waves traveling at speeds slower than c.

We consider a twisted waveguide, formed by extruding any cross section along a straight line while twisting. Such a waveguide is unique in that, like a straight guide, the cross section is uniform along the axis of the guide, yet unlike a straight guide, it has the capacity to support both slow and fast modes. As a result, twisted or helical structures have been considered for their application in traveling wave tubes and particle accelerators [1], [2]. Such twisted structures could potentially be easier to manufacture than other types of slow-wave structures (such as dielectric loaded structures).

Analysis of twisted rectangular waveguides has been carried out before by Lewin [3] and by Yabe, Mushiake, and Nishio [4], [5]. In each of these papers, perturbation theory is used to analyze the propagation characteristics of the dominant quasi-TE mode in the waveguide. The perturbation theory approach is very well suited for analyzing the dominant TE mode in infinite twisted guides with small twist rates. However, this model is not well-suited for rapidly twisted waveguides. This is because perturbation theory assumes

$$k^2 - \beta^2 = \frac{\pi^2}{a^2}\left(1 + \alpha_1 p + \alpha_2 p^2 + \cdots\right), \qquad (1)$$

Joshua Wilson, Cheng Wang, and Aly E. Fathy are with the University of Tennessee at Knoxville

Yoon Kang is with the Spallation Neutron Source (SNS) at Oak Ridge National Laboratory

for some twist rate p, where all higher terms past order p^2 are dropped from the expansion. In this paper, when we speak of "slow twist rates", we refer to those cases where perturbation theory is valid, generally meaning that the product of the twist rate and the largest cross sectional dimension is less than 1.

At high twist rates, then, it becomes necessary to look beyond perturbation methods to arrive at the correct solution. In many cases, the case of rapid twist rate is of more interest in slow-wave applications, since rapidly twisted guides can produce more slowing of the electromagnetic wave. Also, the perturbation theory approach cannot take end effects into account in a twisted cavity of finite length. This could lead to errors in the calculation of the fields near the end walls of the cavity.

Therefore, it is imperative to develop new methods to analyze rapidly twisted guides. For example, it has been recently pointed out by Shyroki [6] that there exists an exact equivalent for twisted and bent waveguide structures, based on the coordinate transformation properties discussed by Nicolet, Zolla, Agha, and Guenneau [7], [8]. Working independently of Shyroki, the authors have developed similar techniques to address this problem, and this method has been extended to include arbitrary cross sections without the need for a staircase-type mesh. We also introduce a new stable two-dimensional nonorthogonal finite difference time domain method for solving twisted guides and present experimental verification of the results.

In this paper, we will present an overview and a mathematical description of helical geometries. From there, a coordinate transform is applied to derive three numerical methods for the solution of twisted guides: a three dimensional time domain method for simulation of twisted cavities of finite length, a two dimensional time domain method for efficient, simultaneous simulation of multiple modes in an infinite twisted structure, and a two-dimensional frequency domain method for individual eigenmode calculations. It is shown how these methods can be used to easily solve twisted guides of arbitrary cross section. Finally, experimental data are presented and compared to our methods and the predictions of perturbation theory.

II. Overview of Twisted Structures

Twisted structures are a special case of the more general class of periodic structures. However, twisted waveguides and cavities possess certain additional properties which are not true of other periodic structures, such as disk-loaded waveguides or other periodically loaded straight guides. These properties allow the transformation of the twisted structure into an equivalent straight structure with uniform cross section. The essence of the transformation is to replace the twisted (or bent) empty

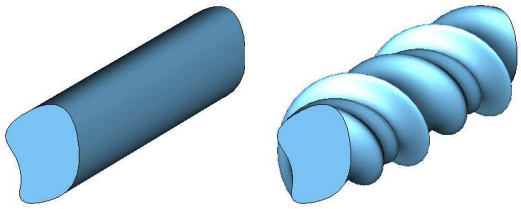

Fig. 1. A straight equivalent (left) to an arbitrary uniformly twisted waveguide (right).

waveguide with a straight waveguide whose cross section is the same, but whose volume is filled with a nonuniform anisotropic material [6]. The fact that the equivalent guide is straight greatly simplifies the implementation of boundary conditions. Also, for uniformly twisted structures, it can be shown that the anisotropic permeability and permittivity do not involve the z coordinate. This allows much of the same machinery previously used to solve two-dimensional propagation problems to be brought to bear on twisted waveguide problems.

A. Defining a Twisted Geometry

Let us assume that we have a 2D cross section defined by some implicit function of x and y. An arbitrary straight cavity can be constructed by specifying a volume

$$\begin{aligned} f(x,y) &< \delta \\ z_{min} < z &< z_{max}, \end{aligned} \tag{2}$$

for some constant δ. It is assumed that the boundaries of the structure are perfectly conducting walls.

Now, we introduce the twisted (or helicoidal) coordinate transform employed by Lewin [3].

$$\begin{aligned} x' &= x\cos pz + y\sin pz \\ y' &= y\cos pz - x\sin pz \\ z' &= z \end{aligned} \tag{3}$$

Here, p is some constant twist rate, usually expressed in radians per meter, or $\frac{R}{m}$. A twisted cavity can now be defined simply by

$$\begin{aligned} f(x',y') &< \delta \\ z_{min} < z' &< z_{max}. \end{aligned} \tag{4}$$

It should be noted that the transverse cross section of such a helical waveguide or cavity (i.e. cut across a $z = constant$ boundary) will always yield the same shape, although rotated about the line $x = 0, y = 0$. In this sense, the structure has a uniform cross section. Fig. 1 shows an arbitrary twisted waveguide, and its corresponding straight equivalent after applying the coordinate transformation. We will first focus on twisted waveguides and cavities of rectangular cross section, and later extend the theory to arbitrary cross sections.

B. Twisted Coordinate System

As discussed in [4], the coordinate transformation (3) is not orthogonal. Its analysis will require the covariant and contravariant basis vectors to be defined. In keeping with the conventional notation of differential geometry, we will sometimes refer to the coordinate x' as x^1, y' as x^2, and z' as x^3. The corresponding contravariant basis vectors will be denoted as $\boldsymbol{e_1}$, $\boldsymbol{e_2}$, and $\boldsymbol{e_3}$, and the covariant vectors as $\boldsymbol{e^1}$, $\boldsymbol{e^2}$, and $\boldsymbol{e^3}$. Following the usual convention, superscripts are used to refer to contravariant quantities, whereas subscripts are used to refer to covariant quantities. Since the coordinate system of interest is nonorthogonal, there should be no expectation that $\boldsymbol{e_i} \cdot \boldsymbol{e_j} = \delta_{ij}$. Instead, the covariant metric tensor must be defined

$$g_{ij} = \boldsymbol{e_i} \cdot \boldsymbol{e_j}. \tag{5}$$

For the twisted coordinate system of (3), it can be shown from basic differential geometry that

$$[g_{ij}] = \begin{bmatrix} 1 & 0 & -py' \\ 0 & 1 & px' \\ -py' & px' & p^2(x'^2 + y'^2) + 1 \end{bmatrix}, \tag{6}$$

from which we note that z', the transformed longitudinal coordinate, does not appear in the metric tensor. Note that as p tends to 0, $[g_{ij}]$ becomes the identity matrix, which is expected since in this case, the original Cartesian coordinate system is recovered. Following Nicolet and Shyroki [7], [8], [6], we define a straight equivalent waveguide by loading with a nonuniform material dictated by the metric tensor.

$$\begin{aligned} \mu^{ij} &= \mu_0 g^{ij}\sqrt{g} \\ \epsilon^{ij} &= \epsilon_0 g^{ij}\sqrt{g}, \end{aligned} \tag{7}$$

Here, g is the determinant of the metric tensor. Also, g^{ij} is the contravariant metric tensor, which is related to (6) by an inverse relationship:

$$[g_{ij}]^{-1} = \left[g^{ij}\right]. \tag{8}$$

In this way, the problem becomes one of solving Maxwell's equations in ordinary Cartesian coordinates in a non-twisted structure, but subject to an anisotropic and nonuniform permittivity and permeability. For (6), the value of g turns out to be one, which can often be used to simplify many expressions involving the material loading.

In the transformed (straight waveguide) problem, the components (E_x, E_y, E_z) and (H_x, H_y, H_z) are equal to the covariant components (E_1, E_2, E_3) and (H_1, H_2, H_3) in the physical problem. Note that this permittivity and permeability vary with position, but do not involve z', the transformed longitudinal coordinate. Assuming the fields can be solved in this manner, the results can be converted back into Cartesian coordinates by multiplying the appropriate Jacobian. For a detailed discussion of the mathematical foundations of the "equivalent waveguide" concept, the reader is directed to the works of Nicolet, Shyroki, and Chandezon [7], [8], [6], [9]. (Ward and Pendry [10] also made use of a similar transformation to simplify calculation of photonic Green's functions.)

III. Three Dimensional Finite-Difference Time Domain Analysis

In this section, we will apply the transformation discussed in the previous section to devolop a three dimensional finite-difference time domain solver. The ability to transform a twisted structure into a straight rectangular domain indicates that a finite difference technique over a structured grid is well-suited to solve the problem, since the boundary conditions can be very simple. We developed an accurate and stable method that could be used for twisted guides. Unfortunately, a standard implementation of the finite-difference time domain (FDTD) technique is impossible here because, for example, in order to calculate $\boldsymbol{E}$ at any point, it is necessary to know all three components of $\boldsymbol{D}$ at that point due to the material anisotropy. In a staggered mesh this is very difficult. However, Holland [11] proposed a remedy for this situation by spatially interpolating the necessary field components. Unfortunately, this approach was found to have late-time instability problems. Schuhmann and Weiland [12] showed that this problem was due to the asymmetric evaluation of the metric tensor matrix. Their solution was to retain the spatial interpolation, but change the way the metric tensor was evaluated.

Around the same time, Thoma and Weiland [13] offered a mathematical proof for the stability of the spatial discretization method for a domain loaded with anisotropic material. Assume that the field vectors have been vectorized, and the curl operators have been appropriately discretized, leading to the well-known Maxwell Grid Equations (MGE's) used in the finite-integration technique [14]:

$$\begin{aligned} C\boldsymbol{e} &= -\dot{\boldsymbol{b}} \\ C^T\boldsymbol{h} &= -\dot{\boldsymbol{d}}, \end{aligned} \tag{9}$$

where $\boldsymbol{d}$, $\boldsymbol{e}$, $\boldsymbol{b}$, and $\boldsymbol{h}$ are the discrete vectorized representations of the fields. As mentioned in [13], the fact that the curl operator acting on the electric field is the transpose of the curl operator acting on the magnetic field is essential to the demonstration of stability. The corresponding discrete material relations are

$$\begin{aligned} \boldsymbol{d} &= D_\epsilon \boldsymbol{e} \\ \boldsymbol{b} &= D_\mu \boldsymbol{h}, \end{aligned} \tag{10}$$

where D_ϵ and D_μ are matrix operators corresponding to the discretized permittivity and permeability of the material, respectively. It was shown [13] that the spatial discretization scheme is stable if the curl operators were related by a transpose as in (9) (as mentioned earlier), and the material operators were symmetric. The late-time stability of the scheme was demonstrated theoretically (and numerically) by proving non-increasing total field energy.

An alternative to this approach is to use the nonuniform, unstaggered mesh developed by Liu and Janaswamy [15], [16]. Forward differences are employed for the electric field, while backward differences are employed for the magnetic field. For a classic second order scheme,

$$\begin{aligned} \frac{dE_i}{dx_j} &= \frac{E_i(x_j+h) - E_i(x_j)}{h} \\ \frac{dH_i}{dx_j} &= \frac{H_i(x_j) - H_i(x_j-h)}{h} \end{aligned} \tag{11}$$

Liu [15] demonstrated that the dissipative errors from the forward and backward difference operators cancel each other out in such a way that the resulting wave operator is accurate to second order and has no dissipative error. It is easily demonstrated that for this mesh structure, the material operators are symmetric if the metric tensor is symmetric at every point, which is guaranteed from the definition of the metric tensor. However, a challenge presents itself around a perfectly conducting boundary, since enforcing the transpose condition on the curl operators is nontrivial. This condition requires, for example, that if the computation of $(\nabla \times \boldsymbol{E})_x (i,j,k)$ involves a term $mE_y(i,j,k+1)$ for some constant m, then the computation of $(\nabla \times \boldsymbol{H})_y (i,j,k+1)$ must have a term $mH_x(i,j,k)$. For interior points, where (11) applies, this condition is satisfied automatically. Near a perfectly conducting boundary, the computation of $\nabla \times \boldsymbol{H}$ is typically altered to enforce the boundary condition on the electric field. If a perfectly conducting boundary exists at $i = N_x$,

$$\begin{aligned} &(\nabla \times \boldsymbol{E})_y (N_x - 1, j, k) \\ &= \frac{E_x(N_x-1,j,k+1) - E_x(N_x-1,j,k)}{\Delta z} \\ &- \frac{0 - E_z(N_x-1,j,k)}{\Delta x}, \\ &(\nabla \times \boldsymbol{H})_z (N_x, j, k) \\ &= \frac{H_y(N_x,j,k+1) - H_y(N_x-1,j,k)}{\Delta x} \\ &- \frac{H_x(N_x,j,k) - H_x(N_x,j-1,k)}{\Delta y}. \end{aligned} \tag{12}$$

Since $(\nabla \times \boldsymbol{H})_z (N_x, j, k)$ involves a term $-\frac{H_y(N_x-1,j,k)}{\Delta x}$ but $(\nabla \times \boldsymbol{E})_y (N_x - 1, j, k)$ does not have a $-\frac{E_z(N_x,j,k)}{\Delta x}$ term, the transpose condition is not satisfied, and there is no guarantee of stability around the boundary. Clearly, another method for enforcing the boundary conditions must be implemented. To do this, a careful examination of the boundary condition is necessary around a conducting boundary, namely

$$(\nabla \times \boldsymbol{H})_x = \frac{dD_x}{dt} = \epsilon^{1j}\frac{dE_j}{dt} = \epsilon^{11}\frac{dE_x}{dt}, \tag{13}$$

for an $x = constant$ boundary, leading to the updating formula

$$\frac{dE_x}{dt} = \frac{1}{\epsilon^{11}}(\nabla \times \boldsymbol{H})_x = \frac{1}{\epsilon_0\sqrt{g}g^{11}}(\nabla \times \boldsymbol{H})_x. \tag{14}$$

Using this relation, the material parameters can be modified along the boundary:

$$[\epsilon]^{-1} = \begin{bmatrix} \frac{1}{\epsilon_0\sqrt{g}g^{11}} & 0 & 0 \\ 0 & 0 & 0 \\ 0 & 0 & 0 \end{bmatrix}. \tag{15}$$

Since the covariant components g_{ij} are normally computed at each mesh point, we can express g^{11} by calculating the $(1,1)$

component of $[g_{ij}]^{-1}$ and simplifying by making use of the symmetry of the metric tensor.

$$[\epsilon]^{-1} = \begin{bmatrix} \frac{1}{\epsilon_0\sqrt{g}}\left(g_{11} + \frac{g_{21}^2 g_{33} + g_{31}^2 g_{22} - 2g_{21}g_{31}g_{23}}{g_{32}^2 - g_{22}g_{33}}\right) & 0 & 0 \\ 0 & 0 & 0 \\ 0 & 0 & 0 \end{bmatrix}. \tag{16}$$

In practice, a very small number is used for the zero elements of this matrix in order to ensure that the material operator D_ϵ^{-1} remains invertible. Now, since the boundary condition around the boundary is satisfied implicitly, the expression for the curl of $\boldsymbol{E}$ around the boundary can be

$$\begin{aligned} &(\nabla \times \boldsymbol{E})_y (N_x - 1, j, k) \\ &= \frac{E_x(N_x - 1, j, k+1) - E_x(N_x - 1, j, k)}{\Delta z} \\ &- \frac{E_z(N_x, j, k) - E_z(N_x - 1, j, k)}{\Delta x}, \end{aligned} \tag{17}$$

satisfying the transpose condition and ensuring stability. This modification of the material parameters around a conducting boundary in an unstaggered collocated nonorthogonal FDTD scheme to ensure stability is novel to this approach, and has not been done by others.

With the material matrices derived in this fashion and using the normal cartesian curl operators, the grid equations of (9) can be updated at each time step using an appropriate time integrator (such as leap frog for a second order scheme). The result is a scheme rather similar to the nonorthogonal FDTD method [11], but not subject to the troubling late-time instability phenomena. The Courant stability criteria for the time step cannot be expressed by a simple formula, as was the case for rectangular grids. However, an upper bound can be set using formulas given in [17]. The authors have designed both second order schemes (employing classic second order spatial differences and leap frog time integration) and fourth order schemes (employing a fourth order spatial difference operator and RK4 based time integration). In both cases, stable and efficient operation has been achieved.

To check the late-time numerical stability, the total cavity energy was computed over time for a simulation of a twisted rectangular cavity (the one discussed later in this paper). The results can be shown in Fig. 2 for up to 8×10^6 time steps. Although the total energy can be seen to fluctuate over time, no late-time instability has ever been observed with this technique, either with a second or a fourth order implementation. The energy fluctuations are due to the inherent error of the time integrator, as evidenced by the fact that the fluctuations can be reduced arbitrarily by decreasing the time step and/or using a higher order integrator such as RK4.

The three dimensional solver is excellent for solving twisted cavities of finite length. However, for solving infinite twisted guides (or even very long twisted cavities where end effects can be neglected), the algorithm can be made much more efficient by using a two dimensional mesh, rather than a three dimensional one.

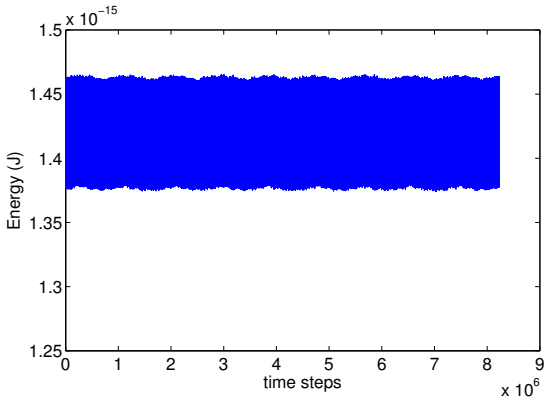

Fig. 2. Cavity energy versus time showing late time stability of the proposed 3D scheme.

IV. Two Dimensional Finite-Difference Analysis

As mentioned previously, the twisted structure is a specific type of periodic structure, so it is natural to turn to solvers that use periodic boundary conditions. However, for the twisted guide, the algorithm can be simplified much further, since the period can essentially be reduced to zero if the appropriate coordinate system is chosen, giving a 2D mesh in the limiting case.

A 2D finite element solver for TE modes in twisted waveguides was proposed by Igarashi and Honma [18]. This solver works well for slowly twisted guides, where the modes can still be regarded as basically TE or TM independently. Strictly speaking, however, TE and TM modes do not exist in a twisted waveguide (as shown by Yabe and Mushiake [4]). A hybrid mode is needed to satisfy the boundary conditions, and this becomes particularly critical as the twist rate becomes relatively large and there is significant deviation from the straight waveguide case. Therefore, we applied finite difference techniques to the straight waveguide equivalent problem. (A finite element approach also using the straight equivalent can be found in [19].)

A 2D FDTD algorithm for the efficient solution of straight waveguide propagation problems was proposed by Xiao and Vahldieck [20]. This should not be confused with the conventional 2D FDTD method where the fields are assumed to be uniform in one direction. Here, the idea is to assume a complex solution of the form

$$\begin{aligned} \boldsymbol{E} &= \boldsymbol{E_1}(x, y, t)e^{-j\beta z} \\ \boldsymbol{H} &= \boldsymbol{H_1}(x, y, t)e^{-j\beta z}. \end{aligned} \tag{18}$$

Here, we are solving only one traveling wave mode solution of the twisted guide problem at a time. Any such modes can exist independently, since they perfectly satisfy the boundary conditions. Instead of the z derivatives being calculated in the conventional sense using finite differences, they are calculated by multiplying that field component by $-j\beta$. In this manner, the quantities $\boldsymbol{E_1}$ and $\boldsymbol{H_1}$ can be updated using a time integrator. Although this means that the computations will

now involve complex quantities rather than the purely real computations of the classical FDTD method, the mesh can be reduced from three dimensions to two. A simple uniform mesh can be used if the material properties are modified around the conducting boundary surface, as discussed above.

A. Time Domain Implementation

Assuming field solutions of the form (18), a time domain solver can easily be derived using the same uniform mesh concept employed for the 3D case, but reduced to two dimensions. The real time-domain fields at any point (x, y, z) in the equivalent straight structure can be recovered from the complex solution using

$$\begin{aligned} \boldsymbol{E}(x,y,z,t) &= \Re\{\boldsymbol{E_1}(x,y,t)e^{-j\beta z}\} \\ \boldsymbol{H}(x,y,z,t) &= \Re\{\boldsymbol{H_1}(x,y,t)e^{-j\beta z}\}. \end{aligned} \tag{19}$$

$\Re\{\}$ represents the real part. The value of β is a running variable from 0 to ∞. Each value of β will result in a number of modes with different frequencies. This technique allows dispersion curves to be obtained efficiently for a large number of modes. We do this by running a number of simulations while sweeping the value of β. A multimode initial condition is used, and an FFT is performed on the output fields of each simulation to obtain the frequencies of the modes.

A sample spectrum obtained by two dimensional time domain analysis of a twisted rectangular waveguide is shown in Fig. 3. As previously mentioned, a mixed-mode initial condition was purposefully chosen to produce a broad spectrum of excited modes. Like the three dimensional method we developed, there was no late-time instability observed in the results produced by this method. The mode with the lowest frequency is the dominant TE-like mode that is investigated experimentally later in this paper.

We demonstrated that a two dimensional time-domain method can be used to solve for the fields and the frequencies of many modes in a rapidly twisted structure over a wide range of frequencies simultaneously. However, the time-domain solver is not capable of directly extracting the eigenmodes of the twisted waveguide, so we also discuss an implementation in the frequency domain.

B. Frequency Domain Implementation

The Finite Difference Frequency Domain method has been discussed by Lui and Chen [21]. In it, the fields are assumed to be harmonic in time and in the z direction, so the explicit time updating scheme of the FDTD method is eliminated completely and replaced by an eigenvalue problem. In it, all six field components are solved for directly. Later, it was found that the number of actual solved field components and the number of nonzero matrix elements could be reduced significantly [22], [23]. The solution of curved waveguides using 2D FDFD has previously been attempted by Lavranos and Kyriacou [24]. However, their formulation depended on an orthogonal coordinate system and the ability to separate the field into axial and transverse components, which was mentioned in [24] to be invalid for high curvature rates (or small curvature radii). Thus, the extension of their work to rapidly twisted waveguides is problematic.

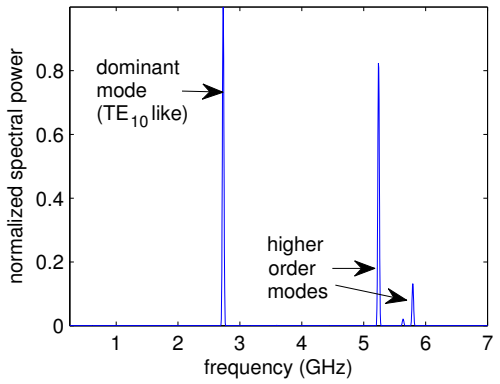

Fig. 3. Sample spectrum obtained by 2D time domain simulation of a twisted rectangular guide.

By contrast, this research proposes to solve the twisted structure in nonorthogonal coordinates which is based on an exact equivalent, and does not make any simplifying assumptions that would be invalid for high twist rates. To use this method to solve the Maxwell equations for a twisted waveguide structure, the vector Helmholtz equation in general curvilinear coordinates is derived. Using the anisotropic equivalent structure and solving the transformed problem in Cartesian coordinates, the Maxwell curl equations become

$$\frac{1}{\sqrt{g}}[g_{ij}]\nabla \times \boldsymbol{E} = -j\omega\mu_0\boldsymbol{H} \tag{20}$$

$$\frac{1}{\sqrt{g}}[g_{ij}]\nabla \times \boldsymbol{H} = j\omega\epsilon_0\boldsymbol{E}, \tag{21}$$

which leads to the eigensystem

$$\frac{1}{\sqrt{g}}[g_{ij}]\nabla \times \left(\frac{1}{\sqrt{g}}[g_{ij}]\nabla \times \boldsymbol{E}\right) = k_0^2\boldsymbol{E}. \tag{22}$$

In this scheme, three vector components have to be computed at each grid point. For example, if a 20 by 20 grid was employed to solve a twisted square waveguide, the dimension of the system would be $20 \times 20 \times 3 = 1200$, and the total number of matrix elements would be $1200^2 = 1.44 \times 10^6$. Fortunately, the use of finite differences assures us that the matrix will likely be sparse. If the sparsity of the matrix is taken into account, it can drastically reduce memory and calculation time. If the field components are vectorized as in the Maxwell Grid Equations, the same matrix operators can be used to calculate both the frequency and time domain solutions. It is difficult to give a definitive rule regarding how many mesh points are needed for a good simulation. In general, it will depend greatly on the judicious choice of a structured mesh. In practice, one should run several cases with varying degrees of mesh refinement to determine when convergence has been achieved.

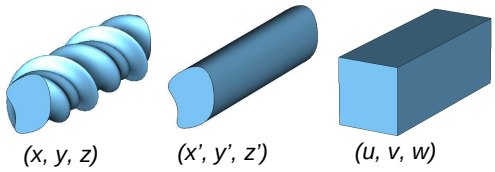

Fig. 4. Cascaded coordinate transformation used to analyze arbitrary twisted structures.

V. Twisted Guides of Arbitrary Cross Section

Thus far, we have only considered twisted waveguides of rectangular cross section. Fortunately, our choice of a twisted coordinate system allows a simple cascaded coordinate transform that permits a solution to arbitrary twisted guides. The coordinate transform of (3) is combined with a planar transform

$$\begin{aligned} x' &= x'(u,v) \\ y' &= y'(u,v) \\ z' &= w. \end{aligned} \tag{23}$$

The coordinates (u, v, w) are arranged in a cartesian grid. This cascaded transform is illustrated in Fig. 4. The functions u and v can be derived using finite differences from any commercial or freeware software package capable of generating 2D structured planar meshes. The authors have made use of a free utility called UNAMALLA to generate such meshes [25]. The covariant metric tensor for this cascaded transform can be obtained using the rule

$$(g_{ij})_u = (g_{mn})_{x'} \frac{\partial x'^m}{\partial u^i} \frac{\partial x'^n}{\partial u^j}. \tag{24}$$

Here, $(g_{mn})_{x'}$ is the metric tensor for the transform from cartesian coordinates to the primed coordinates (in this case, (3)), and the labels u^i correspond to (u, v, w). Under this transformation,

$$[g_{ij}] = \tag{25}$$
$$\begin{bmatrix} x'^2_u + y'^2_u & x'_u x'_v + y'_u y'_v & px'y'_u - py'x'_u \\ x'_u x'_v + y'_u y'_v & x'^2_v + y'^2_v & px'y'_v - py'x'_v \\ px'y'_u - py'x'_u & px'y'_v - py'x'_v & 1 + p^2(x'^2 + y'^2) \end{bmatrix}.$$

Also, note again that the longitudinal coordinate does not appear in the metric tensor, allowing two dimensional methods to be used. Since typical mesh generation programs output the coordinates of each point on the grid, x' and y' are known at each mesh point. The derivatives x'_u, x'_v, y'_u, and y'_v are calculated using finite differences. From here, the relations of (7) can be used to calculate the material properties of the transformed guide.

One particular case of interest in slow wave applications is the twisted "keyhole" structure, whose longitudinal cross section is identical to a disk loaded waveguide. The cross section, along with the generated UNAMALLA mesh, is shown in Fig. 5. This twisted structure is similar to the "helical groove waveguide" discussed by Flouds and Mansell [26] which has application in traveling wave tubes. (In fact, the present theory also provides a method for accurately solving that structure as well.)

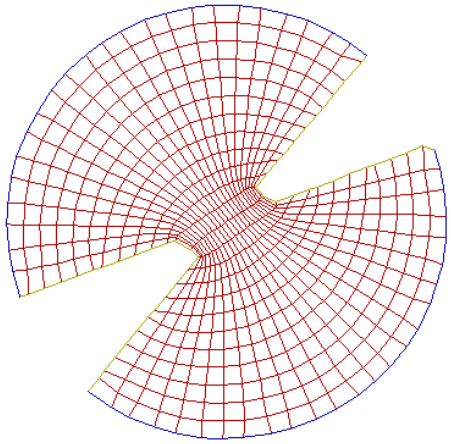

Fig. 5. Keyhole cross section and corresponding mesh.

VI. Comparison and Discussion

In this section, an example twisted rectangular waveguide is considered. The waveguide has cross-sectional dimensions of 8.16 cm by 3.63 cm. We will use this case to discuss the results of the present numerical methods in light of the findings of Lewin, Yabe, Nishio, and Mushiake. To determine at what value of twist rate there is significant deviation, we calculate the expressions given in [5] for Lewin's theory and that presented by Yabe *et. al.* The cutoff frequencies predicted by these two perturbation methods are compared to the results of the developed two dimensional finite difference frequency domain method, employing a 50 by 50 grid. The finite difference calculation was done using MATLAB on a 1.86 GHz Intel(R) Core(TM)2 CPU. Calculating the first five eigenmodes took 14 seconds and used roughly 55MB of memory. The comparison to perturbation theory is shown in Fig. 6.

For low values of twist rate, all three theories are found to be in excellent agreement. As the twist rate increases, however, the results of Lewin begin to be less accurate than those of Yabe *et. al.*. This is because Lewin formulated his theory assuming simple TE waveguide modes, whereas the more accurate theory presented by Yabe *et. al.* assumes a hybrid mode which satisfies the boundary conditions of the twisted guide. Measurement results were given in [5], and these showed good experimental agreement at low twist rates. If the waveguide structures measured in Yabe's paper are scaled up to the same physical size as the waveguides investigated here, the twist rates are all below $13\frac{R}{m}$. Fig. 6 shows that at this twist rate, the theory of [5] is still in close agreement with the finite difference method presented here.

However, as the twist rate becomes even more rapid, all perturbation methods appear to be inadequate. This phenomenon explains the drastic difference between the perturbation theory

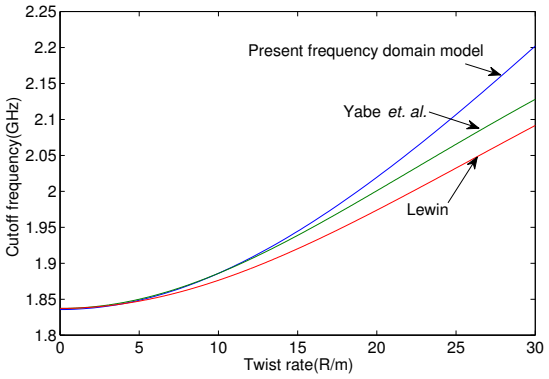

Fig. 6. Cutoff frequencies predicted for 8.16 cm by 3.63 cm rectangular waveguide.

predictions and our measured results for the rapidly twisted rectangular cavity. This result is to be expected, since perturbation theory neglects higher order correction terms for rapid twists. In order to verify the accuracy of the methods applied to rapidly twisted structures, it becomes necessary to turn to commercial software (such as HFSS or CST) or experimental validation.

VII. Experimental Verification

To validate the developed three dimensional finite difference method, a twisted rectangular cavity prototype with the same cross sectional dimensions as in the previous section was designed to work near 2.8 GHz. The cavity has two complete twists over a length of 22.7 cm. For this case ($p = 55.4\frac{R}{m}$), Fig. 6 shows that perturbation methods clearly will not suffice. The prototype was printed using an SLA (Stereolithography Apparatus) technique and then copper plated on the inside. This method can allow the rectangular cross section to be accurately preserved even for large twist rates. Fig. 7 shows the completed prototype. This particular prototype was selected because of its moderately high twist rate, enabling the accuracy of the newly proposed methods to be compared with the existing perturbation theory method.

Measurements were taken on this prototype by placing a copper plate on each end of the waveguide, effectively turning it into a resonant cavity. Two small probes were inserted in the end plates, and a vector network analyzer was used to measure the transmission coefficient S_{21} over a wide range of frequencies. The maxima of $|S_{21}|$ correspond to the resonant modes of the cavity structure. Fig. 8 shows S_{21} over the range of frequencies spanning the first four TE-like modes of the resonant cavity. The frequencies and Q values for these modes are shown in Table I.

Since the cavity is rather electrically short, end effects were found to limit the effectiveness of the two dimensional code for this case. A straight rectangular waveguide can be converted into a cavity by introducing shorting plates without affecting the eigenmodes (since the tangential electric field of TE modes in the waveguide naturally vanishes each half

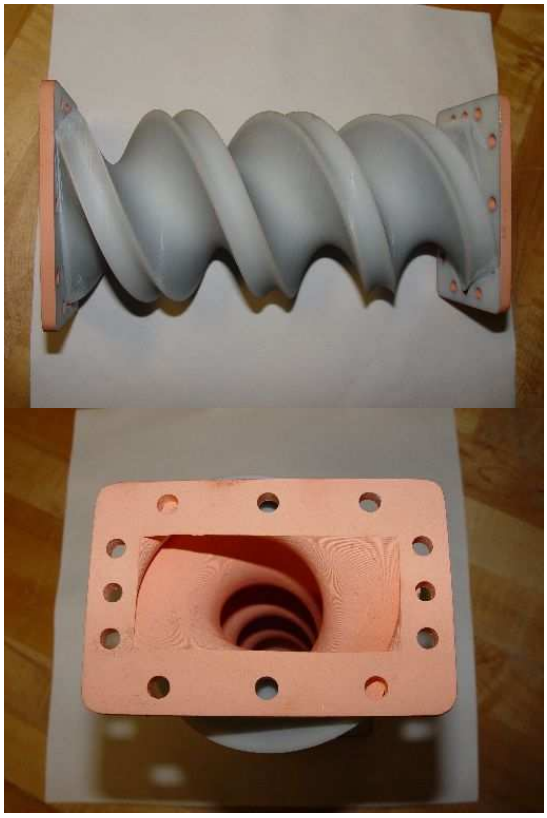

Fig. 7. Twisted rectangular waveguide prototype.

cycle). Unfortunately the same cannot be said of a twisted rectangular guide, so some perturbation in the mode will be introduced by the metal wall.

An 18 X 8 X 50 grid was employed for the 3D solver, and the simulation was allowed to run to 50 ns. The phase constant was selected by establishing an initial condition that contained a particular number of half-cycle variations in the longitudinal direction. The frequency of the resonant mode was then obtained through the use of an FFT. These frequencies were then compared to the measured frequencies and found to be within 0.5% of each other. By comparison, the error using the perturbation theory equations given by Yabe, Mushiake, and Nishio in [5] was more than 8% for each of the modes.

For the 2D method, using a 72 X 32 2D mesh, the code yielded up to 1.8% frequency deviation from experiment. Again, the 2D code solves the structure as if it were infinite. Therefore, to further validate the effectiveness of the 2D code, another prototype was constructed that was identical to the first, except twice as long, now with 4 complete twists. The measurement results for the short and long cavities as well as the 2D NFDTD and 2D NFDFD results are shown in Table II.

The trend in the experimental results of Table II indicates

TABLE I
EXPERIMENTALLY MEASURED FIRST FOUR TE-LIKE MODES FOR THE SHORT TWISTED RECTANGULAR PROTOTYPE COMPARED TO 3D SIMULATION RESULTS.

	Measured frequency	**Q**	Simulation Frequency (3D FDTD)	Deviation from Experiment
Mode 1	2.747 GHz	7001	2.734 GHz	0.47%
Mode 2	2.820 GHz	3977	2.808 GHz	0.43%
Mode 3	2.947 GHz	1921	2.940 GHz	0.24%
Mode 4	3.139 GHz	1003	3.135 GHz	0.13%

TABLE II
SHORT AND LONG PROTOTYPE RESONANT FREQUENCIES COMPARED TO 2D SIMULATION METHOD RESULTS.

Short Prototype Frequency	**Long Prototype Frequency**	2DNFDTD	2DNFDFD
2.747 GHz	2.743 GHz	2.734 GHz	2.735 GHz
2.820 GHz	2.808 GHz	2.794 GHz	2.794 GHz
2.947 GHz	2.932 GHz	2.907 GHz	2.906 GHz
3.139 GHz	3.119 GHz	3.083 GHz	3.082 GHz

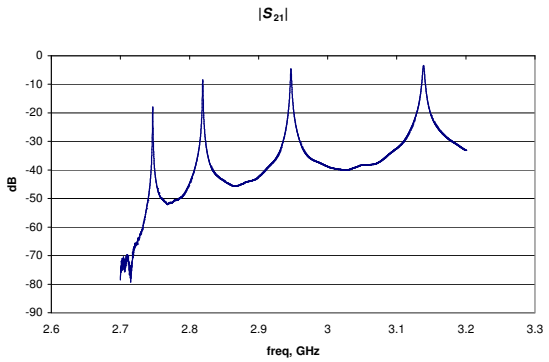

Fig. 8. Measured $|S_{21}|$ for the short twisted rectangular prototype showing resonances.

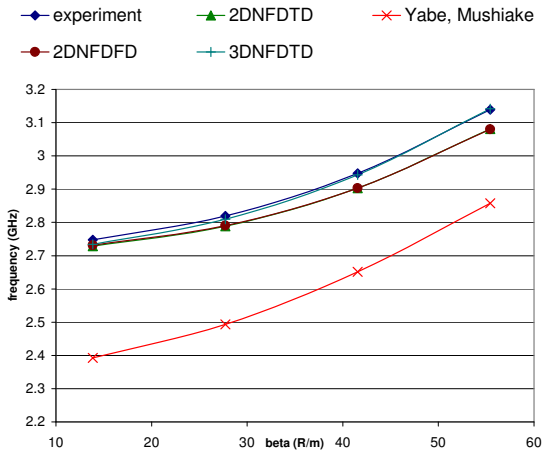

Fig. 9. Dispersion curves showing measured and predicted resonant frequencies for twisted rectangular cavity. (beta is the phase constant.)

that as the cavity gets physically longer, the measured resonant frequency approaches the predictions of the 2D methods, as expected. In the limiting case of an infinite structure, end effects should become negligible, and it is expected that the 2D method will perform quite well.

The experimental cavity results were used to generate dispersion curves. These are compared to the various simulation methods we developed in Fig. 9.

To test the two-dimensional methods for twisted guides of arbitrary cross section, a keyhole cross section was defined in the transverse plane, as in Fig. 5. Since this structure has potential application for particle acceleration purposes, a TM mode near 2.8 GHz was chosen for analysis. A prototype was constructed with three complete twists over a length of 21 cm. This particular design was chosen so that the phase velocity of the wave would be exactly c, which is necessary for most electron accelerators and traveling wave tubes in which particles move at relativistic velocities extremely close to the speed of light. The measured frequency was 2.8135 GHz. For a 25 by 25 grid, the 2D frequency domain method yielded a resonant frequency of 2.8159 GHz while the 2D time domain method gave 2.8158 GHz. The fact that the measured results are very close to prediction indicates that for this TM mode, the perturbations caused by the end walls are small (at least for that value of twist rate).

In order to ensure that the mode measured was indeed the mode predicted by the model, the phase constant was measured and compared with the β value used in the simulation. Here, the mode of interest has two complete cycles over the length of the cavity for an expected $\beta = 59.84 \frac{Rad}{m}$. To experimentally measure β, a bead pull measurement was performed to measure the magnitude of the electric field on the axis of the guide. In this perturbational technique, a probe is placed at each end of the cavity. The transmission is measured at the resonant frequency while a small metallic bead is passed along the cavity axis. The very small shift in resonant frequency (measured as a change in the phase of the transmission) is proportional to the square of the magnitude of the electric field at the bead position. The interested reader is directed to [27], [28] for a detailed discussion of this well-known method.

The results of the bead pull are shown in Fig. 10. The

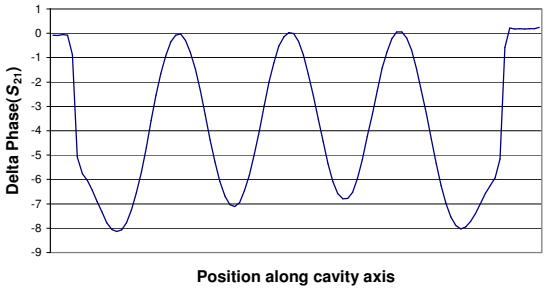

Fig. 10. Bead pull measurement of a 2.8 GHz TM mode of the "keyhole" twisted structure

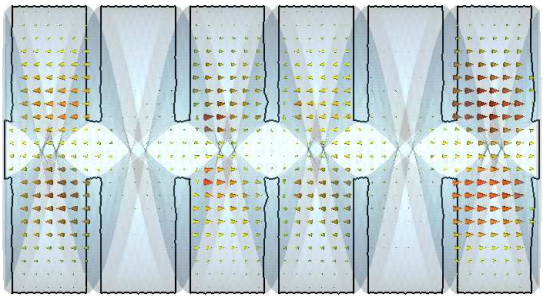

Fig. 11. CST simulation of the "keyhole" twisted structure

horizontal axis shows the bead position along the axis. The plot reveals four distinct minima in the phase of the transmission (corresponding to maxima in the electric field strength). This is consistent with the expectation that the resonant mode has two complete cycles over the cavity length. The small difference between the two middle peaks is likely due to measurement error.

The cavity was also simulated in CST Microwave Studio (Version 2006) [29] (a commercial EM simulation tool which can perform well for slow to moderate twist rates). The predicted resonant frequency was 2.817 GHz, very close to the measured resonant frequency. The electric field is shown in Fig. 11, which indicates four maxima in the magnitude of the electric field along the cavity axis, just as measured in the bead pull. The measured phase velocity, calculated from the measured resonant frequency and phase constant, is $2.95 \times 10^8 \frac{m}{s}$. This offers great practical promise, since many disk loaded structures with similar longitudinal cross section to this twisted structure are designed to accelerate electrons at near relativistic velocities.

Both the CST results and the bead pull measurements indicate that the intensity of the electric field increases close to the end walls of the cavity. This is to be expected, since these walls will cause a perturbation of the mode that would otherwise exist in an infinite twisted waveguide. The three dimensional method must be used if the effects of the end walls cannot be neglected. Analysis of the TM accelerating mode using the proposed techniques is very efficient. For example, using the 2D frequency domain technique, calculation of each mode

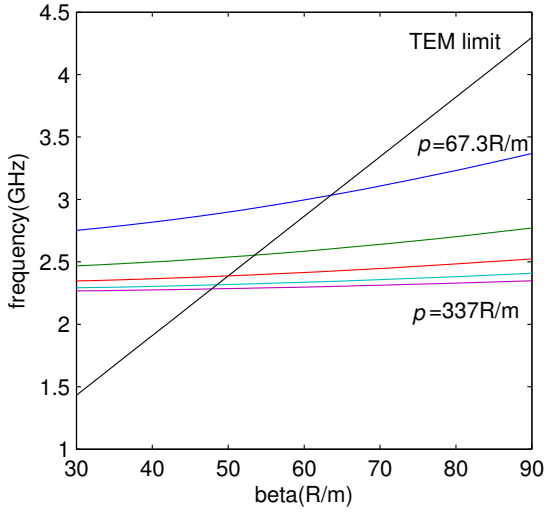

Fig. 12. Predicted dispersion curves of the "keyhole" twisted structure using the 2D frequency domain method for varying twist rates.

for a 25 by 25 grid takes less than 1 second on a 1.86 GHz Intel processor running MATLAB. This allows detailed studies to be performed regarding the dispersion characteristics of a twisted guide, among other things. For this "keyhole" design, the dispersion curves for a variety of twist rates is shown in Fig. 12. It is interesting to note that unlike a TE mode in a twisted rectangular guide, the cutoff frequency is seen to decrease as the twist rate increases. Perturbation theory applied to the dominant mode of a twisted rectangular guide predicts the opposite effect (*i.e.* an increase of the cutoff frequency with increasing twist rate) [5]. This gives one example of how the present method can be readily applied to do very rapid design and optimization of twisted slow wave structures. In addition to dispersion information, other useful figures of merit can be extracted from the eigenmodes of the 2D frequency domain solutions.

VIII. Conclusion

The problem of rapidly twisted structures has been analyzed in detail. The existing perturbation theory methods were found to be quite accurate for low twist rates, but faster twist rates required new models to be developed. Efficient three dimensional and two dimensional numerical techniques have been proposed to solve this problem. These methods are based on an exact straight equivalent waveguide with anisotropic permittivity and permeability that do not vary along the longitudinal direction. This uniformity along the axis of the twisted guide enables the use of conventional 2D nonorthogonal finite difference time and frequency domain solvers.

This work expands the previous work done by Shyroki [6] by treating arbitrary cross sections without the need for a staircase-type mesh and developing a stable two-dimensional (and three dimensional) nonorthogonal finite difference time domain method to solve twisted guides. Arbitrary cross sec-

tions can be analyzed simply using these techniques if a two dimensional structured grid can be created. In addition, good agreement with experimental measurements has been achieved. Moreover, the contributions of end effects to the twisted cavities are investigated experimentally by constructing both long and short twisted prototypes. The experimental data suggests that the 2D methods in both the time and frequency domain become accurate when the twisted structure is very long.

The accuracy and efficiency of these methods will provide an attractive way of designing slow-wave structures for accelerators and traveling wave tubes. It is possible to predict accurately the slowing of the electromagnetic wave, the dispersion relationship, mode characteristics, and higher order modes for such devices. The reduced complexity of these methods circumvents meshing problems associated with existing numerical solvers for very rapidly twisted geometries. As a result, the solutions are obtained in a very efficient fashion.

ACKNOWLEDGMENT

This work has been sponsored by ORNL-SNS. The Spallation Neutron Source is managed by UT-Battelle, LLC, under contract DE-AC05-00OR22725 for the U.S. Department of Energy.

REFERENCES

[1] W. Wang, G. Yu, and Y. Wei, "Study of the ridge-loaded helical-groove slow-wave structure," *IEEE Transactions on Microwave Theory and Techniques*, vol. 45, no. 10, pp. 1689–1695, Oct. 1997.

[2] Y. W. Kang, "Twisted waveguide accelerating structure," in *9th Workshop on Advanced Accelerator Concepts*, Aug. 2000.

[3] L. Lewin, *Theory of Waveguides*. London, Newness-Butherworths, 1975.

[4] H. Yabe and Y. Mushiake, "An analysis of a hybrid-mode in a twisted rectangular waveguide," *IEEE Transactions on Microwave Theory and Techniques*, vol. 32, no. 1, pp. 65–71, Jan. 1984.

[5] H. Yabe, K. Nishio, and Y. Mushiake, "Dispersion characteristics of twisted rectangular waveguides," *IEEE Transactions on Microwave Theory and Techniques*, vol. 32, no. 1, pp. 91–96, Jan. 1984.

[6] D. Shyroki, "Exact equivalent straight waveguide model for bent and twisted waveguides," *IEEE Transactions on Microwave Theory and Techniques*, vol. 56, no. 2, pp. 414–419, 2008.

[7] A. Nicolet, F. Zolla, and S. Guenneau, "Modelling of twisted optical waveguides with edge elements," *European Physics Journal Applied Physics*, vol. 28, pp. 153–157, 2004.

[8] A. Nicolet, F. Zolla, Y. Agha, and S. Guenneau, "Leaky modes in twisted microstructured optical fibers," *Waves in Random and Complex Media*, vol. 17, no. 4, pp. 559–570, Nov. 2007.

[9] J. Chandezon, D. Maystre, and G. Raoult, "A new theoretical method for diffraction gratings and its numerical application," *Journal of Optics*, vol. 11, no. 4, pp. 235–241, 1980.

[10] A. J. Ward and J. B. Pendry, "Calculating photonic green's functions using a nonorthogonal finite-difference time-domain method," *Phys. Rev. B*, vol. 58, no. 11, pp. 7252–7259, Sep. 1998.

[11] R. Holland, "Finite-difference solutions of Maxwell's equations in generalized nonorthogonal coordinates," *IEEE Transactions on Nuclear Science*, vol. 30, pp. 4589–4591, Dec. 1993.

[12] R. Schuhmann and T. Weiland, "Stability of the FDTD algorithm on nonorthogonal grids related to the spatial interpolation scheme," *IEEE Transactions on Magnetics*, vol. 34, no. 5, pp. 2751–2754, Sep. 1998.

[13] P. Thoma and T. Weiland, "Numerical stability of finite difference time domain methods," *IEEE Transactions on Magnetics*, vol. 34, no. 5, pp. 2740–2743, Sep. 1998.

[14] T. Weiland, "Time domain electromagnetic field calculation with finite difference methods," *International Journal of Numerical Modelling*, vol. 9, pp. 295–319, 1996.

[15] Y. Liu, "Fourier analysis of numerical algorithms for the Maxwell equations," *Journal of Computational Physics*, vol. 124, no. 2, pp. 396–416, Mar. 1996.

[16] R. Janaswamy and Y. Liu, "An unstaggered colocated finite-difference scheme for solving time-domain Maxwell's equations in curvilinear coordinates," *IEEE Transactions on Antennas and Propagation*, vol. 45, no. 11, pp. 1584–1591, Nov. 1997.

[17] J.-F. Lee, R. Palandech, and R. Mittra, "Modeling three-dimensional discontinuities in waveguides using nonorthogonal FDTD algorithm," *IEEE Transactions on Microwave Theory and Techniques*, vol. 40, no. 2, pp. 346–352, Feb. 1992.

[18] H. Igarashi and T. Honma, "A finite element analysis of te modes in twisted waveguides," *IEEE Transactions on Magnetics*, vol. 27, no. 5, pp. 4052–4055, Sep. 1991.

[19] A. Nicolet and F. Zolla, "Finite element analysis of helicoidal waveguides," *IET Science, Measurement, and Technology*, vol. 1, no. 1, pp. 67–70, Jan. 2007.

[20] S. Xiao, R. Vahldieck, and H. Jin, "Full-wave analysis of guided wave structures using a novel 2-D FDTD," *IEEE Microwave and Guided Wave Letters*, vol. 2, no. 5, pp. 165–167, May 1992.

[21] M.-L. Lui and Z. Chen, "A direct computation of propagation constant using compact 2-D full-wave eigen-based finite-difference frequency domain technique," in *Proceedings of the 1999 International Conference on Computational Electromagnetics Applications*, 1999, pp. 78–81.

[22] Y.-J. Zhao, K.-L. Wu, and K.-K. M. Cheng, "A compact 2-D full-wave finite-difference frequency-domain method for general guided wave structures," *IEEE Transactions on Microwave Theory and Techniques*, vol. 50, pp. 1844–1848, Jul. 2002.

[23] L.-Y. Li and J.-F. Mao, "An improved compact 2-D finite-difference frequency-domain method for guided wave structures," *IEEE Microwave and Wireless Components Letters*, vol. 13, no. 12, pp. 520–522, Dec. 2003.

[24] C. S. Lavranos and G. A. Kyriacou, "A finite difference frequency domain study of curvature lifted modes degeneration," in *Progress in Electromagnetics Research Symposium*, Aug. 27–30, 2007, pp. 222–226.

[25] P. Barrera, G. Gonzalez, L. Castellanos, and A. Prez. (2008, May) Unamalla mesh generation package. [Online]. Available: http://www.mathmoo.unam.mx/unamalla

[26] K. H. Flouds and J. R. Mansell, "Propagation of an electronic wave through a helical waveguide," *Proc of IEE*, vol. 3, no. 11, pp. 1789–1798, 1964.

[27] L. Maier and J. Slater, "Field strength measurements in resonant cavities," *Journal of Applied Physics*, vol. 23, no. 1, pp. 68–77, Jan. 1952.

[28] D. Goldberg and R. Rimmer, "Measurement and identification of HOMs in RF cavities," in *Proceedings of the 1997 Particle Accelerator Conference*, vol. 3, May 12–16, 1997, pp. 3001–3003.

[29] *CST Microwave Studio 2006 Users Manual*. CST Ltd., Darmstadt, Germany.

Appendix C

Applications of Twisted Hollow Waveguides as Accelerating Structures

Applications of Twisted Hollow Waveguides as Accelerating Structures

Joshua L. Wilson, *Student Member, IEEE,* Aly E. Fathy, *Fellow, IEEE,* Yoon W. Kang, *Senior Member, IEEE* and Cheng Wang

***Abstract*—A new class of accelerating structures employing a uniformly twisted waveguide is considered. Such a twisted helical structure can be designed to have a specified longitudinal cross section. The design of twisted accelerating structures is discussed with regard to particle velocity and strength of the accelerating field. It is shown how to choose a cross section and twist rate in order to produce a given amount of wave slowing. Obtained wave velocities range from the speed of light, c, to 61% the speed of light, while $\frac{R}{Q}$ values of over 1,000 have been achieved. A novel two dimensional finite difference based solver is employed to analyze the twisted structures considered. Two twisted cavity prototypes are fabricated and measured, and excellent agreement is obtained between measured and predicted values.**

I. Introduction

ACCELERATING structures exploit the interaction of an electromagnetic wave with a charged particle to increase the kinetic energy of the particle. In order to accomplish this, the velocity of the wave must be matched to that of the particle. This precludes the use of any simple hollow waveguide structure, as these all support waves that travel faster than c.

The problem of slowing the phase velocity of an electromagnetic wave to c or below has been a topic of extensive investigation. For example, a simple method that has been thoroughly investigated involves using a TM mode in a waveguide partially loaded with dielectric material [1], [2], [3]. Dielectric loaded accelerating structures show great promise in damping of higher order modes [1], yet the presence of the dielectric presents challenges in areas of manufacturing cost and vacuum conditioning. Also, application of dielectric loaded cavities to superconducting accelerators is not practical.

The standard approach to slowing the EM wave has been to introduce periodic reactive loading to the hollow waveguide or cavity. This can be done by using periodically spaced irises as in the conventional disk-loaded accelerating structure (see [4] for a typical design) or by using some smoothly corrugated guide as in the elliptical TESLA-type cavity [5]. Whatever the nature of the reactive loading, the result is a slow-wave periodic structure whose phase velocity is matched to the particle. However, the non-uniform cross section of these cavities gives rise to troubling trapped modes which can cause beam instabilities, fields whose magnitudes vary significantly along the axis, and added manufacturing costs.

Here, we discuss the accelerator application of a uniformly twisted hollow waveguide and compare with conventional accelerating cavities. Because the uniformly twisted guide is geometrically self-similar along a continuous helical path, it deserves consideration as a special class of periodic structure and possesses unique features making it an interesting candidate for accelerating structures.

The idea of a twisted waveguide accelerating structure was proposed in a previous paper [6]. In that paper, it was shown that a twisted waveguide could support electromagnetic waves that traveled with a phase velocity less than c. Since this type of structure has a uniform cross section, it can be fabricated without welding or brazing unlike reactively loaded accelerating structures. In [6], MAFIA code was used to simulate the twisted waveguide using stacked waveguide slices. In this paper, we extend the analysis of the twisted waveguides using a specially designed two-dimensional simulation method [7]. Although ordinary EM codes (such as MAFIA) can yield accurate results, the custom code we have developed specifically for twisted guies can run much faster and facilitate easier optimizations.

An important design consideration is the optimization of the shunt impedance R, defined as

$$R = \frac{V^2}{2P}, \tag{1}$$

where V is the on-axis accelerating potential and P is the dissipated power. Because this parameter is dependent on the material of the cavity walls, the shunt impedance is often normalized to the quality factor Q. Thus, the value of $\frac{R}{Q}$ is an important figure of merit for a cavity geometry. Often, when dealing with waveguides or long cavities, $\frac{R}{Q}$ is normalized to the length, making $\frac{R}{Ql}$ a useful figure of merit if l is the cavity length.

In this paper, we discuss the helical geometry specifically as it compares to ordinary rotationally symmetric accelerating structures. Then, the electromagnetic modes of twisted structures are analyzed and discussed. Prototypes of twisted accelerating structures are presented, and experimental results are compared to theory. The dispersion characteristics of twisted guides are discussed with relation to conventional periodically loaded accelerating structures. Finally, we present some practical design considerations for twisted accelerating guides.

II. Twisted Geometry

The mathematical definition of a twisted volume was given in a previous paper [7], where we utilized the twisted (or helicoidal) coordinate transform employed by Lewin [8].

Yoon Kang is with the Spallation Neutron Source (SNS) at Oak Ridge National Laboratory

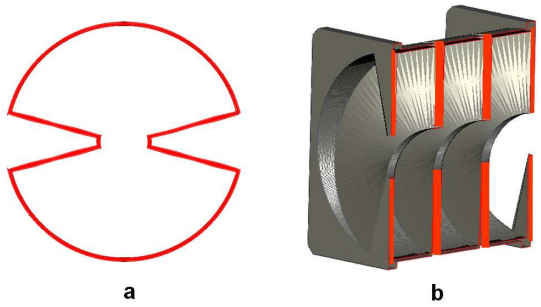

Fig. 1. A twisted analog to the disk-loaded slow-wave structure

$$\begin{aligned} x' &= x\cos pz + y\sin pz \\ y' &= y\cos pz - x\sin pz \\ z' &= z \end{aligned} \tag{2}$$

Here, p is some constant twist rate. We consider that a twisted structure can be designed to have any desired longitudinal cross section by appropriately selecting a transverse cross section to be twisted. Thus, all the well-known accelerator geometries (iris-loaded, elliptical, etc.) have twisted analogs whose longitudinal cross section is identical.

Such a twisted analog can be constructed in the following fashion. Assume we have a rotationally symmetric structure defined by

$$\rho < g(z), \tag{3}$$

where g is some periodic function with periodicity Δz. We define a 2D transverse cross section in polar coordinates (ρ, ϕ)

$$\rho(x,y) < g\left(\frac{\phi(x,y)\Delta z}{\pi}\right) \tag{4}$$

and set the twist rate

$$p = \frac{\pi}{\Delta z}. \tag{5}$$

The transformation of Equation 2 is then used to generate the analog. The twisted analog also allows some interesting comparisons to be made between twisted and rotationally symmetric non-twisted structures, as both can be used as slow wave structures.

The twisted analog defined above is not unique. It is easily observed that any two dimensional profile defined by

$$\rho(x,y) < g\left(\frac{m\phi(x,y)\Delta z}{2\pi}\right) \tag{6}$$

and twist rate

$$p = \frac{2\pi}{m\Delta z} \tag{7}$$

has identical longitudinal cross section to the original rotationally symmetric structure for any even integer m. An example of such a twisted analog is shown in Fig. 1. In this case, the "keyhole" cross section of (a) is extruded along a twisted path to form the volume (b), whose longitudinal cross section is identical to a disk-loaded accelerating structure.

In this study, two twisted structures are compared to their rotationally symmetric analogs. The first is the "keyhole" structure just described, and the second is an analog to the elliptical TESLA-style cavity, specifically related to the medium beta superconducting cavity at the Spallation Neutron Source (SNS) [9].

III. Electromagnetic Modes in Twisted Waveguides

Because the twisted waveguides under consideration are periodic in z, Floquet's theorem predicts that the fields will also have the same periodicity, except for a multiplicative phase factor. In this case, the period of the twisted waveguide will be $2\pi/p$. However, for the case of a uniformly twisted waveguide, it turns out that one can make an even stronger statement.

Assume the fields at some $z = z_0$ are known. Moving a distance dz along the axis of the twisted structure, the structure is exactly the same except for some rotation of angle $p\,dz$. Therefore, as shown in [10] for structures having "screw symmetry", the fields intuitively should be the same except for a phase factor. This relation holds true for any dz, not just $dz = 2\pi/p$. In particular, we can send dz to zero and discover that for an infinite twisted waveguide, the variation of the fields along the axis of propagation involves only simple phase variation. In other words, except for the constant rotation of the fields, the z dependence can be factored out as $e^{-j\beta z}$ for some phase constant β. In terms of the twisted coordinates,

$$\boldsymbol{E}(x',y',z') = \boldsymbol{E_0}(x',y')e^{-j\beta z'} \tag{8}$$

This separation of the z dependence for twisted guides is significant, since it cannot generally be done for periodic structures. In Equation 8, it was possible to replace $e^{-j\beta z}$ with $e^{-j\beta z'}$, since z and z' are numerically equal. Similar relations hold for $\boldsymbol{H}$. Thus, if a twisted coordinate system is used, the fields in a twisted waveguide can be represented in exactly the same fashion as for an infinite straight waveguide. A more mathematical way of showing this equivalence between straight and twisted fields involves an equivalent straight waveguide loaded with some anisotropic material. This equivalent was given approximately in [6], and an exact equivalent is given in [11], [7]. The anisotropic material equivalent also shows that one can make a twisted structure effectively "look" like a dielectric loaded structure without having the undesirable effects associated with real dielectrics.

In addition to simplifying the analysis greatly, this property of the uniformity of the fields along the axis of propagation also provides practical advantages for accelerating structures. In a periodic structure, the fields can be expressed by an infinite Floquet expansion. For example,

$$\boldsymbol{E} = \sum_{n=-\infty}^{\infty} \boldsymbol{E}_n(x,y)e^{j\beta_n z} \tag{9}$$

where

$$\beta_n = \beta_0 + \frac{2\pi n}{\Delta z}. \tag{10}$$

However, in the twisted coordinate system of (2), we have $\boldsymbol{E}_n = 0$ for all $n \neq 0$, due to the fact that the waveguide

TABLE I
PARAMETERS FOR TWISTED ANALOG TO DISK-LOADED ACCELERATING CAVITY

Parameter	Value	Unit
Outer radius	5.493	cm
Inner radius	1.135	cm
Twist Rate	89.76	Radians/m
Phase advance per $\frac{1}{2}$ turn	$\frac{2\pi}{3}$	Radians
Notch angle	30	Degrees

becomes equivalent to a straight waveguide under the coordinate transformation. Thus, only a single space harmonic is present. In conventional coordinates (cylindrical or cartesian), an infinite number of space harmonics will still be needed, but along the z axis (which coincides with the z axis of the twisted coordinate transform) all higher space harmonics must vanish:

$$\boldsymbol{E}_n(x=0, y=0) = 0, n \neq 0. \tag{11}$$

The implication of this is that along the axis of an infinite twisted structure there is no variation in the magnitude of the fields – only in the phase. This distinguishes the twisted guide from conventional slow-wave structures (like corrugated or iris-loaded waveguides). Since only the $\boldsymbol{E}_0$ harmonic travels synchronously with the particle beam and acts cumulatively to accelerate the particles, the elimination of other harmonics is very desirable, and it could be accomplished using the twisted structure.

A word should be said here regarding a well-known twisted structure already used in traveling wave devices, namely the helix traveling wave tube. Although such a slow-wave device shares much in common with the twisted waveguides we are proposing, there are also some notable differences. First, the helix is an open waveguide structure meaning that the fields do not drop to zero outside the structure but rather decay exponentially, roughly following a modified Bessel function of the second kind. This presents a problem at high power, where these fields may not be negligible. Second, the radial component of the wavenumber $h = \sqrt{\beta^2 - k_0^2}$, which dictates the decay rate for the fields outside the helix, approaches zero as the phase velocity of the wave approaches c, indicating that the helix becomes inefficient at relativistic velocities.

To demonstrate the slow-wave capabilities of twisted structures, we again consider the shape of Fig. 1. To design a practical accelerating structure having this geometry, we started out with the dimensions of the well-known SLAC accelerating cavity [4]. It was found, however, that the twisted analog had phase velocity greater than c. To lower the phase velocity, the outer diameter of the cavity was increased until the velocity was c. The physical parameters of this structure are given in Table I.

The notch angle referred to in Table I is the angle of the notch in the "keyhole" transverse cross section. This example shows how a twisted structure can easily be compared to a non-twisted rotationally symmetric structure. For example, in the SLAC accelerating cavity, the phase advance per cell is $\frac{2\pi}{3}$. Similarly, one can consider one half twist of the twisted waveguide as a "cell" and define a $\frac{2\pi}{3}$ mode in the same way.

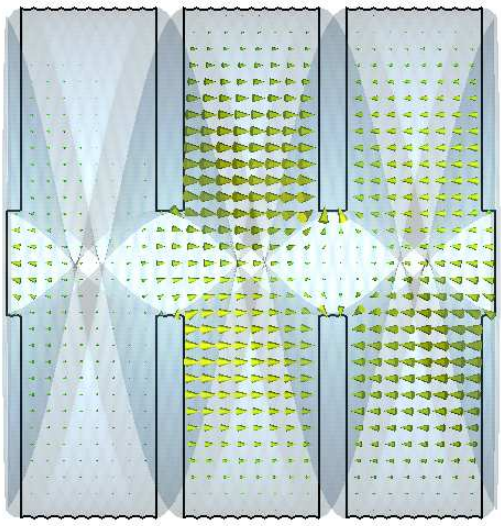

Fig. 2. Electric field of twisted analog of a disk-loaded cavity: CST simulation

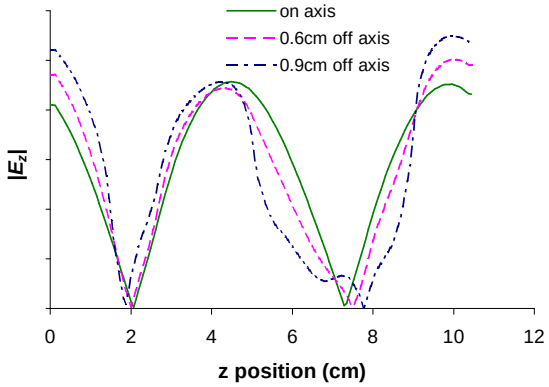

Fig. 3. Magnitude of $\boldsymbol{E_z}$ for on-axis and off-axis particles: CST simulation

A visual representation of the fields in such a structure is provided using CST Microwave Studio simulation [12], and is shown in Fig. 2. A periodic boundary condition was established at the ends of the twisted structure. The Microwave Studio solution represents a standing wave rather than a traveling wave solution. Such a solution can be easily constructed from two counterpropagating traveling wave solutions. The vector electric field is shown as arrows in the figure. The z component of the electric field is plotted in Fig. 3 for a particle on the z-axis, a particle 0.6 cm off axis, and a particle 0.9 cm off axis. Very far from the center of the guide near the groove region, it is easily seen that the field does not vary sinusoidally with the longitudinal coordinate z, indicating that many space harmonics are present in this region. On the other hand, close to the center of the guide, the field variation is sinusoidal as all space harmonics except the fundamental disappear.

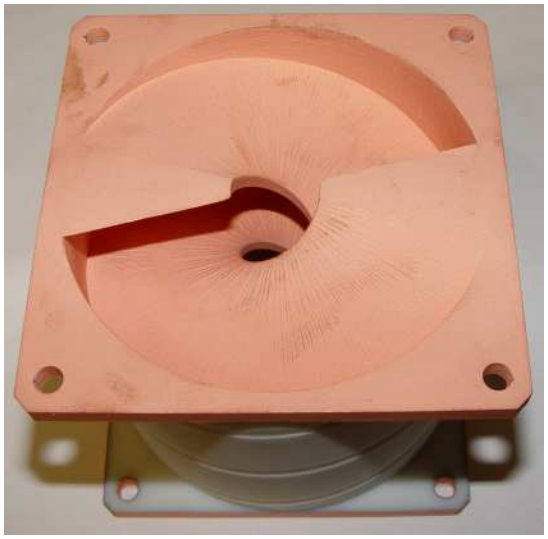

Fig. 4. Fabricated "keyhole" cross-section prototype

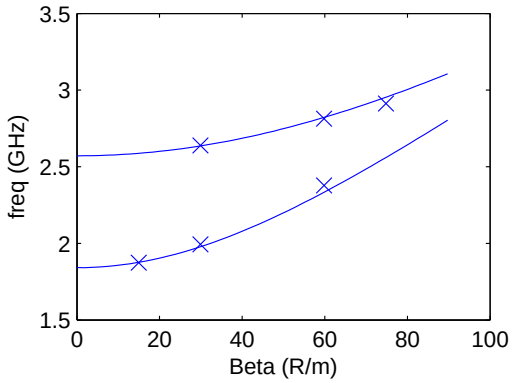

Fig. 5. Predicted and measured dispersion curves for two modes of a twisted analog to a disk-loaded cavity. The mode with higher frequency is the TM accelerating mode. The x's are experimental points.

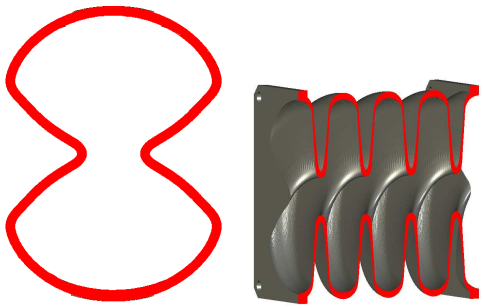

Fig. 6. Cross section and cutaway view of the twisted elliptical prototype.

IV. Experimental Investigation

A twisted cavity prototype for the "keyhole" structure with the dimensions in Table I was printed using an SLA (Stereolithography Apparatus) process. The inside surface was electroplated with copper. The prototype is shown in Fig. 4. Two identical prototypes were made and placed end to end for a total of three complete twists. The structures were terminated with copper shorting plates to form a cavity resonator. A small probe was inserted through each shorting plate, and the transmission was measured to determine the cavity resonances. A bead pull measurement was also performed to determine the value of the phase constant for each of the resonances. The theory of the bead pull technique is discussed in [13], [14], [15] and summarized in Appendix A. This measurement allowed us to determine the variation of the electric field along the cavity axis, from which the phase constant could easily be extracted. Knowing the resonant frequency and the phase constant for each resonant mode, it is now possible to compare the dispersion characteristics to those predicted by theory [7]. The comparison is shown in Fig. 5. There is generally good agreement between the experimental and theoretical results. The discrepancies are likely caused by disturbances introduced by the end walls, which perturb the cavity fields from what they would otherwise be in an infinite twisted guide.

A twisted analog to an elliptical (TESLA-style) cavity is also considered. This design was accomplished in the same way as the disk-loaded analog design, by using (4)-(5). It was found necessary to increase the outer radius in order to ensure that the relativistic $\beta = \frac{v}{c} = 0.61$, which is the same as the SNS medium-beta superconducting cavity. (Note that this β is different from the phase constant discussed earlier.) The final prototype design had inner radius 1.24 cm, outer radius 3.37 cm, and twist rate 96.2 Rad/m. Fig. 6 shows the "dumbbell" shape of the transverse cross section of this slow wave structure, and a cutaway view showing the longitudinal cross section, which is identical to the well-known TESLA-type elliptical profile. Again, two identical prototypes were fabricated, and when placed end to end provide four complete twists. The prototype is shown in Fig. 7, and the dispersion curve for the accelerating mode is shown in Fig. 8. Many additional resonances were observed other than the ones shown in Fig. 8, but their relatively low Q values afforded by the rough cavity walls and other experimental factors prohibited an accurate bead pull measurement of these modes. However, the data points gathered for the accelerating mode of interest show good agreement with theory.

In addition to the dispersion characteristics, the profile of the electric field gathered from the bead pull measurement was analyzed, and experimental $\frac{R}{Q}$ values for each of the two prototypes were obtained. The z component of the axial electric field is proportional to the root of the change in resonant frequency due to the bead at each position (see Appendix A). These measurements are shown for the twisted analog to the disk-loaded and elliptical cavities in Figs. 9 and 10, respectively.

The appearance of the electric field along the cavity axis is seen to be roughly sinusoidal in the center of the cavity.

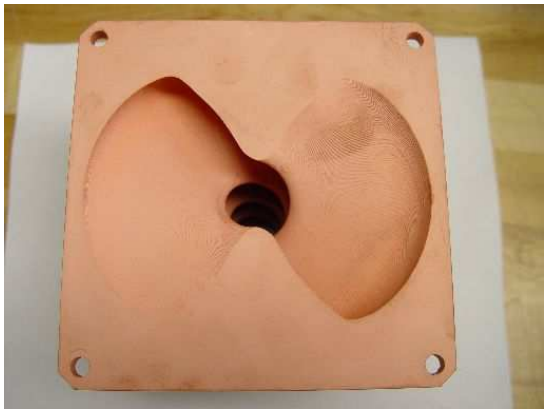

Fig. 7. Fabricated elliptical cross-section prototype

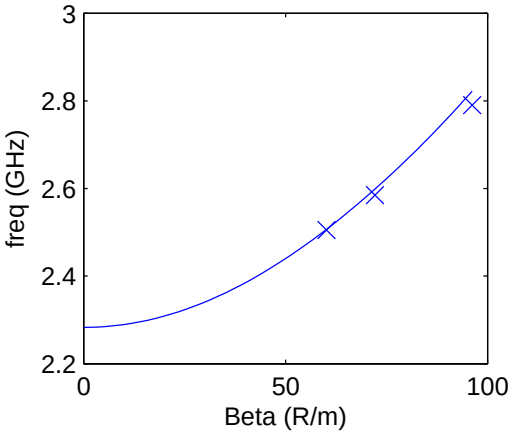

Fig. 8. Predicted and measured dispersion curves for the accelerating mode of an elliptical twisted guide. The x's are experimental points.

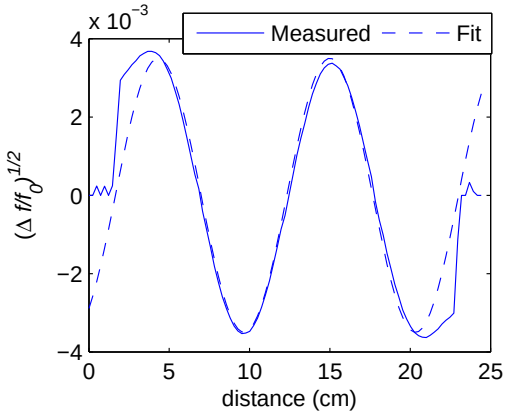

Fig. 9. Measured field in the twisted analog of the disk-loaded cavity.

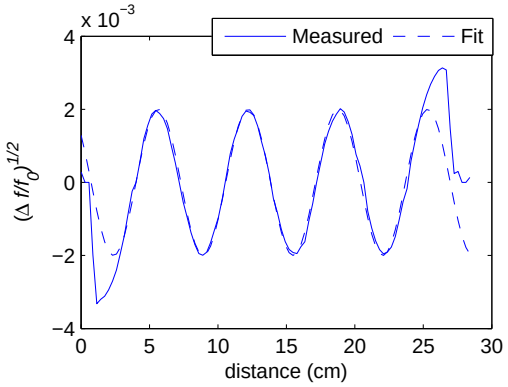

Fig. 10. Measured field in the twisted elliptical cavity.

Since theory predicts the existence of only one space harmonic along the center axis, and hence a simple sinusoidal variation of the electric field, a sinusoidal curve was designed to fit the measured data and is shown alongside the data in Figs. 9 and 10. The sinusoid has distribution

$$y = A\sin(kz + \phi), \tag{12}$$

where

$$k = \frac{\omega}{\beta c}. \tag{13}$$

Here, β is the relativistic quantity that is equal to 1 for the twisted analog of the disk-loaded cavity and 0.61 for that of the elliptical cavity. The other constants, A and ϕ, are chosen to best fit the measured data. These data show that the electric field has a sinusoidal appearance close to the center of the cavity, while end effects cause a deviation close to the cavity end walls.

Using the techniques of [15], the $\frac{R}{Ql}$ of the twisted structures were found. Table II shows a comparison between measured and predicted values. There are several sources of measurement error. The formulas given in [15] (and repeated in Appendix A) are only valid if all other field components except E_z are zero, which may not be exactly the case for the measured twisted structures. Temperature drift during the measurement and uncertainty regarding the precise value of the form factor for the perturbing metal bead also contributed some error. In addition, end effects may play a role, causing an increase of the field strength close to the metal end walls of the cavity. This would cause the measured $\frac{R}{Q}$ to be more than what would be predicted assuming the cavity was infinite in length, explaining why the measured $\frac{R}{Q}$ values to be higher than predicted for an infinite structure. This is particularly the case with the elliptical structure, where edge effects are seen from Fig. 10 to be quite pronounced.

The problem of reducing end effects requires careful consideration. Although not addressed in detail here, we have shown previously that in some cases the end effects can be mitigated by introducing a curved boundary surface as the end wall [6]. Another approach is to eliminate the end walls and leave them open to a waveguide interface, which then

has to be properly matched to the twisted structure. These considerations are beyond the scope of the present paper.

TABLE II
COMPARISON OF MEASURED AND PREDICTED $\frac{R}{Q}$ VALUES FOR TWO TWISTED PROTOTYPES

Cavity type	Measured $\frac{R}{Ql}$	Predicted (Infinite Structure) $\frac{R}{Ql}$
Disk-loaded	776 Ω/m	716 Ω/m
Elliptical	248 Ω/m	223 Ω/m

V. Discussion of Dispersion Characteristics

In this section, we will discuss two desirable features of the dispersion characteristics that are unique to twisted guides. First, we would show that the dispersion characteristics are particularly desirable in the prevention of higher order trapped modes. Second, we demonstrate that the problem of mode separation can be dealt with more easily than in non-twisted periodic geometries.

Higher order trapped modes are troublesome in most conventional periodically loaded accelerating structures because of the appearance of stop-bands in the dispersion characteristic. When beam energy is deposited in such a stop band, the excited fields cannot propagate out of the structure to higher-order mode dampers and remain "trapped" in the accelerating cavity. Such modes are particularly problematic in superconducting cavities, because the large Q values allow these unwanted resonances to continue for a long time before finally decaying due to wall losses. In the case of the twisted guide, however, there are no stop bands above the cutoff frequency of the fundamental propagating mode. Although this may not be apparent from the appearance of Figs. 5 and 8, these figures show only the first branch of the propagating modes (*i.e.* those whose phase constant is between 0 and $\frac{\pi}{\Delta z}$). In reality, these modes can be thought of to continue on to infinitely high values of β by virtue of the straight waveguide equivalent.

A second observation relates to mode spacing in these accelerating structures. Many periodically loaded accelerating cavities operate very efficiently close to π mode, or 180 degrees of phase shift per unit cell. However, near the point on the dispersion curve where $\beta = \frac{\pi}{\Delta z}$, the group velocity (calculated as $\frac{d\omega}{d\beta}$) typically approaches zero. This prohibits effective operation, since nearby unwanted modes would be excited very easily. One solution to eliminate the problem of zero group velocity at π mode is the deliberate creation of confluent pass bands, with the point of confluence judiciously selected as the point of the desired π mode operation [16]. However, this requirement places a significant constraint on the design of the periodic accelerating structure. In the case of the twisted waveguide no such problem exists, as the group velocity remains nonzero for all values of the phase constant β.

VI. Design Considerations

In our discussion of practical design consideration, we will consider mainly variations on the twisted analogs to the disk-loaded accelerating structure. While there are infinite number of possible cross sections, this shape can be particularly instructive due to its simplicity. Other cavity shapes, such as the twisted elliptical cavity, can be thought of (at least to first order approximation) as a disk-loaded analog with rounded edges.

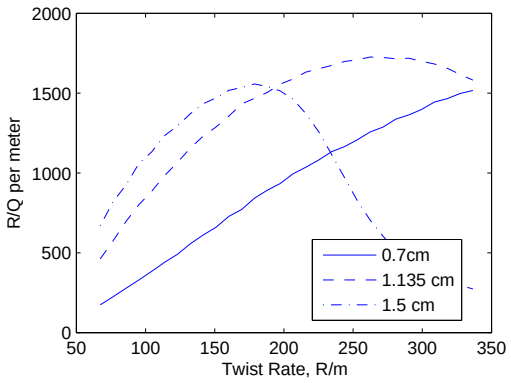

Fig. 11. Simulated effect of changing the inner radius on $\frac{R}{Q}$.

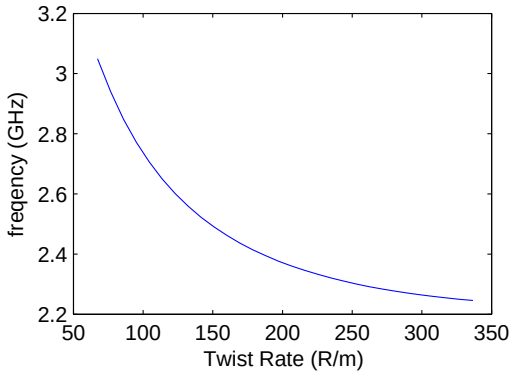

Fig. 12. Simulated frequency as a function of twist rate. (Phase velocity held equal to c.)

In the current study, it was investigated how to maximize the value of $\frac{R}{Q}$ with respect to the rate of twisting for the twisted analog to the disk-loaded accelerating structure. We assumed that the structure was constrained to have a phase velocity equal to c for accelerating relativistic particles. For each value of the twist rate p, the frequency was adjusted in simulation in order to satisfy the phase velocity constraint. $\frac{R}{Q}$ was calculated from simulation using the technique found in Appendix B. For the twisted analog to the disk loaded accelerating structure, we show $\frac{R}{Q}$ performance for inner radii of 0.7 cm, 1.135 cm (design value), and 1.5 cm. This is shown as a function of the twist rate in Fig. 11.

For the design case of 1.135 cm inner radius, the frequency should be adjusted as a function of the twist rate as shown in Fig. 12.

In conventional accelerator cavities, a small iris radius is

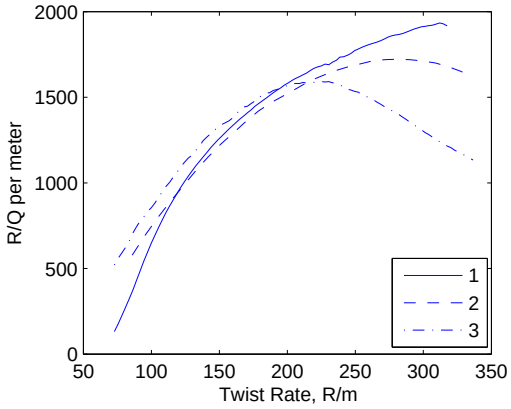

Fig. 13. Simulated effect of changing m on $\frac{R}{Q}$.

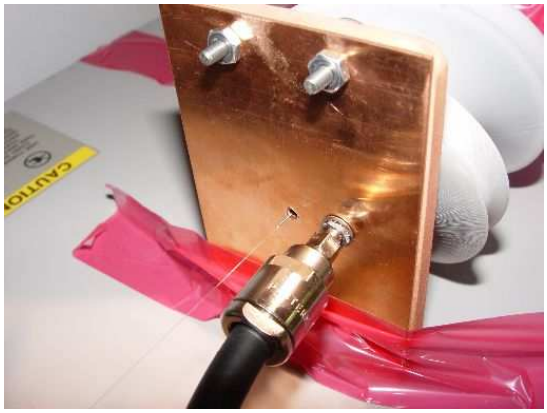

Fig. 14. Bead pull measurement setup, showing the metallic needle (barely visible at the cavity entrance) and fishing line going through the copper end plate of the twisted cavity. The cable in the photograph is connected to a small probe which is used to measure S_{21}.

desirable for higher shunt impedances, but has the drawback that it decreases the maximum allowable size of the beam; so a design tradeoff is often needed. For the experimental prototype, the twist rate was only 89.76 $\frac{Rad}{m}$, so in practice a relatively higher value for the twist rate will yield higher values of $\frac{R}{Q}$.

We consider the effect of a varying cross section on these curves. Two parameters in particular are varied: the inner radius of the notch (corresponding to the iris radius of the disk loaded analog) and the value of m in Eq. 6.

The figure indicates that while the $\frac{R}{Q}$ can be increased somewhat by choosing a smaller inner radius, at low twist rates, a larger radius can actually be desirable.

We then investigated changing the parameter m in Eq. 6. For a given twist rate, changing m leads to either compressing or expanding the longitudinal cross sectional shape in the axial direction. For even values of m, the cross section will be identical to that of a disk loaded cavity. For odd values of m, the cross section would be a "staggered" version of the original cross section. Again, we hold all other parameters constant, and show the effect of changing m on $\frac{R}{Q}$ as a function of the twist rate. We considered values of m ranging from 1 to 3, with $m = 2$ the design value. The results are presented in Fig. 13. In general, the value of m does not effect the $\frac{R}{Q}$ value significantly except at high twist rates. However, higher values of m lead to a more complex structure and may be more difficult to manufacture. Generally, then, lower m values are preferable.

VII. Conclusion

We investigated a new type of accelerating structure consisting of a uniformly twisted waveguide. Using the simple method presented in this paper, it is possible to construct a twisted accelerating structure whose longitudinal cross section matches a predefined shape. Twisted structures have been successfully modeled using a theory presented in a previous paper, and experimental measurements on two twisted accelerating cavity candidates indicate excellent agreement with theory.

It has been demonstrated that twisted waveguides are able to slow an electromagnetic wave to velocities below c without the introduction of problematic dielectrics or open structures. These slow wave modes permit interaction with an electron or ion beam. Twisted structures also offer the possibility of uniform acceleration of on-axis particles because of the vanishing of all higher order space harmonics along the center axis of the guide.

Appendix A
Bead Pull Measurements and $\frac{R}{Q}$ Determination

To measure the electric field along the axis of the twisted cavities and calculate their $\frac{R}{Q}$, a bead pull measurement was carried out. A small metallic needle was threaded by a fishing line and moved through the cavity by a stepper motor and pulley system. Two small holes on the copper end walls accommodated the needle and line. The bead and line is shown at the entrance to the twisted cavity in Fig. 14.

The needle's volume was calculated to be $\Delta V = 1.12 \times 10^{-9} m^3$. The needle had length $l = 3.6mm$ and diameter $d = 0.63mm$. This leads to an aspect ratio of 5.71. According to [15], for $l/d \gg 1$, the metallic cylinder can be considered to be a spheroid of major axis $l/2$ and minor axis $d/2$. Making this approximation, we calculate the eccentricity

$$e = \sqrt{1 - \frac{d^2}{l^2}} = 0.985. \tag{14}$$

From here, the depolarization $L_\parallel$ is calculated using [15].

$$L_\parallel = \frac{1+e^2}{e^3}\left(\frac{1}{2}\ln\frac{1+e}{1-e} - e\right), \tag{15}$$

from which we have the depolarization factor

$$F_1 = \frac{1}{3L_\parallel}. \tag{16}$$

Finally, the $\frac{R}{Q}$ is calculated from the formula

$$\frac{R}{Q} = \frac{1}{3\pi f_0 \Delta V F_1 \epsilon_0} \left[\left(\int \sqrt{\frac{\Delta f}{f_0}} \cos kz \, dz \right)^2 + \left(\int \sqrt{\frac{\Delta f}{f_0}} \sin kz \, dz \right)^2 \right], \tag{17}$$

which is the same as the formula given in [15], except for a factor of 2 which is due to the fact that we used the definition

$$\frac{R}{Q} = \frac{V_{acc}^2}{2\omega U}, \tag{18}$$

where V_{acc} is the on-axis accelerating voltage and U is the stored energy. Δf was measured indirectly through measuring the phase of the transmission coefficient S_{21} and using the approximation

$$\frac{\Delta f}{f_0} = \frac{\tan(\angle S_{21})}{2Q_L}, \tag{19}$$

where Q_L is the measured (loaded) Q of the cavity. Since Δf is proportional to E_z^2, it always has the same sign. To calculate $\sqrt{\frac{\Delta f}{f_0}}$, then, requires that the correct branch of the square root be judiciously chosen. To do this, we examined the Δf data and found points where it was nearly zero and the corresponding intervals in between such zero points. Every other interval was then multiplied by -1 to achieve the sinusoidal appearance of Figs. 9 and 10.

The measured $\frac{R}{Q}$ was for a standing wave pattern, while in the simulation we assumed a traveling wave. If a standing wave mode is considered a sum of two traveling wave modes, it is obvious that only the forward traveling wave (traveling synchronously with the particle) contributes to the acceleration, and thus to the value of V_{acc}. However, the energy of the wave will reflect both the forward and backward components. As a result, the traveling wave $\frac{R}{Q}$ is twice the standing wave value. Thus, to calculate the traveling wave $\frac{R}{Ql}$, the measured $\frac{R}{Q}$ was multiplied by 2 and taken over the length of the cavity.

APPENDIX B
NUMERICAL SIMULATION DETAILS

The twisted accelerating structures were simulated using the two dimensional methods found in [7], specifically the two-dimensional finite-difference frequency domain method. The frequency domain method permits direct extraction of the eigenvectors given a propagation constant β. For each twisted cross section, a two-dimensional structured mesh was generated using the computer code UNAMALLA [17]. We then use the coordinates of the structured mesh to compute the metric tensor components [7]:

$$[g_{ij}] = \begin{bmatrix} x_{x'}^2 + y_{x'}^2 & x_{x'}x_{y'} + y_{x'}y_{y'} & pxy_{x'} - pyx_{x'} \\ x_{x'}x_{y'} + yyx'y_{y'} & x_{y'}^2 + y_{y'}^2 & pxy_{y'} - pyx_{y'} \\ pxy_{x'} - pyx_{x'} & pxy_{y'} - pyx_{y'} & 1 + p^2(x^2 + y^2) \end{bmatrix}. \tag{20}$$

At each point in the rectangular $x' - y'$ domain, the physical coordinates x and y are given by the mesh generation program, and the partial derivatives in the equation above can then be approximated using finite differences. For the simulations in this paper, a 51X51 mesh was employed and reasonable convergence was achieved.

The $\frac{R}{Q}$ value can be computed from the simulated traveling wave eigenmode if the energy per unit length U/l is calculated. Then, the following formula is utilized:

$$\frac{R}{Q} = \frac{|E_{z,axis}|^2}{2\omega(U/l)} \tag{21}$$

or

$$\frac{R}{Ql} = \frac{|E_{z,axis}|^2}{2\omega(U)} = \frac{|E_{3,axis}|^2}{\omega \iint \left(\sum_{j,k=1}^{3} \epsilon_0 g^{jk} E_j E_k + \mu_0 g^{jk} H_j H_k \right) \sqrt{g} dx' dy'}.$$

Here, E_i and H_i represent the i covariant component of the respective fields in the transformed coordinate system, g^{ij} correspond to the components of the contravariant metric tensor, and g is the determinant of the covariant metric tensor. (21) is valid at the center of the guide, where $E_3 = E_z$. The expression for the total energy per unit length U, which appears in the denominator, is the same whether derived in twisted or Cartesian coordinates. The integration is then performed over the rectangular $x' - y'$ cross section in the transformed coordinate system. The method was analyzed by comparing results to CST for the case of an infinite twisted disk loaded analog of the same type as the measured prototype except with a slightly more rapid twist rate of 150 Rad/m. An agreement to within 6.7 % was achieved.

ACKNOWLEDGMENT

This work has been sponsored by ORNL-SNS. The Spallation Neutron Source is managed by UT-Battelle, LLC, under contract DE-AC05-00OR22725 for the U.S. Department of Energy.

REFERENCES

[1] C. Jing, W. Gai, J. Power, R. Konecny, S. Gold, W. Liu, and A. Kinhead, "High-power RF tests on x-band dielectric-loaded accelerating structures," *IEEE Transactions on Plasma Science*, vol. 33, no. 4, pp. 1155–1160, Aug. 2005.

[2] J. Power, W. Gai, S. Gold, A. Kinkead, R. Konecny, C. Jing, W. Liu, and Z. Yusof, "Observation of multipactor in an alumina-based dielectric-loaded accelerating structure," *Physics Review Letters*, vol. 92, no. 16, Apr. 2004.

[3] C. Jing, W. Liu, W. Gai, J. Power, and A. Kanareykin, "34.272 GHz multilayered dielectric-loaded accelerating structure," in *Proceedings of 2005 Particle Accelerator Conference*, 2005, pp. 1952–1954.

[4] R. P. Borghi, A. L. Eldredge, G. A. Loew, and R. B. Neal, *Design and Fabrication of the Accelerating Structure for the Stanford Two-Mile Accelerator*. Academic Press, New York, N. Y., vol. 1.

[5] J. Sekutowicz, "TESLA superconducting accelerating structures," *Measurement Science and Technology*, vol. 18, no. 8, pp. 2285–2292, 2007.

[6] Y. W. Kang, "Twisted waveguide accelerating structure," in *9th Workshop on Advanced Accelerator Concepts*, Aug. 2000.

[7] J. Wilson, C. Wang, A. Fathy, and Y. Kang, "Analysis of rapidly twisted hollow waveguides," *Submitted to IEEE Transactions on Microwave Theory and Techniques*, Jun. 2008.

[8] L. Lewin, *Theory of Waveguides*. London, Newness-Butherworths, 1975.
[9] C. Rode, "The SNS superconducting linac system," in *Proceedings of the 2001 Particle Accelerator Conference*, vol. 1, Jun. 18–22, 2001, pp. 619–623.
[10] P. Crepeau and P. McIsaac, "Consequences of symmetry in periodic structures," *Proceedings of the IEEE*, vol. 52, pp. 33–43, 1964.
[11] D. Shyroki, "Exact equivalent straight waveguide model for bent and twisted waveguides," *IEEE Transactions on Microwave Theory and Techniques*, vol. 56, no. 2, pp. 414–419, 2008.
[12] *CST Microwave Studio 2006 Users Manual*. CST Ltd., Darmstadt, Germany.
[13] L. Maier and J. Slater, "Field strength measurements in resonant cavities," *Journal of Applied Physics*, vol. 23, no. 1, pp. 68–77, Jan. 1952.
[14] D. Goldberg and R. Rimmer, "Measurement and identification of HOMs in RF cavities," in *Proceedings of the 1997 Particle Accelerator Conference*, vol. 3, May 12–16, 1997, pp. 3001–3003.
[15] P. Matthews, T. Berenc, F. Schoenfeld, A. Feinerman, Y. Kang, and R. Kustom, "Electromagnetic field measurements on a millimeter wave linear accelerator," *IEEE Transactions on Microwave Theory and Techniques*, vol. 44, no. 8, pp. 1401–1409, Aug. 1996.
[16] D. McDiarmid and G. Walker, "Two examples of "confluence" in periodic slow wave structures," *IEEE Transactions on Microwave Theory and Techniques*, vol. 16, no. 1, pp. 2–6, Jan. 1968.
[17] P. Barrera, G. Gonzalez, L. Castellanos, and A. Prez. (2008, May) Unamalla mesh generation package. [Online]. Available: http://www.mathmoo.unam.mx/unamalla

Vita

Joshua Wilson was born in Milwaukee, WI on July 4, 1983. He attended Marquette University in Milwaukee and graduated from there with a B.S. in electrical engineering in 2004. He began his graduate studies at Marquette University and left in 2005 to pursue an internship at the Spallation Neutron Source at Oak Ridge National Laboratory.

In the fall of 2005, Joshua enrolled in the PhD program at the University of Tennessee, Knoxville. His research includes design of high power microwave devices for particle accelerator use, millimeter wave devices, numerical techniques in electromagnetics, and accelerator cavity design.